

desk 845-3261
845-5631

**ELECTROMAGNETIC PENETRATION THROUGH A SLOT IN A SCREEN
COVERED BY A DIELECTRIC SLAB**

BY

ROBERT DUDLEY NEVELS, JR.

**B.S.E.E., University of Kentucky, 1969
M.S.E.E., Georgia Institute of Technology, 1973**

**A Dissertation
Submitted to the Faculty of
The University of Mississippi
in Partial Fulfillment of the Requirements
for the Degree of Doctor of Philosophy
in Engineering Science**

**The University of Mississippi
November, 1979**

ELECTROMAGNETIC PENETRATION THROUGH A SLOT IN A SCREEN
COVERED BY A DIELECTRIC SLAB

BY

ROBERT DUDLEY NEVELS, JR.

Allie M. Smith
Dean of the School of
Engineering

Charles E. Smith
Professor and Chairman of
the Department of Electrical
Engineering

Joseph Tamm
Dean of the Graduate School

Chalmers W. Butler
Distinguished Professor of
Electrical Engineering
(Director of Dissertation)

Ronald R. Wilton
Professor of Electrical
Engineering

W. M. Causey
Professor of Mathematics

ABSTRACT

ELECTROMAGNETIC PENETRATION THROUGH A SLOT IN A SCREEN COVERED BY A DIELECTRIC SLAB

NEVELS, ROBERT D., JR. B.S., University of Kentucky, 1969.
M.S., Georgia Institute of Technology, 1973.
Ph.D., University of Mississippi, 1978. Dissertation
directed by Professor Chalmers M. Butler.

The problem of scattering from a slot in a screen covered by a dielectric slab has applications in the study of EMP (electromagnetic pulse) effects as well as the analysis of transmission and reception through apertures located on the surfaces of aircraft. Integral equations are derived in terms of the tangential electric field in the slot for an electromagnetic wave incident upon a single slot, coupled slots and a notch in a ground screen covered by a dielectric slab. The method of moments is used to solve the various coupled integral equations derived.

Results are presented for the electric field in a slot lying in a dielectric covered ground screen as a function of slot width and dielectric thickness. For the problem of multiple slots in a ground screen covered by a dielectric slab, results are given for the electric field in the slot as function of slot width, dielectric thickness and spacing between the slots. The electric field in the aperture of a notch in a ground screen covered by a dielectric slab is presented as a function of slot width, dielectric thickness and notch depth. The far electric and magnetic fields are presented for selected cases of the above problem.

The existence of a dielectric slab-air interface and the effect of surface waves in a dielectric slab causes a significant difference between the slot electric fields for a slot in a ground screen covered with a dielectric slab and a slot in a ground screen without a dielectric slab cover. The fact that surface waves are not attenuated in a lossless dielectric slab is confirmed by a study of the slot electric field for the case of coupled slots.

A method for handling singular Sommerfeld integrals which arise in problems involving a dielectric covered screen perforated by a slot is discussed. The Sommerfeld integrals used for the determination of the electric and magnetic far fields are solved by a saddle point integration procedure.

TABLE OF CONTENTS

	Page
LIST OF TABLES	vii
LIST OF FIGURES	viii
Chapter	
I. INTRODUCTION	1
1.1 Brief Literature Survey	1
1.2 Objectives of this Dissertation	6
II. A SLOT OF UNIFORM WIDTH IN AN INFINITE DIELECTRIC-COVERED CONDUCTING SCREEN	8
2.1 TE Excitation of a Slot in a Ground Screen Immersed in Dielectric Slab	10
2.1a Magnetic Field in the Region $z < 0$	12
2.1b Magnetic Field in the Region $z > 0$	15
2.1c Integral Equation for Tangential Electric Field in a Slot	17
2.2 TM Excitation of a Slotted-Screen by a Dielectric Slab	19
2.3 Discussion of the Integral Equations	22
2.4 Multiple Slots in a Dielectric Covered Infinite Planar Screen	24
III. SCATTERING OF SURFACE WAVES BY A NOTCH IN A PERFECTLY CONDUCTING INFINITE SCREEN COVERED BY A DIELECTRIC SLAB	28
3.1 General Formulation of the Integral Equations	30
3.2 Scattering Parameters	33

Chapter	Page
IV. NUMERICAL TECHNIQUE	37
4.1 Comparison of Original Sommerfeld Integral with the Sommerfeld Correction Term	38
4.2 Singularities Along the Path of Integration	46
4.2a Types of Singularities	46
4.2b Method of Handling Singular Integrals	52
4.3 Numerical Solution to the Integral Equation	57
V. RESULTS AND CONCLUSIONS	58
5.1 TE Excitation of a Slot in a Ground Screen Covered by a Dielectric Slab	58
5.1a TE Slot Magnetic Current Distribution	58
5.1b Convergence Tests	69
5.1c Plausibility Test	71
5.1d TE Case Far Fields	71
5.1e TE Case as a Function of Angle of Incidence	80
5.2 TM Excitation of a Slot in a Ground Screen Covered by a Dielectric Slab	80
5.2a TM Slot Magnetic Current Distribution	80
5.2b TM Case Far Fields	85
5.3 TE Excitation of Two Slots in a Ground Screen Covered by a Dielectric Slab	90
5.4 Excitation of a Notch in a Ground Screen Covered by a Dielectric Slab	103

	Page
APPENDIX A: GREEN'S FUNCTION SOLUTION FOR A LINE SOURCE IMBEDDED IN A DIELECTRIC SLAB	111
APPENDIX B: FAR FIELDS	128
APPENDIX C: SURFACE WAVE MODES	156
BIBLIOGRAPHY:	162
BIOGRAPHICAL SKETCH OF THE AUTHOR	165

LIST OF TABLES

LIST OF FIGURES

Figure		Page
2.1	General problem of a slot in an infinite conducting screen sandwiched between dielectric slabs and excited by infinite electric and magnetic line sources parallel to the axis of the slot.	9
2.2	Illustration of the use of the equivalence principle by replacing the slot with a perfect conductor bordered on either side by the appropriate magnetic currents for the case of TE illumination of the slot.	11
2.3	The equivalent problem of a slot in a screen covered by a dielectric slab, for the region $z < 0$ for the case of TE illumination of the slot.	13
2.4	The equivalent problem of a slot in a screen covered by a dielectric slab, for the region $z > 0$ for the case of TE illumination of the slot.	16
2.5	TE illumination of a perfectly conducting screen perforated by several slots of infinite extent and covered on both sides by dielectric slabs.	25
3.1	TM surface wave excitation of a 'notch' in a ground screen covered by a dielectric slab.	29
3.2	Equivalent problem of a 'notch' in a ground screen covered by a dielectric slab, valid for $z > 0$	29
4.1(a)	Integration contour along the real k_x -axis with $\pm k_a$ and $\pm k_b$ representing branch points and k_s representing a surface wave singularity.	44
4.1(b)	Integration contour deformed around the branch cut in the upper half plane.	44

Figure		Page
4.2	Typical kernel of the Sommerfeld correction term evaluated in the aperture for the case of TE incident illumination.	45
4.3	Far field kernel of Sommerfeld correction term for a TE slot as a function of angle where (—) real and (----) imag.	47
4.4	Branch cuts removed from the axis due to the introduction of loss in the k_a and k_b	50
5.1	Characteristic setup for parameter studies of this chapter with: ϵ_o dielectric constant of free space; $\epsilon_d = 2.7 \epsilon_o$; $\mu_d = \mu_o$ permeability of free space.	59
5.2a	Equivalent magnetic current $M_y(x) (=E_x^a)$ for a slot of width $0.1\lambda_o$, subject to normally incident TE excitation for various slab thicknesses.	60
5.2b	Equivalent magnetic current $M_y(x) (=E_x^a)$ for a slot of width $0.1\lambda_o$, subject to normally incident TE excitation for various slab thicknesses.	61
5.3a	Equivalent magnetic current $M_y(x) (=E_x^a)$ for a slot of width $0.5\lambda_o$, subject to normally incident TE excitation for various slab thicknesses.	63
5.3b	Equivalent magnetic current $M_y(x) (=E_x^a)$ for a slot of width $0.5\lambda_o$, subject to normally incident TE excitation for various slab thicknesses.	64
5.4	Equivalent magnetic current $M_y(x) (=E_x^a)$ for a slot of width $1.0\lambda_o$, subject to normally incident TE excitation for various slab thicknesses.	65

Figure	Page
5.5 Equivalent magnetic current $M_y(x) (=E_x^a)$ for a slot of width $3.0\lambda_o$, subject to normally incident TE excitation for various slab thicknesses.	66
5.6 Equivalent magnetic current $M_y(x) (=E_x^a)$ for a slot of width $1.0\lambda_o$, subject to normally incident TE excitation showing transition from the Free Space ($h=0$) case to the Two Media ($h=\infty$) case.	70
5.7 Plausibility test showing center-of-slot equivalent magnetic current $M_y(x) (=E_x^a)$ for a slot of width $3.0\lambda_o$, subject to normally incident TE excitation as a function of slot thicknesses $h = [a(\lambda_d/50), b(\lambda_d/10), c(\lambda_d/8), d(\lambda_d/4), e(5\lambda_d/16), f(3\lambda_d/8), g(\lambda_d/2), h(.6\lambda_d), i(.63\lambda_d), j(\lambda_{sl}+\lambda_d/50), k(\lambda_{sl}+\lambda_d/20)]$, where $\lambda_{sl} = .63\lambda_d$	72
5.8 Normalized space wave portion of the far magnetic field component $H_y(\theta)$ for a slot of width $0.1\lambda_o$, subject to normally incident TE excitation for various slab thicknesses.	74
5.9 Normalized space wave portion of the far magnetic field component $H_y(\theta)$ for a slot of width $0.5\lambda_o$, subject to normally incident TE excitation for various slab thicknesses.	76
5.10 Normalized space wave portion of the far magnetic field component $H_y(\theta)$ for a slot of width $1.0\lambda_o$, subject to normally incident TE excitation for various slab thicknesses.	77
5.11 Normalized space wave portion of the far magnetic field component $H_y(\theta)$ for a slot of width $3.0\lambda_o$, subject to normally incident TE excitation for various slab thicknesses.	78

Figure	Page
5.12 Normalized surface wave portion of the far magnetic field $H_y(\theta)$ for a slot of width $0.1\lambda_0$, subject to normally incident TE excitation for various slab thicknesses.	79
5.13a Equivalent magnetic current $M_y(x) (=E_x^a)$ for a slot of width $1.0\lambda_0$ and dielectric slab thickness $h = \lambda_d/8$, subject to TE excitation at a variety of angles of incidence.	81
5.13b Equivalent magnetic current $M_y(x) (=E_x^a)$ for a slot of width $1.0\lambda_0$ and dielectric slab thickness $h = \lambda_d/8$, subject to TE excitation at a variety of angles of incidence.	82
5.14 Normalized space wave portion of the far magnetic field $H_y(\theta)$ for a slot of width $1.0\lambda_0$ and dielectric slab thickness $h = \lambda_d/8$, subject to TE excitation at a variety of angles of incidence.	83
5.15 Equivalent magnetic current $M_x(y) (=E_y^a)$ for a slot of width $0.1\lambda_0$, subject to normally incident TM excitation for various slab thicknesses.	84
5.16 Equivalent magnetic current $M_x(y) (=E_y^a)$ for a slot of width $0.5\lambda_0$, subject to normally incident TM excitation for various slab thicknesses.	86
5.17 Equivalent magnetic current $M_x(y) (=E_y^a)$ for a slot of width $1.0\lambda_0$, subject to normally incident TM excitation for various slab thicknesses.	87
5.18 Equivalent magnetic current $M_x(y) (=E_y^a)$ for a slot of width $0.5\lambda_0$, subject to normally incident TM excitation for selected slab thicknesses.	88

Figure		Page
5.19	Normalized space wave portion of the far electric field component $E_y(\theta)$ for a slot of width $0.1\lambda_0$, subject to normally incident TM excitation at various slab thicknesses.	89
5.20	Normalized space wave portion of the far electric field component $E_y(\theta)$ for a slot of width $0.5\lambda_0$, subject to normally incident TM excitation at various slab thicknesses.	91
5.21	Normalized space wave portion of the far electric field component $E_y(\theta)$ for a slot of width $1.0\lambda_0$, subject to normally incident TM excitation at various slab thicknesses.	92
5.22	Normalized surface wave portion of the far electric field component $E_y(\theta)$ for a slot of width $0.1\lambda_0$, subject to normally incident TM excitation at various slab thicknesses.	93
5.23a	Equivalent magnetic current $M_y (=E_x^a)$ for two slots of width $0.1\lambda_0$ and $0.05\lambda_0$, subject to normally incident TE excitation for various slab thicknesses.	95
5.23b	Equivalent magnetic current $M_y (=E_x^a)$ for two slots of width $0.1\lambda_0$ and $0.05\lambda_0$, subject to normally incident TE excitation for various slab thicknesses.	96
5.24a	Equivalent magnetic current $M_y (=E_x^a)$ for two slots of width $0.1\lambda_0$, subject to normally incident TE excitation for various slab thicknesses, $s = 0.5\lambda_d$ center-of-slot separation distance.	97

Figure	Page
5.24b Equivalent magnetic current $M_y (=E_x^a)$ for two slots of width $0.1\lambda_0$, subject to normally incident TE excitation for various slab thicknesses, $s = 0.5\lambda_d$ center-of-slot separation distance.	98
5.25 Normalized far magnetic field $H_y(\theta)$ for two slots of width $0.1\lambda_0$ and separation distance $s = 0.5\lambda_d$ subject to TE excitation for various slab thicknesses.	99
5.26 Equivalent magnetic current $M_y (=E_x^a)$ for two slots of width $0.1\lambda_0$ and various slot separation distances s , subject to normally incident TE excitation with dielectric slab thickness $h = 0$	100
5.27 Equivalent magnetic current $M_y (=E_x^a)$ for two slots of width $0.1\lambda_0$ and various slot separation distances s , subject to normally incident TE excitation with dielectric slab thickness $h = \lambda_d/8$	101
5.28 Equivalent magnetic current $M_y (=E_x^a)$ for two slots of width $0.1\lambda_0$, subject to normally incident TE excitation when slot separation s is large and a slab of thickness $\lambda_d/8$ lies on the ground screen.	102
5.29 Equivalent magnetic current $M_y (=E_x^a)$ for a notch of width $0.02\lambda_0$ and depth $0.05\lambda_0$, subject to surface wave TM_x excitation for several slab thicknesses.	104
5.30 Equivalent magnetic current $M_y (=E_x^a)$ for a notch of width $0.02\lambda_0$ and depth $0.125\lambda_0$, subject to surface wave TM_x excitation for several slab thicknesses.	104

Figure	Page
5.31 Equivalent magnetic current $M_y (=E_x^a)$ for a notch of width $0.02\lambda_0$ and depth $0.25\lambda_0$, subject to surface wave TM_x excitation for several slab thicknesses.	105
5.32 Equivalent magnetic current $M_y (=E_x^a)$ for a notch of width $0.25\lambda_0$ and depth $0.05\lambda_0$, subject to surface wave TM_x excitation for several slab thicknesses.	105
5.33 Equivalent magnetic current $M_y (=E_x^a)$ for a notch of width $0.25\lambda_0$ and depth $0.125\lambda_0$, subject to surface wave TM_x excitation for several slab thicknesses.	106
5.34 Equivalent magnetic current $M_y (=E_x^a)$ for a notch of width $0.25\lambda_0$ and depth $0.25\lambda_0$, subject to surface wave TM_x excitation for several slab thicknesses.	106
5.35 Normalized far magnetic field for a notch of width $0.02\lambda_0$ and depth $0.05\lambda_0$, subject to surface wave TM_x excitation for several slab thicknesses.	107
5.36 Normalized far magnetic field for a notch of width $0.02\lambda_0$ and depth $0.125\lambda_0$, subject to surface wave TM_x excitation for several slab thicknesses.	107
5.37 Normalized far magnetic field for a notch of width $0.02\lambda_0$ and depth $0.25\lambda_0$, subject to surface wave TM_x excitation for several slab thicknesses.	108

Figure		Page
5.38	Normalized far magnetic field for a notch of width $0.25\lambda_o$ and depth $0.05\lambda_o$, subject to surface wave TM_x excitation for several slab thicknesses.	108
5.39	Normalized far magnetic field for a notch of width $0.25\lambda_o$ and depth $0.125\lambda_o$, subject to surface wave TM_x excitation for several slab thicknesses.	109
5.40	Normalized far magnetic field for a notch of width $0.25\lambda_o$ and depth $0.25\lambda_o$, subject to surface wave TM_x excitation for several slab thicknesses.	109
A.1	Infinite magnetic line source embedded in a dielectric slab and polarized in the y-direction.	112
A.2	Infinite magnetic line source embedded in a dielectric slab and polarized in the x-direction.	112
A.3	Top and bottom sheets of the Riemann surface for the β^2 -plane.	123
A.4	Top and bottom sheets of the Riemann surface for the k_x^2 -plane.	123
A.5a	Region of validity for $k_x^2 - k_{x_i}^2 \leq \gamma'$ in the k_x -plane.	126
A.5b	Curves in the k_x -plane satisfying $2k_{x_r} - k_{x_i} = -\gamma''$	126
A.6	Top and bottom sheets of the Riemann surface for the k_x -plane.	126
B.1	Top and bottom sheets of the complex k_x -plane for the case of a dielectric slab with no loss.	136

Figure	Page
B.2 Complex α -plane segmented to indicate quadrants mapped from the top (T) and bottom (B) of the k_x -plane.	136
B.3 The complex γ -plane segmented into quadrants mapped from the top (T) and bottom (B) of the k_x -plane.	140
B.4 Contours in the complex τ -plane before (C) and after (S) deformation through the steepest descents path.	140
B.5 Successive steepest descent contours S demonstrating how surface and leaky wave poles are captured in the α -plane. . . .	147
B.6 Successive steepest descent contours S demonstrating how surface and leaky wave poles are captured in the γ -plane. . . .	151
C.1 A dielectric slab of thickness h located above a perfectly conducting ground plane. . .	157
C.2 Graphical solution for surface wave modes. . .	157

CHAPTER I
INTRODUCTION

1.1 Brief Literature Survey

The objective of this research project is to study the consequences of placing a dielectric slab over a perfectly conducting ground plane perforated by a slot-aperture. The problem as presented here involves an incident field illuminating an infinite length slot in a ground screen with a dielectric slab placed over the illuminated or the shadow side of the ground screen, or of a slot-perforated ground screen immersed in a slab of finite thickness. For each of these cases it can be established [24] that surface waves propagate in a dielectric slab lying on a ground plane as long as the relative dielectric constant of the slab is other than that of the surrounding medium. When the TM mode of surface wave occurs, no lower frequency cut-off exists, regardless of slab thickness.

For antennas, the excitation of surface waves represents a loss in terms of useful radiated power in a given direction and therefore results in a reduction of the antenna gain [6]. The presence of surface waves can cause spurious radiation at finite terminations of the dielectric slab or discontinuities in the conductor surface. For these and several related problems extensive measurements of radiated field, conductance and susceptance have been carried out [2,5,6,8,10,11]. However, since to our knowledge no previous work has been done on the effect of discontinuities in the conductor surface on radiation by surface waves, we examine, also, the problem of radiation caused by a rectangular "notch" of various

dimensions in the surface of the ground plane covered by a dielectric slab.

Much of the early literature deals with the impedance properties of a rectangular waveguide with a dielectric-covered broad face perforated by narrow radiating slots. Several investigators [4,5] have published calculations of conductance and susceptance versus dielectric-cover thickness, dielectric constant, and slot displacement from the center line of the broadside of the waveguide. It was found [5] that sharp resonant peaks in the reflection coefficient of such structures are associated with thick dielectric slabs, and that such resonances may be avoided by using thin slabs. For the design of dielectric-covered resonant slots in a rectangular waveguide, Bailey [1] presents a modified Stevenson's theory [13] for normalized conductance of a slot as a function of dielectric thickness in order to find an upper bound on conductance variation for thick dielectric material.

If the slot under consideration is located in a conducting plane of infinite extent, Fourier transform theory can be used to express the electric field in the slot in terms of a Fourier transform of an assumed spectral distribution. Theoretical curves which show the change in impedance in terms of the dielectric constant and dielectric thickness compare favorably with experiment and therefore justify this approach for thin slabs [1]. Clark, Rudduck, and Wu have improved upon these results by using a surface integration technique [9].

Pattern measurements of slot radiators in dielectric-coated metal plates were first obtained by Bailey [8]. These measurements were the

result of an investigation into the role that the dimensions of width and length as well as thickness of dielectric play on measured slot antenna patterns for dielectric coated ground planes. It was found that for small thicknesses the shape of the radiation pattern is essentially unchanged from the uncoated plane regardless of the length and the width of the dielectric cover. When thicknesses are increased, this dimension and the direction of propagation of the surface wave is a primary factor in the shape of the measured pattern.

The case of a waveguide terminated in a slot in a ground plane of infinite extent with a dielectric slab covering [3] has also been studied. A disagreement of about twenty percent was noted in comparisons of normalized conductance or susceptance versus frequency with calculations made from a mathematical analysis of the problem using the Fourier methods mentioned above for some thin sheet cases. It was concluded that tolerances do not explain the error. A measurement of slot field for cases where maximum error occurs revealed significant distortions. It was concluded that higher order modes which are neglected in the analysis are the probable cause of disagreement. The integral equation method, which takes into account higher order modes that exist in the slot is used in this paper.

Wu [6] considered the problem of a parallel plate waveguide opening into a ground plane covered by a dielectric slab. He determined that, due to the presence of the dielectric slab, slot electric fields contain a high content of higher order modes and that the use of only the

dominant mode for the spectral function or variational approach can lead to considerable error. His integral equation approach, however, allows the determination of more accurate radiation patterns and the amount of energy supplied to excite surface waves. A knowledge of the power carried by the surface waves is important if the slot is to be used as a directive antenna.

An investigation has also been made of the input admittance of a circular waveguide opening into a dielectric-coated ground plane [2]. Good agreement between theory and measurements was claimed when the TE_{11} dominant mode was used for the aperture field. It was also reported that the amount of energy trapped inside the dielectric for the case of a circular waveguide was about twenty-five percent less than for the case of a rectangular waveguide over most of the frequency band, providing a significant advantage over the rectangular guide in terms of far field radiated power outside the dielectric slab.

Some interesting work has been carried out concerning the effects of a dielectric slab covering over phased arrays [25]. The freely excited array was least sensitive to the effects of the dielectric coating. The performance of the standing-wave array was degraded by multiple reflections in the branch lines, while the performance of the traveling-wave array was degraded by changes in the propagation characteristics of the main line [17]. The effect of a dielectric-sheet-cover on a circular array of axial thin slits has also been considered [14]. It was shown that in circular arrays, pattern distortions similar to those occurring in planar arrays were observed.

A study of the literature to this point indicates that pattern distortion and impedance peculiarities prevalent for the different structures mentioned are certainly due to the effects of the dielectric. A closer look, however, indicates that previous investigators were not just viewing a problem of internal reflections, since reflections can be compensated by the use of matching elements. The underlying implication of the work being done in this area is that energy is coupled into surface wave modes and radiated or reflected causing changes in the various parameters of the system. In several of the papers studied it was noted that in explanations of pattern distortions there seems to be some confusion as to the mechanism of surface wave involvement. We believe that this is due in part to the lack of a thorough analytical solution to the problems mentioned. It is our intention to give a more accurate and complete analytical solution than has thus far been attained. This solution, of necessity, involves a careful study of the surface waves.

The mathematical method utilized in this paper is that of finding an integral equation which when solved by use of the method of moments yields the tangential electric field in the plane of the slot. Electromagnetic diffraction by an aperture in an infinite conducting screen situated in a homogeneous medium has been investigated by several researchers in recent years. An integral equation solution to the two-media problem in which the half-spaces separated by the conducting screen contain different electromagnetic properties was first presented for a case other than that of an electrically small aperture by Butler and

Umashankar [48]. More recently the problem of diffraction by an aperture in a planar, conducting screen separating partitioned half spaces was investigated [49]. The mathematical techniques used in this paper are similar to and are seen to be a natural extension of those used in the two above mentioned papers (i.e. [48] and [49]).

Radiation through a slot in a ground screen covered by a dielectric slab also has several implications in the area of EMP studies. Shielding of minute cracks in the surface of aircraft is a primary concern. It is hoped that through this study some recommendations can be made concerning protection of aircraft from such a large voltage surge. In the event that some "leakage" into the craft does occur, the problem of damage to equipment at points far removed from the entry location, due to the coupling of energy into surface-wave modes, is also evident and is carefully examined.

1.2 Objectives of this Dissertation

The principal objectives of this dissertation are as follows:

1. To formulate the integro-differential equations for the magnetic current in a slot for the following series of problems:
 - (a) Penetration through an infinite-length slot in a ground screen covered by a dielectric slab on the illuminated and shadow side.

- (b) Penetration through coupled infinite-length slots in a ground screen covered by a dielectric slab on the illuminated or shadow sides or immersed in a slab of finite thickness.
 - (c) Scattering of a surface wave propagating along a dielectric-slab covered conductor by a notch of infinite length.
2. To determine the magnetic current distribution in the slot for each of the above problems by solving the formulated equations by the method of moments. Numerical results are obtained subject to variations in the parameters of slot width and slab thickness for each case.
 3. To formulate expressions for far field radiation and to compute the radiated field patterns for several of the cases mentioned above.

CHAPTER II

A SLOT OF UNIFORM WIDTH IN AN INFINITE DIELECTRIC-COVERED CONDUCTING SCREEN

The general type of problem considered in this chapter is that of TE (TM) illumination of a slot of infinite length and finite width which has been excited from both the $z < 0$ and the $z > 0$ regions. Fig. 2.1 illustrates a cross-sectional view of the slot which is contained in a thin conducting screen that covers the $z = 0$ plane and is immersed in a dielectric slab lying in the region $-t_1 \leq z \leq t_2$. It is assumed that the dielectric constant is different and that the dielectric loss is small in each of the four regions shown in Fig. 2.1.

The first few sections of this chapter are devoted to the case of TE slot illumination for which we develop fully the integral equations for problems with the tangential electric field in the slot as the unknown. The next section deals with another basic problem, that of TM illumination of the infinite slot in a ground screen which is immersed in a dielectric slab. In the last section an investigation of the problem of coupled slots in a dielectric-covered screen is presented. In all the problems considered here, TE (TM) illumination of the slot describes a situation where the incident electric (magnetic) field vector lies in a direction transverse to the axis of the slot.

The derivation of the Green's function for a line source embedded in a dielectric slab is essential to the mathematical construction of the various equations of this dissertation. A technique for deriving

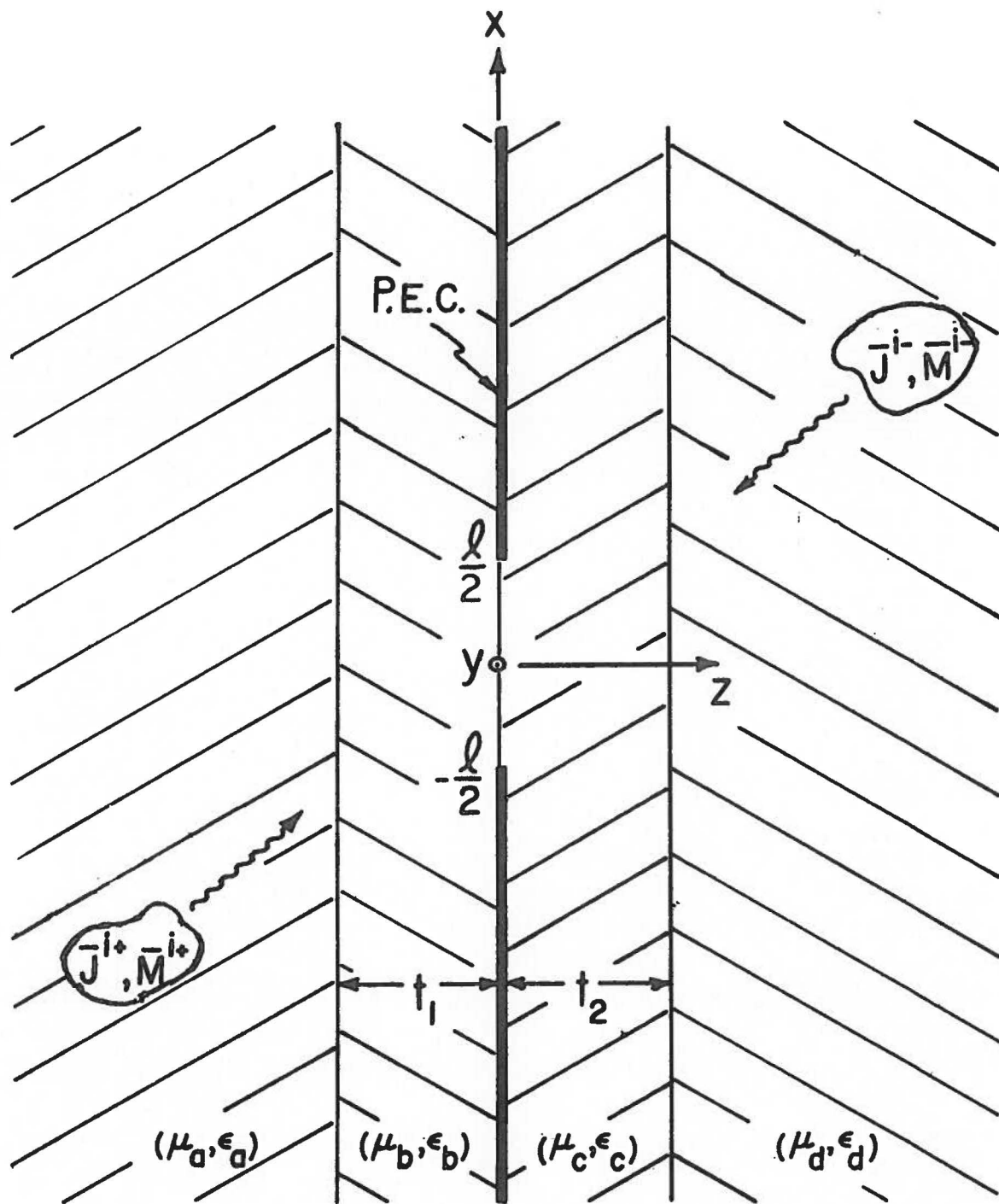


Fig. 2.1 General problem of a slot in an infinite conducting screen sandwiched between dielectric slabs and excited by infinite electric and magnetic line sources parallel to the axis of the slot.

this Green's function is presented in Appendix A [37]. The basic concept of this procedure involves finding a solution for the electric vector potential due to an infinite magnetic line source, subject to continuity conditions at the dielectric slab-air interface and the radiation condition. The electric vector potential for a dielectric-covered slot is then found by convolving the slot magnetic current distribution with the proper Green's function over the slot limits. Expressions for the magnetic field in each of the dielectric regions may be written in terms of the electric vector potential in each of the respective dielectric regions. The desired integral equations are then obtained by enforcing continuity of tangential magnetic field through the slot.

2.1 TE Excitation of a Slot in a Ground Screen Immersed in a Dielectric Slab

The general case of TE excitation of an infinite slot in a screen having a dielectric-slab cover in the $-t_1 \leq z \leq t_2$ region (see Fig. 2.2a) is dealt with below. The screen, which lies in the $z = 0$ plane, is assumed to be vanishingly thin, perfectly conducting and infinite in extent. The source varies harmonically in time according to the factor $e^{j\omega t}$. This factor is suppressed in the following analyses.

The transverse component of electric field, E_x^a , which is the unknown to be determined, is that component of electric field in the slot which is polarized in a direction parallel to the screen and perpendicular to the axis of the slot. The incident magnetic field is polarized parallel to the axis of the slot ($\bar{H}^{inc} = H^{inc}\hat{y}$). The situation shown in Fig. 2.2b is equivalent to the problem illustrated in Fig. 2.2a and has

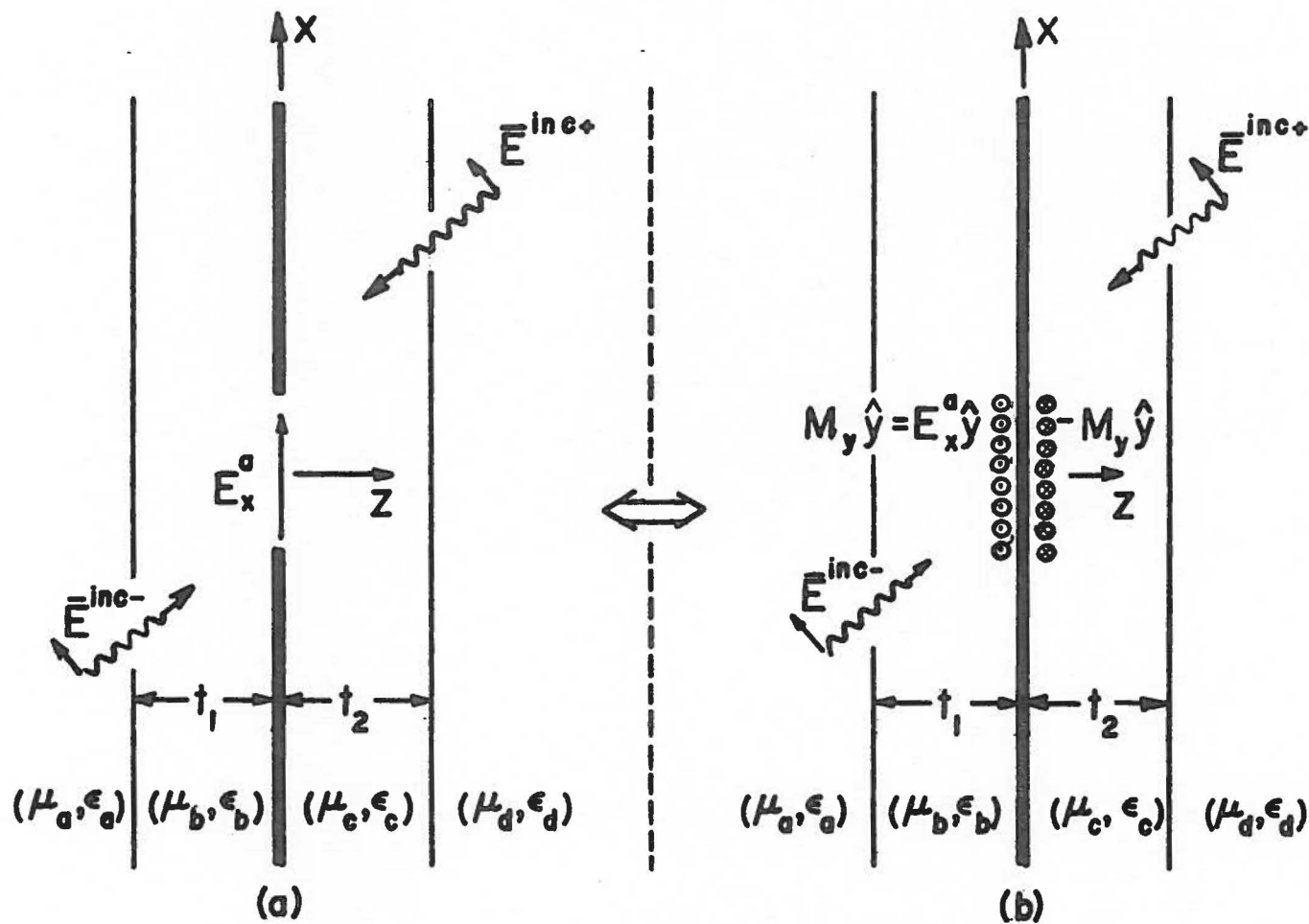


Fig. 2.2 Illustration of the use of the equivalence principle by replacing the slot with a perfect conductor bordered on either side by the appropriate magnetic currents for the case of TE illumination of the slot.

been obtained by resorting to the equivalence principle. This means that, if the slot is shorted by a perfect electric conductor (P.E.C.), the fields in the two half spaces will remain the same if the appropriate magnetic currents are placed over the shorted slot on either side of the screen.

2.1a Magnetic Field in the Region $z < 0$

The equivalent problem valid in the region $z < 0$, shown in Fig. 2.3c, is obtained by imaging the magnetic current pictured in Fig. 2.3b in the infinite plane screen. In Fig. 2.3c the magnetic currents are seen to be radiating in a dielectric slab of thickness $2t_1$ and therefore the fields, valid in the space $z < 0$, can be found from the expressions for electric vector potential \bar{F}^a_b . Since the slot magnetic current is directed entirely parallel to the slot axis, then the electric vector potential can be expressed as $\bar{F}^a_b = F_y^b \hat{y}$. One can write the total magnetic field in the left half-space at a point \bar{r} as

$$\bar{H}_y^b(\bar{r}) = H_y^{sc}(\bar{r}) \hat{y} - \frac{j\omega}{k_a^2} (k_a^2 + \nabla \cdot) F_y^b(\bar{r}) \hat{y} \quad (2.1)$$

where k_a is the propagation constant in mediums (a) and (b) respectively. $H_y^{sc}(\bar{r})$ is called the short circuit magnetic field and is that field which would exist in regions a and b, due to the source current \bar{J}^i , \bar{M}^i when the slot is short circuited. Since performance of the divergence operation in Eq. (2.1) above would require one to take a derivative of the vector potential with respect to the y-direction, a coordinate with which $F_y^b(\bar{r})$ does not vary, Eq. (2.1) reduces to

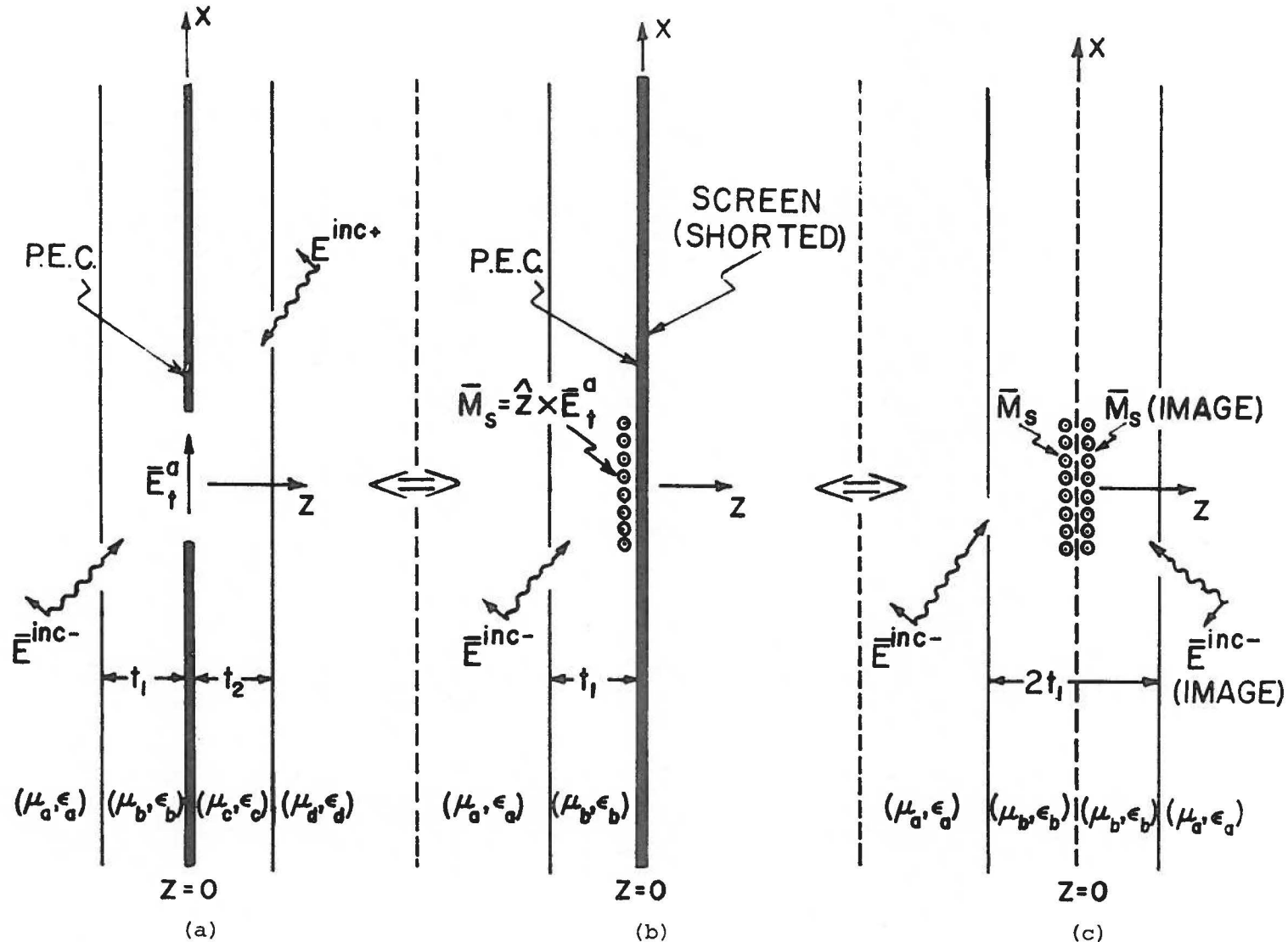


Fig. 2.3 The equivalent problem of a slot in a screen covered by a dielectric slab, for the region $z < 0$, for the case of TE illumination of the slot.

$$H_y^b(\vec{r}) = H_y^{sc}(\vec{r}) - j\omega F_y^b(\vec{r}), \quad z < 0 \quad (2.2)$$

Utilizing the Green's function G_b derived in Appendix A for the case of polarization in the direction of the slot axis, one may write an expression for the electric vector potential in region (b)

$$F_y^b(\vec{r}) = \int_{x'=-l/2}^{l/2} 2M_y(x') G_b(x, x', z) dx' \quad (2.3)$$

where

$$G_b(x, x', z) = \frac{-j\epsilon_b}{4} \left[H_0^{(2)}(k_b \sqrt{z^2 + (x-x')^2}) - \frac{4}{\pi} \int_{k_x=0}^{\infty} \left(\frac{\Gamma_k^- e^{-j2\beta_b t_1}}{\Gamma_k^- e^{-j2\beta_b t_1} + 1} \right) \frac{\cos \beta_b z \cos k_x (x-x') dk_x}{\beta_b} \right] \quad (2.4)$$

with

$$\Gamma_k^- = \frac{\epsilon_b \beta_a - \epsilon_a \beta_b}{\epsilon_b \beta_a + \epsilon_a \beta_b} \quad (2.5)$$

and

$$\beta_b^a = \begin{cases} \sqrt{k_a^2 - k_x^2}, & k_a \geq k_x \\ -j\sqrt{k_x^2 - k_a^2}, & k_a \leq k_x \end{cases} \quad (2.6)$$

Here ϵ_a and μ_a are the dielectric constant and permeability, respectively, of mediums a and b. $H_0^{(2)}$ is the Hankel function of the second kind and zero order. Magnetic current $M_y(x)$, in the slot is expressed in terms of electric field in the slot

$$M_y(x) = E_x^a(x)$$

2.1b Magnetic Field in the Region $z > 0$

The field in the region $z > 0$ can be obtained by imaging (see Fig. 2.4) as was done in the previous section. The magnetic field in this region is

$$\overline{H}_y^d(\vec{r}) = H_y^{sc}(\vec{r})\hat{y} + \frac{j\omega}{k_c^2} (k_c^2 + \nabla \cdot) F_y^d(\vec{r})\hat{y}$$

which reduces to

$$\overline{H}_y^d(\vec{r}) = H_y^{sc}(\vec{r}) + j\omega F_y^d(\vec{r}), \quad z > 0 \quad (2.7)$$

where $H_y^{sc}(\vec{r})$ is the short-circuit magnetic field in regions c and d.

A positive sign in front of the vector potential on the right hand side of the equation above is accounted for by the fact that the vector potential is defined with the same form in both half spaces ($z > 0$ and $z < 0$) even though the equivalent magnetic current is in opposite directions in the two regions. The sign of the current is removed from the definition of vector potential in the equations for $\overline{H}_y^d(\vec{r})$. Utilizing the Green's function derived in Appendix A, one can immediately write down an expression for the vector potential in region (c) as

$$F_y^c(\vec{r}) = \int_{x'=-\ell/2}^{\ell/2} 2M_y(x') G_c(x, x', z) dx' \quad (2.8)$$

where

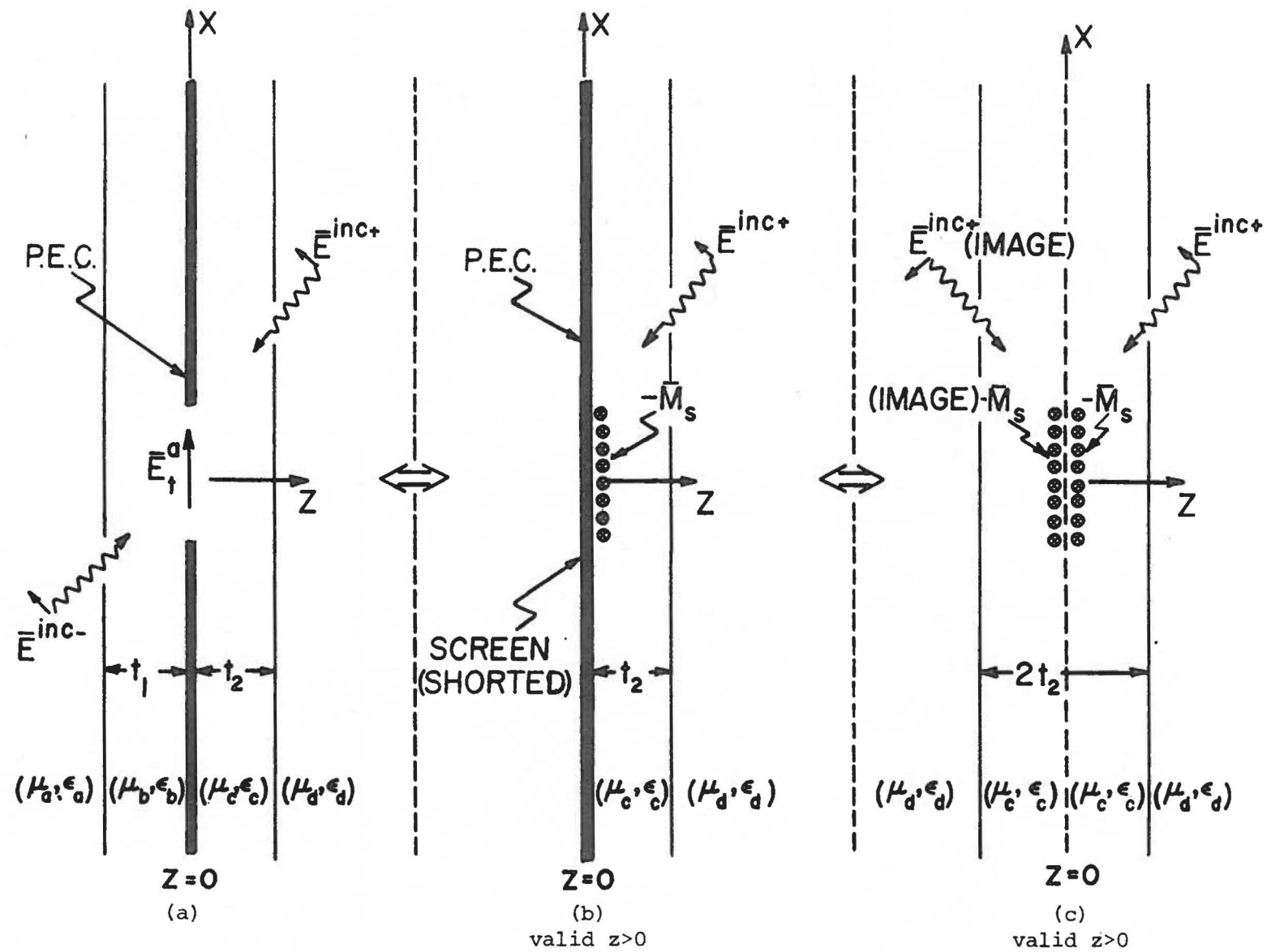


Fig. 2.4 The equivalent problem of a slot in a screen covered by a dielectric slab, for the region $z > 0$, and for the case of TE illumination of the slot.

$$G_c(x, x', z) = \frac{-j\epsilon_c}{4} \left[H_0^{(2)} \left(k_c \sqrt{z^2 + (x-x')^2} \right) - \frac{4}{\pi} \int_{k_x=0}^{\infty} \left(\frac{\Gamma_k^+ e^{-j2\beta_c t_2}}{\Gamma_k^+ e^{-j2\beta_c t_2} + 1} \right) \frac{\cos\beta_c z \cos k_x (x-x') dk_x}{\beta_c} \right] \quad (2.9)$$

with

$$\Gamma_k^+ = \frac{\epsilon_c \beta_d - \epsilon_d \beta_c}{\epsilon_c \beta_d + \epsilon_d \beta_c} \quad (2.10)$$

and

$$\frac{\beta_c}{d} = \begin{cases} \sqrt{\frac{k_c^2}{d} - k_x^2}, & k_x \leq \frac{k_c}{d} \\ -j \sqrt{\frac{k_x^2}{d} - k_c^2}, & k_x \geq \frac{k_c}{d} \end{cases} \quad (2.11)$$

2.1c Integral Equation for Tangential Electric Field in Slot

$\bar{H}^c(\bar{r})$ and $\bar{H}^b(\bar{r})$ satisfy Maxwell's equation and the radiation condition as well as the appropriate boundary conditions on the screen. An integral equation involving the slot magnetic current (or E_x^a) as the unknown can now be found by enforcing continuity of tangential magnetic field in the slot. Taking the limit as z approaches zero, one can equate the tangential magnetic fields in the two dielectric slab regions in the following manner:

$$\lim_{z \uparrow 0} (\bar{H}^b(x) \times \hat{z}) = \lim_{z \downarrow 0} (\bar{H}^c(x) \times \hat{z})$$

$$\lim_{z \uparrow 0} (H_y^{sc^b}(x) - j\omega F_y^b(x)) \hat{y} \times \hat{z} = \lim_{z \downarrow 0} (H_y^{sc^c}(x) + j\omega F_y^c(x)) \hat{y} \times \hat{z}$$

or

$$F_y^b(x) + F_y^c(x) = -\frac{j}{\omega} (H_y^{sc^b}(x) - H_y^{sc^c}(x)) \quad (2.12)$$

Accomodating the fact that in the slot $z=0$, one combines Eqs. (2.3) and (2.8) with Eq. (2.12) to get

$$\begin{aligned} & \epsilon_b \int_{x'=-\ell/2}^{\ell/2} M_y(x') \left[H_0^{(2)}(k_b |x-x'|) \right. \\ & \quad \left. - \frac{4}{\pi} \int_{k_x=0}^{\infty} \left(\frac{\Gamma_k^- e^{-j2\beta_b t_1}}{\Gamma_k^- e^{-j2\beta_b t_1} + 1} \right) \frac{\cos k_x (x-x')}{\beta_b} dk_x \right] dx' \\ & + \epsilon_c \int_{x'=-\ell/2}^{\ell/2} M_y(x') \left[H_0^{(2)}(k_c |x-x'|) \right. \\ & \quad \left. - \frac{4}{\pi} \int_{k_x=0}^{\infty} \left(\frac{\Gamma_k^+ e^{-j2\beta_c t_2}}{\Gamma_k^+ e^{-j2\beta_c t_2} + 1} \right) \frac{\cos k_x (x-x')}{\beta_c} dk_x \right] dx' \\ & = \frac{2}{\omega} (H_y^{sc^b} - H_y^{sc^c}) \end{aligned} \quad (2.13)$$

The short-circuit magnetic field in the interval $-\ell/2$ to $\ell/2$ for an arbitrary angle of incidence due to plane wave excitation is found to be

$$H_y^{sc^b}(x) = \frac{2T^+ E_0}{n_b} e^{-jk_a x} \sin \theta_i^+ \quad (2.14)$$

where $H_y^{sc^b}$ is evaluated on the shorted perfectly conducting screen

and the transmission coefficient T is

$$T^+ = \frac{\eta_b \cos \theta_i^+ e^{jk_a t_1} \cos \theta_t^+}{\eta_a \cos \theta_i^+ \cos(k_b t_1 \cos \theta_t^+) + j \eta_b \cos \theta_t^+ \sin(k_b t_1 \cos \theta_t^+)} \quad (2.15)$$

The angle of incidence on the dielectric slab is θ_i^+ and the angle of transmission through the slab is determined from Snell's law to be

$$\theta_t^+ = \sin^{-1} \left(\sqrt{\frac{\epsilon_a}{\epsilon_b}} \frac{d}{c} \sin \theta_i^+ \right) \quad (2.16)$$

where θ^- and θ^+ represent angles in region $z < 0$ and $z > 0$ respectively. Also

$$\eta_s = \sqrt{\frac{\mu_s}{\epsilon_s}} ; \quad s = a, b, c, d \quad (2.17)$$

In general the amplitude of the incident plane wave is chosen so that

$$E_0 = 1.$$

2.2 TM Excitation of a Slotted-Screen Covered by a Dielectric Slab

The general equations for TM illumination of an infinite length slot in a screen immersed in a dielectric slab are derived in this section by a procedure analogous to that presented in Section 2.1. An application of the above mentioned procedure outlined in Section 2.1 first requires finding an expression for the x-component of the total magnetic field in the left half-space parallel to the plane of the slot

$$H_x^a(\vec{r}) = H_x^{sc}(\vec{r}) - \frac{j\omega}{k_a^2} \left(k_a^2 + \frac{\partial^2}{\partial x^2} \right) F_x^b, \quad z < 0 \quad (2.18)$$

then the x-component of the total magnetic field in the right half-space parallel to the plane of the slot

$$\overset{c}{H}_x^d(\vec{r}) = \overset{sc}{H}_x^d(\vec{r}) + \frac{j\omega}{k_c^2} (k_b^2 + \frac{\partial^2}{\partial x^2}) F_x^d, \quad z > 0 \quad (2.19)$$

where

$$\vec{r} = x\hat{x} + z\hat{z}$$

Requiring continuity of magnetic field in the slot, one obtains

$$\lim_{z \uparrow 0} (\overset{b}{H}_x \hat{x} \times \hat{z}) = \lim_{z \downarrow 0} (\overset{c}{H}_x \hat{x} \times \hat{z})$$

or

$$\begin{aligned} \lim_{z \uparrow 0} \left[\overset{sc}{H}_x^b(x) - \frac{j\omega}{k_b^2} (k_b^2 + \frac{\partial^2}{\partial x^2}) F_x^b(x) \right] \hat{x} \times \hat{z} \\ = \lim_{z \downarrow 0} \left[\overset{sc}{H}_x^c(x) + \frac{j\omega}{k_c^2} (k_c^2 + \frac{\partial^2}{\partial x^2}) F_x^c(x) \right] \hat{x} \times \hat{z} \end{aligned} \quad (2.20)$$

Rearranging terms in Eq. (2.20), one obtains the integro-differential equation in the slot

$$\frac{1}{k_b^2} (k_b^2 + \frac{\partial^2}{\partial x^2}) F_x^b(x) + \frac{1}{k_c^2} (k_c^2 + \frac{\partial^2}{\partial x^2}) F_x^c(x) = -\frac{j}{\omega} (\overset{sc}{H}_x^b(x) - \overset{sc}{H}_x^c(x)) \quad (2.21)$$

Utilizing the Green's function derived in Appendix A for the case of polarization parallel to the dielectric slab interface and along the slot axis, one may write the complete integral equation for the case of TM illumination of a slotted screen immersed in a dielectric slab as follows

$$\begin{aligned}
& \frac{\epsilon_b}{k_b^2} (k_b^2 + \frac{\partial^2}{\partial x^2}) \int_{x'=-\ell/2}^{\ell/2} M_x(x') \left[H_0^{(2)}(k_b |x-x'|) \right. \\
& \quad \left. - \frac{4}{\pi} \int_{k_x=0}^{\infty} \left(\frac{\Gamma_g^- e^{-j2\beta_b t_1}}{\Gamma_g^- e^{-j2\beta_b t_1} + 1} \right) \frac{\cos k_x (x-x')}{\beta_b} dk_x \right] dx' \\
& + \frac{\epsilon_c}{k_c^2} (k_c^2 + \frac{\partial^2}{\partial x^2}) \int_{x'=-\ell/2}^{\ell/2} M_x(x') \left[H_0^{(2)}(k_c |x-x'|) \right. \\
& \quad \left. - \frac{4}{\pi} \int_{k_x=0}^{\infty} \left(\frac{\Gamma_g^+ e^{-j2\beta_c t_2}}{\Gamma_g^+ e^{-j2\beta_c t_2} + 1} \right) \frac{\cos k_x (x-x')}{\beta_c} dk_x \right] dx' \\
& = \frac{2}{\omega} (H_x^{sc^b}(x) - H_x^{sc^c}(x)) \quad (2.22)
\end{aligned}$$

with

$$\frac{\Gamma_g^+}{\Gamma_g^-} = \frac{\beta_b \mu_a - \beta_a \mu_b}{\beta_b \mu_a + \beta_a \mu_b} \quad (2.23)$$

β is as defined in Eqs. (2.6) and (2.11) and μ_a is the permeability in regions a and d, respectively. The short circuit magnetic field on the shorted screen for the case of TM plane wave illumination is

$$H_x^{sc^b}(x) = - \frac{E_0 T^+}{n_b c} \cos \theta_t e^{-jk_b \frac{x}{c} \sin \theta_t} \quad (2.24)$$

where the transmission coefficient T is

$$T^+ = \frac{\eta_b \cos \theta_i^+ e^{jk_a t_1} \frac{t_1}{2} \cos \theta_i^+}{j \sin(k_b t_1 \sin \theta_t^+) (\eta_b \cos \theta_i^+ + \eta_a \cos \theta_t^+)} \quad (2.25)$$

The angles of incidence from each half space θ_i^+ and the angles of transmission through the dielectric slab interface θ_t^+ are related by Eq. (2.16). The impedance of the various mediums is defined by Eq. (2.17).

2.3 Discussion of the Integral Equations

The integrand of each integral in Eqs. (2.13) and (2.22) is a combination of two terms which are the Green's functions for two polarizations of a magnetic line source embedded in a dielectric slab. The first term of these Green's functions, a Hankel function of the second kind and zero order, can be viewed as the Green's function for a line source radiating into an infinite homogeneous space with the electrical character of the dielectric slab. The second term, which is of a class of functions known as Sommerfeld integrals [38], can be viewed as a correction term accounting for the finite width of the dielectric slab. The correction term integral is over the continuous wave number spectrum and is attributed to the interaction of the wave functions from the line source in the dielectric slab with the surrounding media.

Although the correction terms for the TE and TM incidence cases appear to be very similar, an important distinction is noted when one observes that the singularities of the integrand of the correction terms have a special significance. To understand this significance we first note that a TE (TM) wave incident upon a slot results in the excitation of TM (TE) surface waves in a dielectric slab covering the slot. However, these surface waves, which are bound within the slab region, occur at discrete values of the transverse wave number. When the k_x integration variable of the correction term encounters these values, the integrand indicates the onset of a surface wave by displaying a characteristic singularity. These surface wave singularities occur at different points in the k_x spectrum, depending on whether a TE or a TM surface is excited.

The number of surface waves that occur depend upon the dielectric constant, the frequency, and the thickness of the dielectric slab. If, for example, the dielectric constants in all four regions approach the same value, then one has the classic aperture penetration problem. On the other hand, allowing the dielectric constants in the two regions for $z < 0$ to approach the same value ϵ_- while the dielectric constants in the two media for $z > 0$ approach a different value ϵ_+ , produces the two media problem [44]. In both these cases the Sommerfeld correction term goes to zero and no surface wave exists. Similar circumstances occur when the dielectric slab thickness is reduced to zero or is increased to infinity. When the imaginary part of the dielectric constant in either region (a) or (d) is allowed to approach $-\infty$, then the problem of penetration into (radiation from) a parallel-plate guide can be produced. Integral

equations for the coupling between two parallel plate guides are arrived at by requiring that the imaginary part of the dielectric constant in both regions (a) and (d) approach $-\infty$. Numerous combinations of the above mentioned cases can be constructed from the general problems of Sections 2.1 and 2.2.

2.4 Multiple Slots in a Dielectric Covered Infinite Planar Screen

Although several interesting slot penetration problems arise from particularization of the cases presented in Sections 2.1 and 2.2, the case of d' excitation by a dielectric-slab-covered perfectly-conducting screen perforated by several slots has certain unique characteristics which are worth consideration (see Fig. 2.5). From a mathematical viewpoint this problem leads to a number of coupled integral equations equal to the number of slots perforating the conducting screen. It is also shown that significant coupling between the slots occurs even for slot-separation distances of many wavelengths.

We contend that coupling between the various slots is expected from a physical standpoint since surface waves are launched from each slot and travel unattenuated in the lossless medium of the dielectric slab. It is this surface wave phenomena that gives rise to drastic changes in the slot fields at distances beyond which one would expect ordinary coupling between slots to have become virtually nil.

For TE excitation, integral equations for the multiple slot case are derived in the same way that integral equations for the single slot case of Section 2.1 are derived. By appealing to the equivalence principle one can find expressions for the magnetic fields in the dielectric slabs on

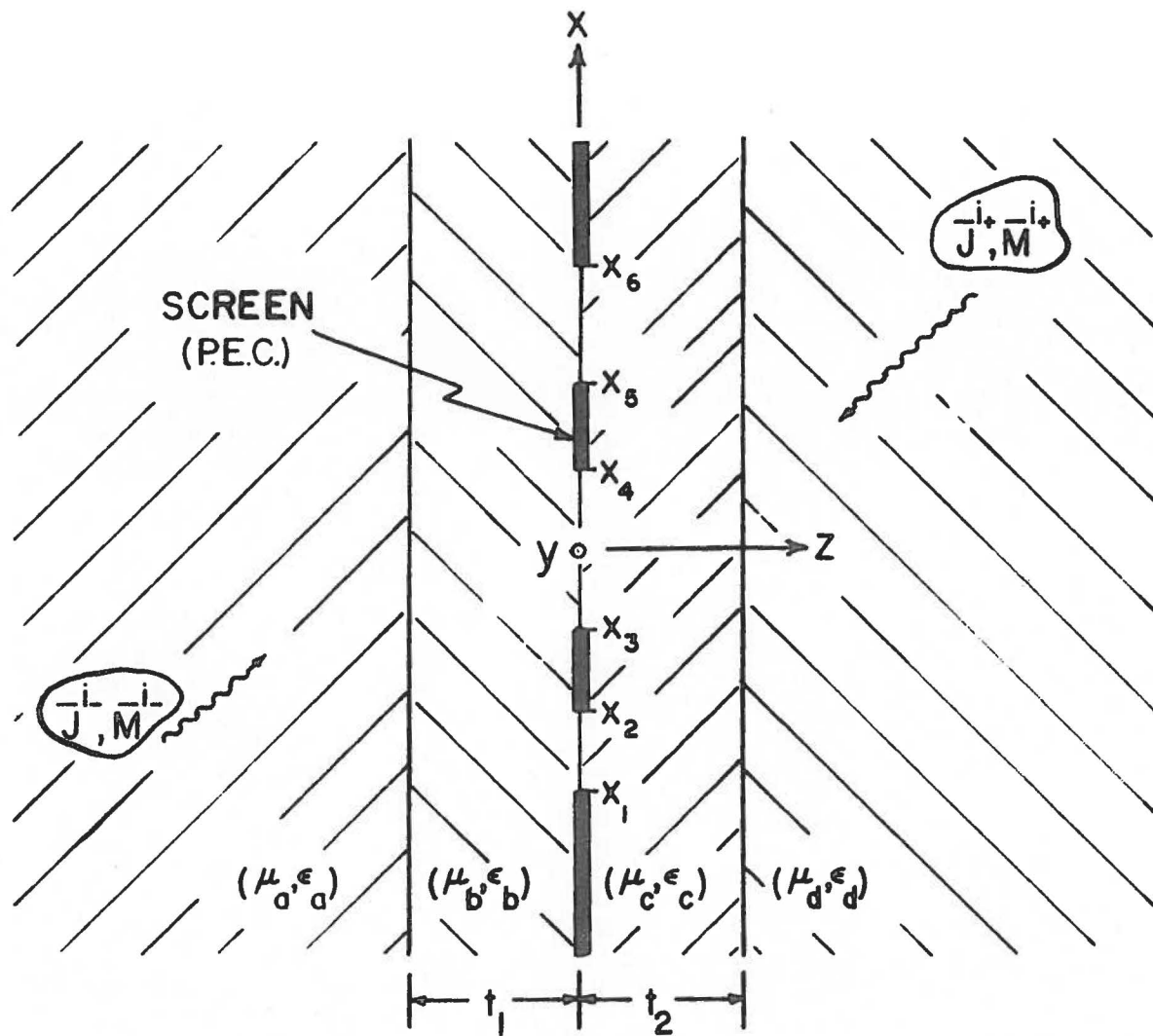


Fig. 2.5 TE illumination of a perfectly conducting screen perforated by several slots of infinite extent and covered on both sides by dielectric slabs.

the left and right sides of the conducting screen and then require continuity of magnetic field through the slots. As a practical example, integral equations are written for the case in which the screen is perforated by two slots, lying in the regions, $x_1 \leq x \leq x_2$ and $x_3 \leq x \leq x_4$, in the conducting screen (Fig. 2.5).

For the case of TE excitation the appropriate integral equations for the case of a dielectric slab-covered perfectly-conducting screen perforated by two slots of infinite extent are:

$$F_y^b(x) + F_y^c(x) = -\frac{j}{\omega} (H_y^{sc})^b(x) - H_y^{sc}(x) , \quad x_1 \leq x \leq x_2 \quad (2.26a)$$

$$F_y^b(x) + F_y^c(x) = -\frac{j}{\omega} (H_y^{sc})^b(x) - H_y^{sc}(x) , \quad x_3 \leq x \leq x_4 \quad (2.26b)$$

where

$$F_y^b(x) = \int_{x'=x_1}^{x_2} 2M_{y1}(x') G_b(x, x') dx' + \int_{x'=x_3}^{x_4} 2M_{y2}(x') G_b(x, x') dx' \quad (2.27a)$$

$$F_y^c(x) = \int_{x'=x_1}^{x_2} 2M_{y1}(x') G_c(x, x') dx' + \int_{x'=x_3}^{x_4} 2M_{y2}(x') G_c(x, x') dx' \quad (2.27b)$$

with

$$M_{y1}(x) = E_x^{a1}(x)$$

$$M_{y2}(x) = E_x^{a2}(x)$$

E_x^{a1} and E_x^{a2} are the tangential electric fields in slots one and two, respectively, and $G_b(x, x')$ and H_y^{sc} are as defined in Section 2.1.

While Eqs. (2.26) are similar in form, each of these equations is applied in a different slot as indicated by the constraint relations given. It is now necessary to solve Eqs. (2.26) by numerical methods dealing with coupled integral equations.

CHAPTER III

SCATTERING OF SURFACE WAVES BY A NOTCH IN A PERFECTLY CONDUCTING INFINITE SCREEN COVERED BY A DIELECTRIC SLAB

The general problem of a shorted parallel plate guide (notch) opening into a perfectly conducting infinite ground screen covered by a dielectric slab is shown in Fig. 3.1. It is assumed here that the fields in the dielectric slab and in the parallel plate region of the notch are invariant in the y -direction. Fields incident from the exterior region of the notch are assumed to be surface waves which could emanate from a variety of sources. Possible sources include an infinite magnetic line source parallel to the y -axis and any one of the TE-excited dielectric covered slots mentioned in the previous chapter that are illuminated from the $z < 0$ region. For the sake of simplicity, we assume that if excitation is due to a line source then the line source lies at such a distance in $|x|$ from the slot-aperture of the notch that only the surface wave modes present in the dielectric slab are incident upon the notch. It is also assumed that the surface wave modes are TM to the direction of propagation in the dielectric slab.

A companion problem to the one presented here is that of a parallel plate guide excited from inside the guide by a generator. This problem has been dealt with extensively by C.P. Wu [6,41]. The 'notch' problem considered in this chapter is investigated with the objective of studying the radiation properties of surface waves guided by a dielectric over a ground screen which encounter surface discontinuities in the screen.

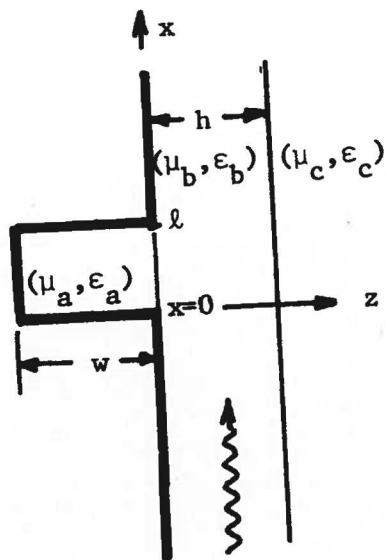


Fig. 3.1 TM surface wave excitation of a 'notch' in a ground screen covered by a dielectric slab.

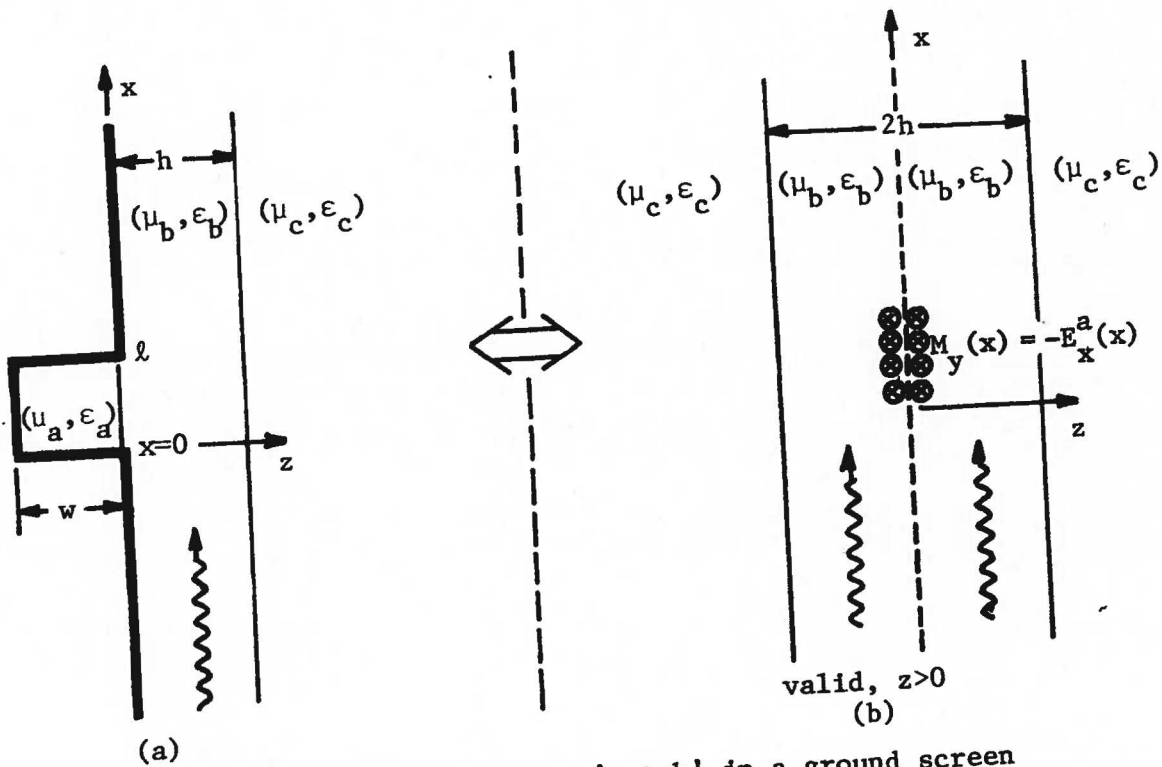


Fig. 3.2 Equivalent problem of a 'notch' in a ground screen covered by a dielectric slab, valid for $z > 0$.

3.1 General Formulation of the Integral Equations

The groundwork as laid down in Chapter II of this paper is used to formulate the integral equation for the general problem depicted in Fig. 3.1. It is known from the equivalence principle that one can short circuit the slot, in this case with a perfect electric conductor (P.E.C.), and place the appropriate magnetic surface currents over the shorted slot both inside the guide and outside on the infinite planar screen. The equivalence principle, however, is used to obtain an expression for the magnetic field in the exterior region ($z > 0$) only. One can find the interior region magnetic field by first obtaining the interior region electric vector potential $\bar{F}_y(x,y)$ in terms of the aperture electric field. The interior magnetic field ($z < 0$) can then be written in terms of the interior electric vector potential as

$$\bar{H}_y(x,z)\hat{y} = -j\omega \bar{F}_y(x,y)\hat{y} \quad (3.1)$$

where \bar{F}_y is the vector potential expressed as a function of the electric field in the slot and is modified for cases of computational interest.

The equations for the magnetic field in the region $z > 0$ may be obtained by again appealing to the equivalence principle in the manner covered explicitly in Chapter II. The magnetic current is specified to be in the negative y -direction as shown in Fig. 3.2(b). Since it is not necessary to preserve the definition of the electric vector potential on the two sides of the slot, as was done for each case in Chapter II, the minus sign in front of the definition of vector potential is retained for both regions. The magnetic field for $z > 0$ is therefore written

$$H_y^+(x, z) = -j\omega F_y^+(x, z) + H_y^{sc+}(z) \quad (3.2)$$

Here, it is understood that the general symbol $F_y^+(x, z)$ is used to represent the electric vector potential in both regions (b) and (c).

In the introduction to the present chapter it is mentioned that, although one could find the fields incident upon the slot in terms of a Sommerfeld integral involving a magnetic line current, it is more desirable to formulate the equation assuming excitation due to the surface wave modes. This, in the final analysis, gives a solution more latitude, in that one is not limited to a single technique for exciting surface waves.

If we now force the transverse component H_y of the magnetic field to be continuous through the slot, then all conditions for the existence of electromagnetic fields are satisfied. This operation is applied as follows

$$\lim_{z \uparrow 0} (\bar{H}_y^-(\bar{r}) \times \hat{z}) = \lim_{z \downarrow 0} (\bar{H}_y^+(\bar{r}) \times \hat{z}), \quad (x, y) \in A \quad (3.3)$$

Employing (3.1) and (3.2) in (3.3) we have finally

$$F_y^- - F_y^+ = \frac{j}{\omega} H_y^{sc+} \quad (3.4)$$

where H_y^{sc+} is that value of magnetic field that would exist on the conducting screen in the region of the slot if the slot were not present.

Utilizing the Green's function derived in Appendix A for the vector potential $F_y^+ = F_y^b$, the terms in Eq. (3.4) may be written as follows

$$\begin{aligned}
 F_y^- = & -\frac{\epsilon_a}{\ell k_a} \cot(k_a w) \int_{x'=0}^{\ell} E_x^a(x') dx' \\
 & + \frac{2\epsilon_a}{\ell} \sum_{n=1}^{\infty} \left[\frac{\cos(\frac{n\pi x}{\ell})}{\gamma_n^a} \coth(\gamma_n^a w) \int_{x'=0}^{\ell} E_x^a(x') \cos(\frac{n\pi x'}{\ell}) dx' \right] \quad (3.5)
 \end{aligned}$$

and

$$\begin{aligned}
 F_y^+ = & \frac{j\epsilon_b}{2} \int_{x'=0}^{\ell} E_x^a(x') \left[-\frac{4}{\pi} \int_{k_x=0}^{\infty} \left(\frac{\Gamma_k e^{-j\beta_b 2h}}{1 + \Gamma_k e^{-j\beta_b 2h}} \right) \frac{\cos k_x (x-x')}{\beta_b} dk_x \right. \\
 & \left. + H_0^{(2)}(k_b |x-x'|) \right] dx' \quad (3.6)
 \end{aligned}$$

$$H_y^{sc+} = H_0 e^{-jk_s (x-\ell/2)} \quad (3.7)$$

where as before

$$\Gamma_k = \frac{\epsilon_b \beta_c - \epsilon_c \beta_b}{\epsilon_b \beta_c + \epsilon_c \beta_b}$$

$$\beta_c = \begin{cases} \sqrt{k_c^2 - k_x^2}, & k_x < k_c \\ -j \sqrt{k_x^2 - k_c^2}, & k_x > k_c \end{cases}$$

$$\gamma_n^a = \sqrt{(\frac{n\pi}{\ell})^2 - k_a^2}$$

The values of the propagation constant $k_x = k_s$ for which the surface waves occur may be found by referring to the methods of Appendix C or numerically by the methods mentioned in Chapter IV.

A restriction that $\lambda_a/2 > l > 0$ is placed upon the width dimension of the notch. This implies that, only the lowest order $n=0$ (TEM) mode propagates in the parallel plate region of the notch. Eq. (3.7) is a representation for the surface wave traveling in the dielectric slab. This surface wave representation may be normalized to the center of the slot by setting $H_0 = 1$. The phase term $\exp(jk_s l/2)$ is included in Eq. (3.7) so that the surface wave is phase referenced to the center of the slot.

The first term on the R.H.S. of Eq. (3.5) is the standing wave portion of the total field in the guide which is caused by a reflection of the field between the slot discontinuity and the guide short circuit. In the general vector potential formula this term is associated with the magnitude of the dominant TEM mode in the guide. The second term in (3.5) is the result of higher order modes which are produced by the slot discontinuity. These modes decay rapidly with respect to distance and therefore cannot be detected at points very far removed from the slot, inside the guide ($z < 0$). The effect of higher order modes, however, not only significantly changes the usually assumed lowest order TEM mode characteristic shape of the slot fields but also to a lesser extent alters the far field radiation pattern.

3.2 Scattering Parameters

A scattering matrix is particularly useful in characterizing the response of a structure at microwave frequencies. The scattering matrix

method is utilized in this chapter to analyze the scattering of surface waves from a notch discontinuity. For a detailed discussion of the scattering matrix method the reader should refer to Collin [34].

The scattering matrix representation for the present case is that of a two port network where the observation planes are taken to be interior to the slab at planes several wavelengths distant from the notch region. In terms of the incident V^+ and reflected V^- voltage waves, the scattering matrix can be written

$$\begin{bmatrix} V_1^- \\ V_2^- \end{bmatrix} = \begin{bmatrix} S_{11} & S_{12} \\ S_{21} & S_{22} \end{bmatrix} \begin{bmatrix} V_1^+ \\ V_2^+ \end{bmatrix} \quad (3.8)$$

where $S_{11} = S_{22}$ and $S_{12} = S_{21}$.

Interior to the dielectric slab, a much greater portion of the total field is due to surface waves than is due to the radiation field at distances several wavelengths removed from the region of the notch. The scattering parameters are therefore calculated using only the residue (i.e. surface wave) terms of the Sommerfeld integral. This allows the removal of the branch cut integral representing the continuous eigenvalue spectrum of the radiation field from the Sommerfeld integral expression in Eq. (3.6). The scattering parameters for a dielectric slab over a notch perforated ground plane are

$$S_{11} = S_{22} = \frac{j k_b e^{j k_s (2x_1 - \lambda/2)}}{k_s \left[j h + \frac{\epsilon_c \epsilon_b (\beta_c^2 - \beta_b^2)}{\beta_c \Gamma_k^n \Gamma_k^d} \right]} \int_{x'=0}^{\lambda} \left(\frac{E^a(x')}{x' \eta_b H_0} \right) e^{-j k_s x'} dx' \quad (3.9)$$

$$S_{21} = S_{12} = \left\{ 1 - \frac{j k_b e^{-j k_s \lambda / 2}}{k_s \left[j h + \frac{\epsilon_c \epsilon_b (\beta_c^2 - \beta_b^2)}{\beta_c \Gamma_k^n \Gamma_k^d} \right]} \int_{x'=0}^{\lambda} \left(\frac{E_x^a(x')}{n_b H_0} \right) e^{j k_s x'} dx' \right\} x e^{j k_s (x_2 - x_1)} \quad (3.10)$$

where k_s is the surface wave propagation constant and

$$\Gamma_k^n = \epsilon_b \beta_c - \epsilon_c \beta_b$$

$$\Gamma_k^d = \epsilon_b \beta_c + \epsilon_c \beta_b$$

S_{12} can be viewed as the transmission coefficient of a surface wave passing through the notch region and S_{11} the reflection coefficient.

Terminal planes at x_1 and x_2 in the dielectric slab are shown in Fig. 3.

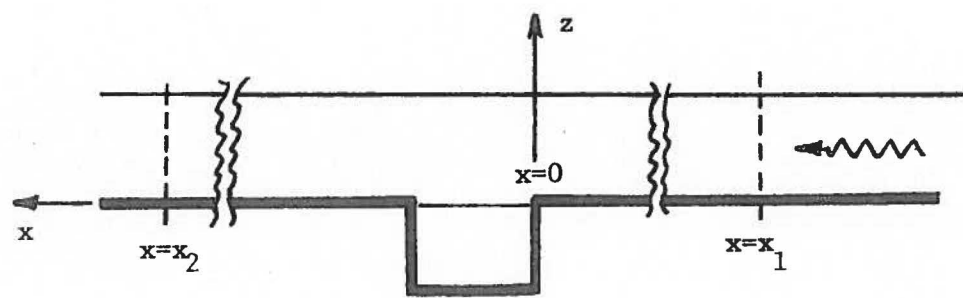


Fig. 3.3 Scattering parameter terminal planes x_1 and x_2 are many wavelengths away from the notch.

CHAPTER IV

NUMERICAL TECHNIQUE

Since the Sommerfeld integral

$$S(x - x') = \int_{k_x = -\infty}^{\infty} \left(\frac{1 - \Gamma_k e^{-j2\beta_b h}}{1 + \Gamma_k e^{-j2\beta_b h}} \right) \frac{e^{jk_x(x-x')}}{\beta_b} dk_x \quad (4.1)$$

derived in Appendix A contains infinite limits of integration over an integrand which exhibits branch point singularities and pole singularities on a branch cut, it is necessary to carefully investigate the numerical techniques which are used for evaluation of this integral. Eq. (4.1) can also be written in the form

$$S(x - x') = \pi H_0^{(2)}(k_b |x - x'|) - 2 \int_{k_x = -\infty}^{\infty} \left(\frac{\Gamma_k e^{-j2\beta_b h}}{\Gamma_k e^{-j2\beta_b h} + 1} \right) \frac{e^{jk_x(x-x')}}{\beta_b} dk_x \quad (4.2)$$

where the first term on the right hand side is a Hankel function of the second kind and zero order.

The rearrangement of terms exhibited in Eq. (4.2) provides us with a segregation of the so-called Sommerfeld correction term (the integral term in Eq. 4.2) from the Hankel function which is referred to as the asymptotic part of the original Sommerfeld integral of Eq. (4.1). Since approximations for the Bessel and Neumann functions which comprise the Hankel function $H_0^{(2)}$ exist in abundance in the literature, we do not here describe in detail a numerical method used for obtaining values of the

Hankel function. Instead, we refer the interested reader to several sources [42,43] containing useful information on the topic of Bessel functions. The remainder of this chapter is concentrated upon the numerical evaluation of the Sommerfeld correction term and a comparison of the real-axis integration method to an integration in the complex k_x -plane around the existing branch cuts.

4.1 Comparison of Original Sommerfeld Integral with the Sommerfeld Correction Term

Although the integrals contained in Eqs. (4.1) and (4.2) are similar in some aspects, these two integrals are seen to differ in two important ways. First of all, the integrand of the correction term in Eq. (4.2) becomes infinite while the integrand of Eq. (4.1) passes smoothly through the branch point $k_x = k_b$. This correction term singularity has been created by the removal of the Hankel function from the original form (4.1). The integrand of the integral form of the Hankel function therefore has a singularity of similar structure but opposite sign from that of the correction term singularity.

The second way in which the correction term in Eq. (4.2) differs from the original form Eq. (4.1) has to do with the relative rate of convergence of these two integrals. For real axis integration the integrand of the original form of the Sommerfeld integral has a very slow rate of decay as does the integrand of the integral form of the Hankel function in Eq. (4.2). The correction term integrand however, has a relatively rapid rate of decay in most instances. When $\text{Re } k_x$ is large, $\Gamma_k e^{-j2\beta_b h} \approx 0$

so that one may approximate

$$\int_{k_x=L}^{\infty} \left(\frac{1 - \Gamma_k e^{-j2\beta_b h}}{1 + \Gamma_k e^{-j2\beta_b h}} \right) \frac{e^{jk_x(x-x')}}{\beta_b} dk_x \approx \int_{k_x=L}^{\infty} \frac{e^{jk_x(x-x')}}{\beta_b} dk_x$$

where L is a large number. Since the Hankel function has the integral form

$$\pi H_0^{(2)}(k_b |x-x'|) = \int_{k_x=-\infty}^{\infty} \frac{e^{jk_x(x-x')}}{\beta_b} dk_x$$

it can be concluded that subtracting out the Hankel function from the original Sommerfeld integral has the effect of removing the asymptotic part of the original integral. The limits of numerical integration for the correction term are therefore not excessively large when the value of the correction term integral is placed within some reasonable bound.

If limits $k_x = \pm L$ are placed upon the real axis numerical integration of the Sommerfeld correction term, then the correction term may be written in the following way

$$\begin{aligned} & \int_{k_x=-\infty}^{\infty} \left(\frac{\Gamma_k e^{-j2\beta_b h}}{\Gamma_k e^{-j2\beta_b h} + 1} \right) \frac{e^{jk_x(x-x')}}{\beta_b} dk_x \\ & \approx \int_{k_x=-L}^L \left(\frac{\Gamma_k e^{-j2\beta_b h}}{\Gamma_k e^{-j2\beta_b h} + 1} \right) \frac{e^{jk_x(x-x')}}{\beta_b} dk_x + R_1 \end{aligned} \quad (4.3)$$

where

$$R_1 = j2C \int_{k_x=L}^{\infty} \frac{e^{-2k_x h} \cos k_x (x-x')}{k_x} dk_x \quad (4.4a)$$

with

$$C = \frac{\epsilon_b - \epsilon_a}{\epsilon_b + \epsilon_a} \quad (4.4b)$$

It is noted that $|C|$ can never be greater than one. Since the term $\cos k_x (x-x')$ is oscillatory and therefore does not contribute to the approximate remainder term R_1 , the following criterion is used in placing a bound upon this neglected part of the Sommerfeld correction term:

$$\begin{aligned} \left| j2C \int_{k_x=L}^{\infty} \frac{e^{-2k_x h} \cos k_x (x-x')}{k_x} dk_x \right| &\leq 2|C| \int_{k_x=L}^{\infty} \left| \frac{e^{-2k_x h}}{k_x} \right| dk_x \\ &= 2|C| \int_{k_x=L}^{\infty} \frac{e^{-2k_x h}}{k_x} dk_x \quad (4.5) \end{aligned}$$

Letting $t = 2k_x h$, one may rearrange Eq. (4.5) to obtain

$$|R_1| \leq 2|C| \int_{k_x=L}^{\infty} \frac{e^{-2k_x h}}{k_x} dk_x = 2|C| \int_{t=2hL}^{\infty} \frac{e^{-t}}{t} dt = 2|C| E_1(2hL)$$

where $E_1(z)$ is an exponential integral and may be placed in series form

$$E_1(z) = -\gamma - \ln z - \sum_{n=1}^{\infty} \frac{(-1)^n z^n}{n! n} , \quad |z| \leq 10.0 \quad (4.6a)$$

$$E_1(z) = \frac{e^{-z}}{z} \left(1 - \frac{1}{z} + \frac{2}{z^2} - \frac{2 \cdot 3}{z^3} + \dots \right) , \quad |z| > 10.0 \quad (4.6b)$$

where $\gamma = .57721$ is Euler's constant and z is a general complex number.

The total error resulting from the numerical evaluation of the left hand side of (4.3) is obtained by taking a ratio of $|R_1|$ with the numerical value of the first term on the right hand side of (4.3). Successively increasing values of L lead to successive improvement in the error. Sufficient accuracy is obtained when a ratio of less than 10^{-4} is reached.

Another possible method for evaluating the Sommerfeld integral in Eq. (4.2) involves closing the integration contour in the upper half k_x -plane with $x-x'$ changed to $|x-x'|$. Eq. (4.2) is then seen to be equal to the integral around the branch cuts which are the result of evaluating the square root β_a and β_b terms in the upper half k_x -plane. This branch cut integration path is shown in Fig. 4.1b, and is mathematically equal to the real axis integration in Fig. 4.1a, so

$$\int_B f(k_x |x-x'|) dk_x = \int_R f(k_x, x-x') dk_x \quad (4.7a)$$

where $f(k_x, x-x')$ is the integrand of Eq. (4.2) and

$$f(k_x |x-x'|) = \left(\frac{\Gamma_k e^{-j2\beta_b h}}{1 + \Gamma_k e^{-j2\beta_b h}} \right) \frac{e^{jk_x |x-x'|}}{\beta_b} \quad (4.7b)$$

and $k_x' = k_x' + jk_x''$, a complex number. It is noted that the integration over the semi-circular contour at infinity is zero provided one strictly adheres to the choice of branch cut paths indicated in Appendix A.

Integration along the branch cut provides one with a numerical problem similar to that of integration along the real axis. Along the branch cut the integrand decays as the integration variable k_x' increases along the imaginary axis. The dominant term generating the decay in Eq. (4.7b) is $\exp[-k_x''|x-x'|]$. Obvious similarities between the real axis integral and the branch cut integral lead us to conclude that the branch cut integral is also amenable to numerical integration as long as $|x-x'|$ is a significant number. The neglected part of the branch cut correction term integral may be approximated by

$$R_2 = j \int_M^\infty \left(\frac{Ce^{-j2k_x''h}}{1 + Ce^{-j2k_x''h}} \right) \frac{e^{-k_x''(x-x')}}{k_x''} dk_x'' \quad (4.8)$$

where k_x'' indicates integration on the imaginary axis, C is defined in Eq. (4.4b) and M is a large number. A bound may be placed upon the remainder term R_2 in a manner similar to that used for the real axis integral.

Applying the above mentioned bounding procedure, we get

$$|R_2| \leq \left(\frac{|C|}{1 - |C|} \right) \int_{k_x=M}^\infty \frac{e^{-k_x|x-x'|}}{k_x''} dk_x'' = \left(\frac{|C|}{1 - |C|} \right) E_1(M|x-x'|) \quad (4.9)$$

where $E_1(z)$ is the exponential integral defined in Eqs. (4.6a, b).

For this paper, we have chosen a combination of the two integration procedures pictured in Fig. 4.1 . A numerical switch is employed which makes a decision, based upon the relative sizes of $|x-x'|$ and h , of either integrating along the real axis entirely, Fig. 4.1(a), or integrating only on the branch cut, Fig. 4.1(b). If $|x-x'|$ is greater than h then only the branch cut method is used, otherwise the real axis integration method is used.

It should also be pointed out that in most Sommerfeld integral forms, oscillations of the integrand are a prime consideration. Oftentimes, these oscillations are so rapid that accurate real axis numerical integration becomes very time consuming or impossible. A study of the Sommerfeld integral used in this paper shows that these oscillations are due mainly to the relative size of the field-point, source-point term $(x-x')$ and to the relative thickness h of the dielectric slab. For the Sommerfeld integral forms used in this paper, when dielectric slab thicknesses and aperture widths are approximately two wavelengths or less, few oscillations occur in the integrand of the Sommerfeld integral evaluated below the evenescent wave region $k_x < k_b$. A graph of the integrand of the Sommerfeld correction term is shown in Fig. 4.2 for a typical set of parameters.

When solving for the fields at a great distance from the aperture, the $(x-x')$ term becomes very large, resulting in a rapidly oscillating integrand for any significant value of k_x . Such a situation may be handled by the steepest descent integration technique and is discussed

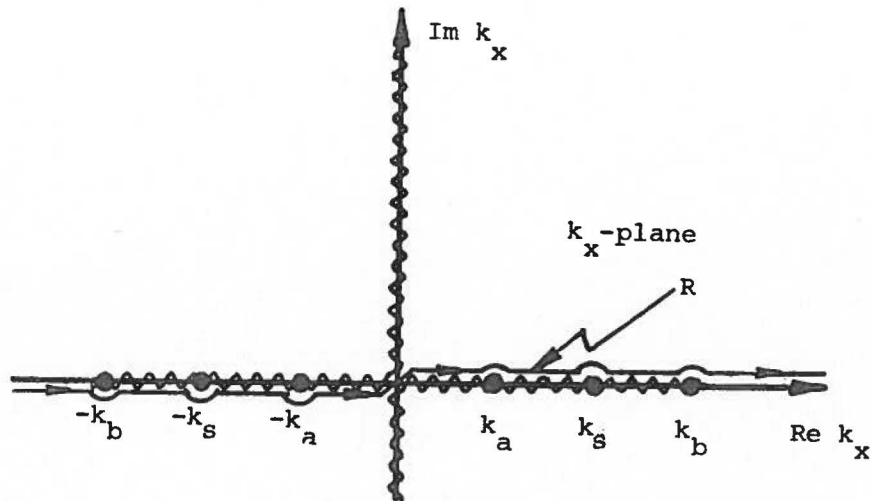


Fig. 4.1(a) Integration contour along the real k_x -axis with $\pm k_a$ and $\pm k_b$ representing branch points and k_s representing a surface wave singularity.

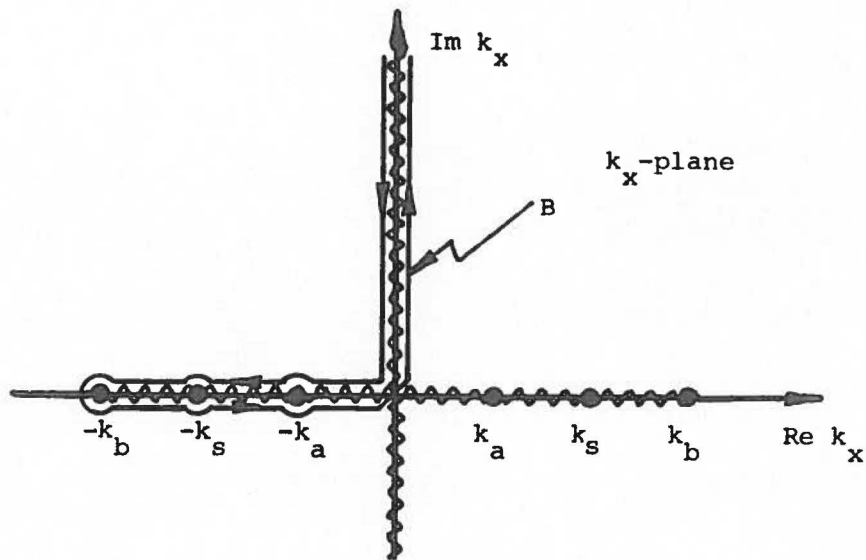


Fig. 4.1(b) Integration contour deformed around the branch cut in the upper half plane.

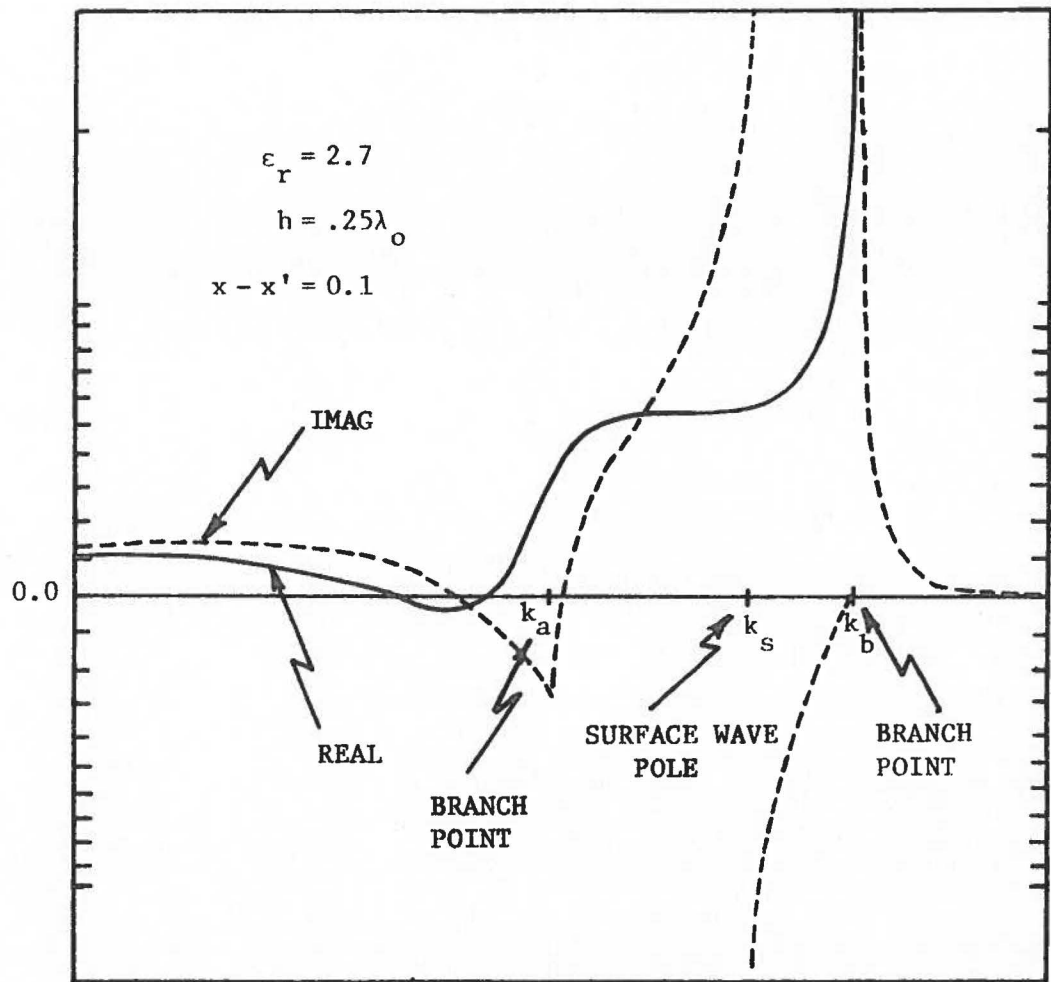


Fig. 4.2 Typical kernel of the Sommerfeld correction term evaluated in the slot for the case of TE incident illumination.

in Appendix (B). A graph of the Sommerfeld correction term given in Eq. (A.16) for a typical set of parameters is shown in Fig. 4.3 for various angles of observation.

A numerical test was run to determine the accuracy of the saddle point integration procedure. In this test, a numerical integration of the Sommerfeld correction term of Eq. (A.16) is carried out by use of a 96 order Gaussian quadrature integration scheme and the results are compared with those of the saddle point integration method. It should be pointed out that, when variations in the integrand of Eq. (A.16) become very rapid, the Gaussian quadrature scheme can be expected to give only a relative indication as to the value of the integral. Results of the Gaussian quadrature versus saddle point integration methods are shown in Table 4.1. In general, the comparison is good, however the steepest descent method results represent a savings in computer computation time of a hundred fold over the Gaussian quadrature method results.

4.2 Singularities Along the Path of Integration

4.2a Types of Singularities

Two types of singularities occur in the Sommerfeld correction term integrand. Branch points singularities occur at k_b and k_a , which are wave numbers for the dielectric and free space regions respectively. Singularities of a different nature occur on the real k_x -axis between $\text{Re}(k_a)$ and $\text{Re}(k_b)$ due to zeros of the $(\Gamma_k^e - j2\beta_b h + 1)$ term in the denominator of the Sommerfeld correction integral. This second type of singularity accounts for the onset of surface waves.

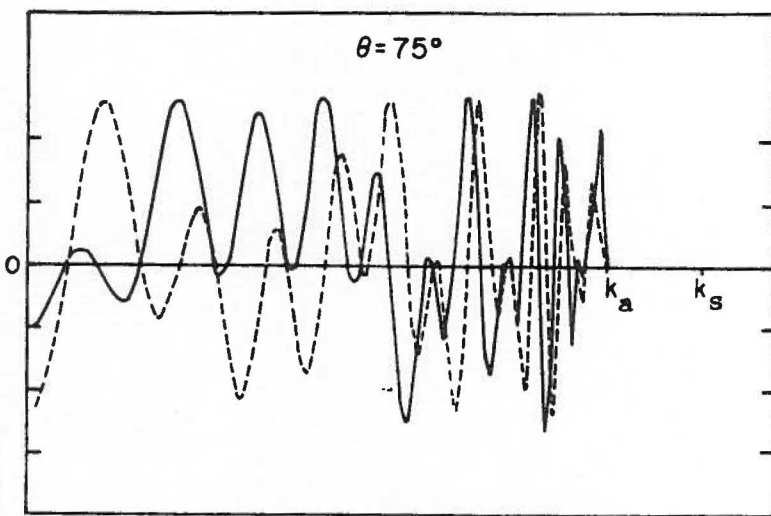
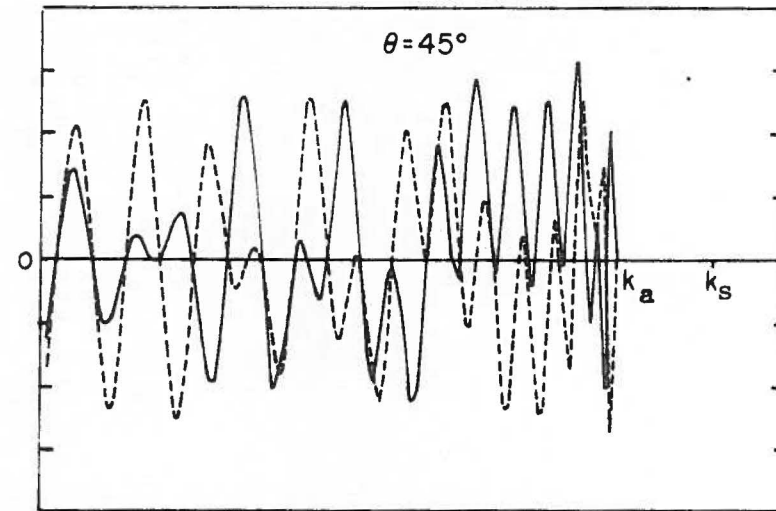
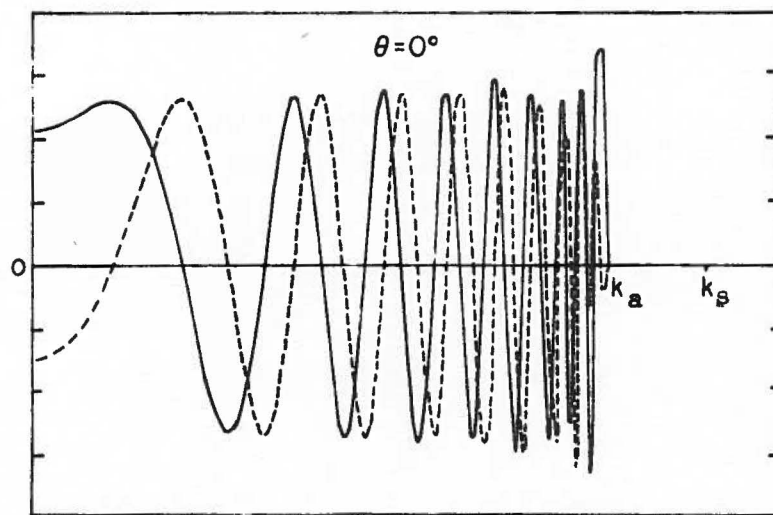
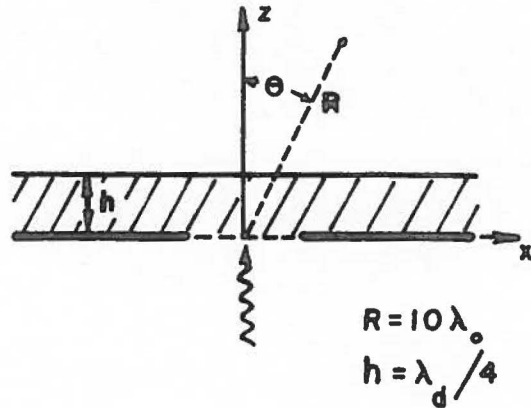


Fig. 4.3 Far field kernel of Sommerfeld correction term for a TE slot as a function of angle where (—) real and (----) imag.

OBSERVATION ANGLE (DEGREES)	NUMERICAL INTEGRATION METHOD		SADDLE POINT METHOD	
	REAL	IMAGINARY	REAL	IMAGINARY
0.00	8.502768	-0.4807813	8.496697	-0.3553188
10.00	8.279802	-0.3759933	8.280612	-0.2961241
20.00	7.698076	-0.2034106	7.658218	-0.1538278
30.00	6.702013	0.1656364	6.711096	-0.0166294
40.00	5.565812	0.3139000	5.571622	0.0233119
50.00	4.414089	0.0646260	4.381554	-0.0749106
60.00	3.188560	-0.1751078	3.226487	-0.2757561
70.00	2.018372	-0.4441655	2.105364	-0.4665410
80.00	0.860945	-0.4257846	0.993869	-0.4501766

Table 4.1 Numerical results showing a comparison of the Gaussian quadrature versus saddle point integration methods for a slab of thickness $\lambda_d/4$ and slot width $\lambda_o/2$.

It is not mathematically proper to describe the surface wave singularities as poles since by virtue of their location (i.e., on a branch cut) every point in a region around these singularities is not analytic. It has been assumed that the top sheet (Fig. 4.1) is the proper sheet for carrying out the necessary complex plane integrations. We therefore cannot include the bottom k_x -plane (not shown) when describing a region about the surface wave singularity.

In a practical sense however, k_a and k_b must contain some loss in order to provide the integral equation solutions with an exponential decay necessary for satisfaction of the radiation condition. An exaggerated picture of such a situation is shown in Fig. 4.4 . The addition of a small amount of decay has moved the branch points at $\pm k_a$ and $\pm k_b$ off the real axis and has caused a separation of the two original branch cuts into four separate branch cuts. The surface wave singularities become separated from the branch cuts. Every point in a region around each surface wave singularity is now analytic so that one can now legitimately refer to surface wave singularities as poles. Taking the limit as loss approaches zero one can show that the situation shown in Fig. 4.4 reduces to that pictured in Fig. 4.1 . In the subsequent paragraphs we assume that some small but detectable loss exists in both the free space and dielectric regions.

The purpose of the preceding discussion is to allow us to use a theorem of complex variables which states that integration around a pole of a function in the complex plane, in the counterclockwise direction,

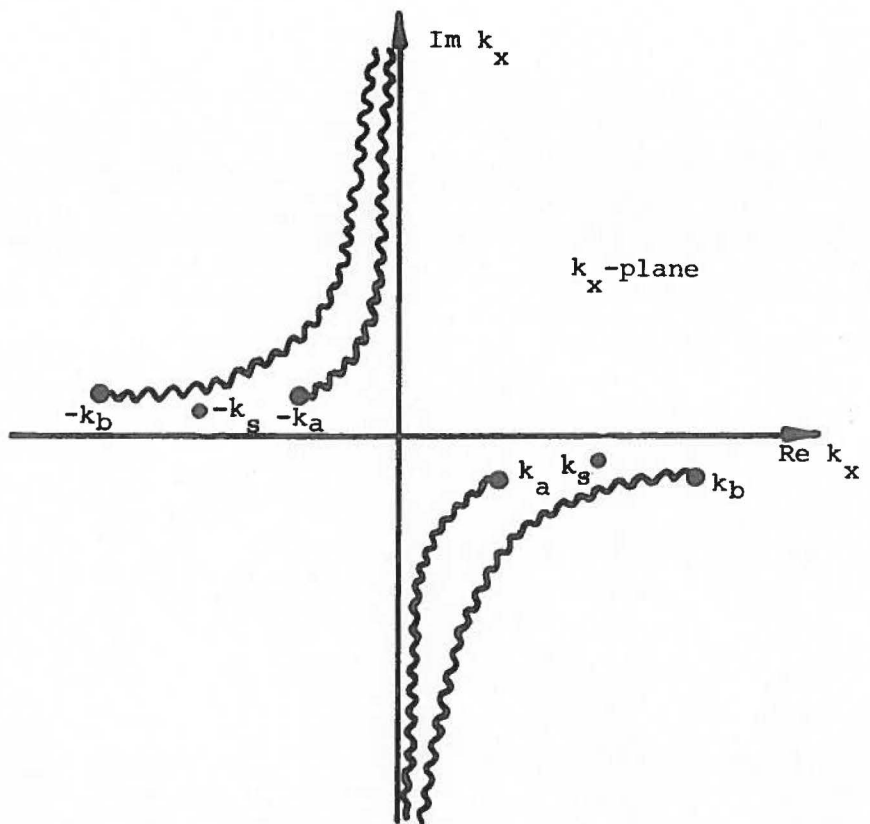


Fig. 4.4 Branch cuts removed from the axis due to the introduction of loss in the k_a and k_b propagation constants.

is equal to $2\pi j$ times the residue of that function evaluated at the enclosed pole. Since integration in this case for both Fig. 4.1(a) and Fig. 4.1(b) is on a semi-circle around the pole, the half residue formula, πj (Residue), is used here.

Rather than carry out this integration numerically, it was found much more efficient to analytically evaluate the residue. Each residue at the surface wave poles in Eq. (4.2) is evaluated by

$$\text{Res} = (k_x - k_s) \left(\frac{\frac{-j2\beta_b h}{e^{\frac{-j2\beta_b h}{k}} + 1}}{\Gamma_k e^{\frac{-j2\beta_b h}{k}}} \right) \left. \frac{e^{jk_x(x-x')}}{\beta_b} \right|_{k_x = k_s} \quad (4.10)$$

where k_s is the pole position. Since both the numerator and denominator go to zero at $k_x = k_s$ we must apply L 'Hospitals' rule, which results in the following expression

$$\text{Res} = \frac{jk_s(x-x')}{2k_s \left[jh + \frac{\epsilon_a \epsilon_b (\beta_a^2 - \beta_b^2)}{\beta_a \Gamma_N \Gamma_D} \right]}$$

where

$$\Gamma_N = (\beta_a \epsilon_b - \beta_b \epsilon_a)$$

$$\Gamma_D = (\beta_a \epsilon_b + \beta_b \epsilon_a)$$

The relative location of the surface wave poles may be found by a graphical solution procedure commonly found in texts such as Collin [34]. This procedure involves finding the intersection of tangent lines with

circles having radii that vary according to the relative thickness of the dielectric slab. For the various cases of interest in this paper, we have restricted ourselves to the use of only two surface wave modes. This restriction prevents the numerical problem from becoming overly complicated while allowing the dielectric to approach thicknesses greater than a wavelength measured inside the slab. The exact location of each pole is then found by placing the approximate graphical location into a Muller method root solving routine [35]. For numerical results it is assumed in this paper $\epsilon_b / \epsilon_a = 2.7$.

4.2b Method of Handling Singular Integrals

Integration is carried out between the singularities on the path of integration of the Sommerfeld correction term Eq. (4.2) by use of a low order Gaussian quadrature numerical integration routine. It has been noted that, if we integrate up to very close to a surface wave singularity and then deform the integration contour onto a semicircle in the complex plane, the contribution from the semicircular region equals $-\pi j$ times the residue at that pole. The minus sign in front of πj indicates that, in accordance with the conditions of this problem, integration must be carried out in the clockwise direction around the surface wave pole. The integral remaining after the residue has been extracted from the correction term integral is known as a deleted integral.

The correction term can be written as a combination of deleted integral along the real k_x axis and a contribution due to a small semi-circle around branch point singularities at $k_{\frac{a}{b}}$. Since integration

around the branch points at k_x^a and k_x^b is zero in the limit as the radius of the integration contour recedes to zero one is left with a deleted correction integral about surface wave singularities k_s and the branch points k_x^a , k_x^b

$$\text{S.C.} = \int_{k_x=0}^{\infty} \left(\frac{\Gamma_k e^{-j2\beta_b h}}{\Gamma_k e^{-j2\beta_b h} + 1} \right) \frac{e^{jk_x(x-x')}}{\beta_b} dk_x - \pi j \text{Res}(k_s) \quad (4.11)$$

Great care must be exercised when integrating the deleted integral in Eq. (4.11) around the singular points. In order to handle these difficult points a method is used whereby the singular part of the integrand in (4.11) is subtracted out, leaving a smoothly varying integrand plus an integral over just the singular part. For the surface wave singularities, the denominator of the deleted integral in Eq. (4.11) is expanded in a two term Taylor series about the singular point k_s ,

$$1 + f(k_x) = 1 + f(k_s) \overset{=-1}{+} f'(k_s)(k_x - k_s) = f'(k_s)(k_x - k_s)$$

where

$$f(k_x) = \Gamma_k e^{-j2\beta_b h}$$

Over a fixed symmetric region ($k_s - \Delta/2, k_s + \Delta/2$) about the surface wave pole k_s the deleted integral of (4.11) is

$$\begin{aligned}
 \int_{k_x = k_s - \Delta/2}^{k_s + \Delta/2} \frac{f(k_x)g(k_x)}{f(k_x) + 1} dk_x &= \int_{k_x = k_s - \Delta/2}^{k_s + \Delta/2} \left[\frac{f(k_x)g(k_x)}{f(k_x) + 1} - \frac{f(k_s)g(k_s)}{f'(k_s)(k_x - k_s)} \right] dk_x \\
 &\quad + \frac{f(k_s)g(k_s)}{f'(k_s)} \int_{k_x = k_s - \Delta/2}^{k_s + \Delta/2} \frac{1}{(k_x - k_s)} dk_x \quad (4.12)
 \end{aligned}$$

where

$$g(k_x) = \frac{e^{jk_x(x-x')}}{\beta_b}$$

Since the singular part cannot be integrated by ordinary means we must take the Cauchy principal value, which in for this case becomes

$$\int \frac{1}{k_x - k_s} dk_x = 0 .$$

Although, as was mentioned previously, the surface wave singularity is not a pole in the strict sense of the word, the coefficient of the singular part has a value equal to the residue of the correction term integrand at the point k_s given by

$$\text{Res}(k_s) = \frac{f(k_s)g(k_s)}{f'(k_s)} \quad (4.13)$$

The residue of Eq. (4.13) contains either a - or a + sign, depending upon whether integration is above or below the branch cut.

The branch point singularity must be handled in a manner similar to that used for the surface wave singularity. The singular part around the branch point, fortunately can be integrated analytically. After manipulation the final form of Eq. (4.11) is as follows:

$$\begin{aligned}
 S.C. &= \int_{k_x=0}^{\infty} U(k_x) dk_x \\
 &= -j\pi \text{Res}(k_s) + \int_0^{k_s - \Delta/2} U(k_x) dk_x \quad (4.14) \\
 &\quad + \int_{k_s - \Delta/2}^{k_s + \Delta/2} \left[U(k_x) - \frac{\text{Res}(k_s)}{k_x - k_s} \right] dk_x \\
 &\quad + \int_{k_s + \Delta/2}^{k_b - \varepsilon} U(k_x) dk_x \\
 &\quad + \int_{k_b - \varepsilon}^{k_b} \left[U(k_x) - \frac{e^{jk_b(x-x')}}{2\sqrt{2k_b} \sqrt{k_b - k_x}} \right] dk_x \\
 &\quad + \int_{k_b}^{k_b + \varepsilon} \left[U(k_x) - \frac{j e^{jk_b(x-x')}}{2\sqrt{2k_b} \sqrt{k_x - k_b}} \right] dk_x
 \end{aligned}$$

$$\begin{aligned}
 & + \frac{e^{jk_b(k-x')}}{\sqrt{2k_b}} \sqrt{\epsilon} (1+j) \\
 & + \int_{k_b+\epsilon}^{\infty} U(k_x) dk_x
 \end{aligned}$$

where

$$U(k_x) = \left(\frac{\Gamma_k e^{-j2\beta_b h}}{\Gamma_k e^{-j2\beta_b h} + 1} \right) \frac{e^{jk_x(x-x')}}{\beta_b}$$

Here Δ represents a small region around a surface wave pole located at k_s and ϵ represents a small region around the branch point located at k_b .

The behavior of the branch point singularity at $k_x = k_b$ for the case of TM aperture illumination is unlike the behavior of the branch point singularity at the same point in the TE case. By taking the limiting case as k_x approaches k_b in the TM case one finds that the branch point has the behavior of a pole. This means that in the limiting case as R (radius of integration) approaches zero integration around the branch point at k_b will yield a finite contribution to the Sommerfeld correction term for the TM case while for the TE case a similar integration would produce no contribution to the Sommerfeld integral. One can therefore handle the Sommerfeld integral for the case of TM slot illumination by subtracting the singular behavior from the Sommerfeld integral and adding back the analytically determined contribution due to the singular point. The branch point singularity at k_a is bounded and can be handled by

by normal numerical integration methods.

4.3 Numerical Solution to the Integral Equation

The solution for the aperture electric field $E^a(x)$ from the integral equation (Eq. 2.11 and Eq. 2.20) may be obtained by use of the method of moments [40]. Specifically, the aperture is first divided into N segments each of width Δx . Then $E^a(x)$ is expanded into sets of flat pulse basis functions

$$E^a(x) = \sum_{n=1}^{\infty} e_n P_n(x)$$

where e_n are the unknown coefficients to be found and

$$P_n(x) = \begin{cases} 1, & x \in (x_n - \Delta/2, x_n + \Delta/2) \\ 0, & \text{otherwise} \end{cases}$$

Delta function testing is used on Eq. (2.11) while piecewise linear testing in the case of Eq. (2.20) reduces the differential operator to a form equivalent to a numerical difference equation.

CHAPTER V

RESULTS AND CONCLUSIONS

In this chapter numerical results are given showing slot magnetic current (electric field) and far field patterns for selected cases of the problems presented in the previous chapters. Results are obtained as a function of such parameters as dielectric slab thickness, slot width, excitation angle of incidence, and for the case of coupled slots, slot separation distance. For the "notch" problem, results are given as a function of notch depth.

Fig. 5.1 pictures a typical configuration for the numerical results given in this chapter. A ground screen perforated by a slot is covered by a dielectric slab lying on the shadow side of the screen (see Fig. 5.1). The width of the slot is ℓ , the thickness of the dielectric slab is h and the relative dielectric constant of the slab is chosen to be $\tilde{\epsilon}_d = 2.7$. The region outside the slab is chosen to have the electrical properties of free space.

In each of the figures for the case of TE slot excitation (TM surface wave excitation) λ_{s1} represents the slab thickness h at which the second surface wave mode is produced. In each of the figures for the case of TM slot excitation (TE surface wave excitation) λ_{s1} represents the slab thickness at which the first surface wave mode is produced.

5.1 TE Excitation of a Slot in a Ground Screen Covered by a Dielectric Slab

5.1a TE Slot Magnetic Current Distribution

In Fig. 5.2 numerical results are given as a function of dielectric thickness for the case of TE excitation of the slot pictured in Fig. 5.1.

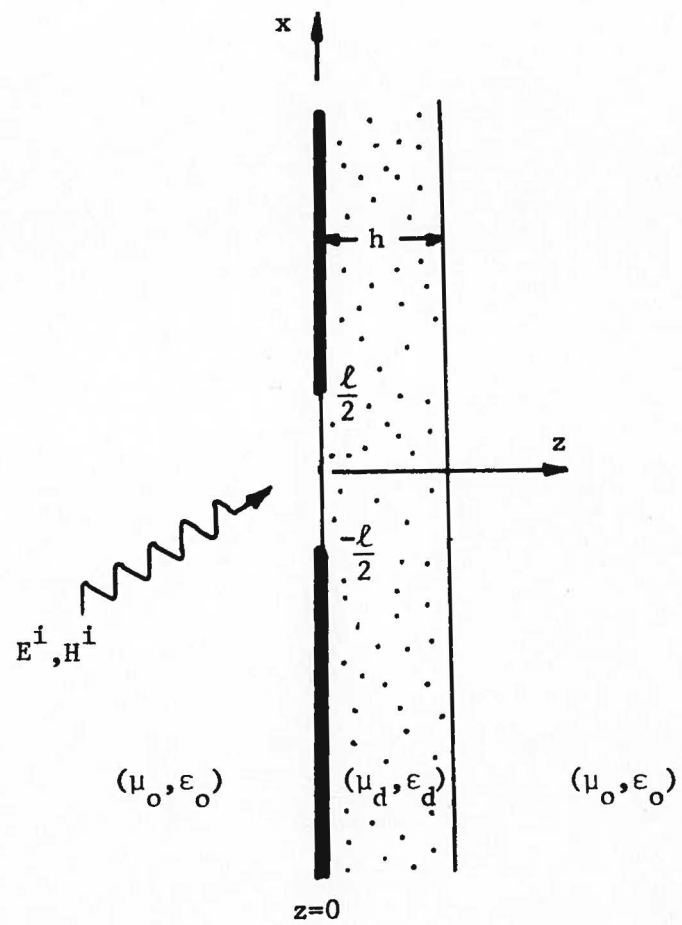


Fig. 5.1 Characteristic setup for parameter studies of this chapter with: ϵ_0 dielectric constant of free space; $\epsilon_d = 2.7 \epsilon_0$; $\mu_d = \mu_0$ permeability of free space.

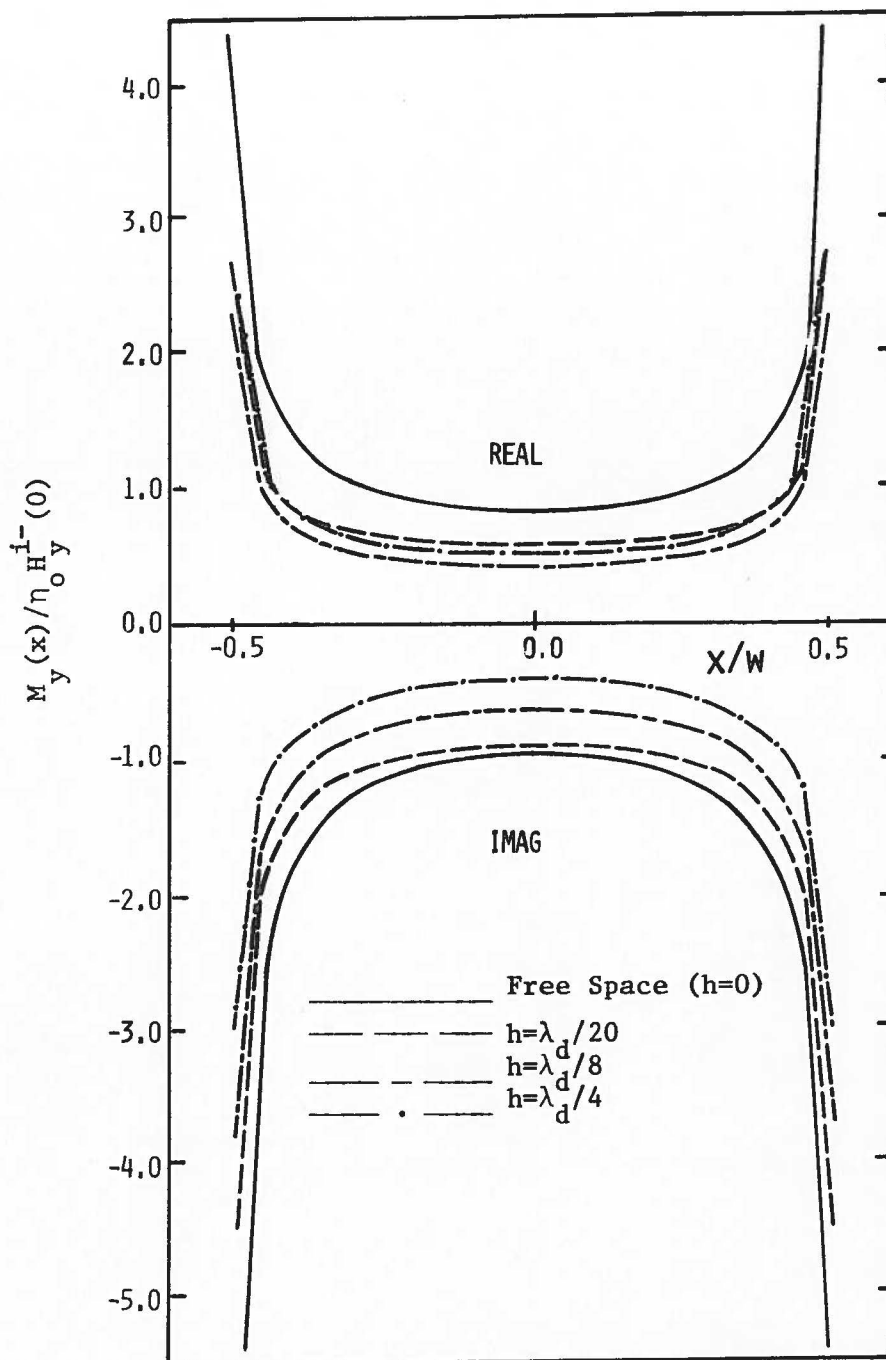


Fig. 5.2a Equivalent magnetic current $M_y(x)$ ($= E_x^a$) for a slot of width $0.1\lambda_o$, subject to normally incident TE excitation for various slab thicknesses.

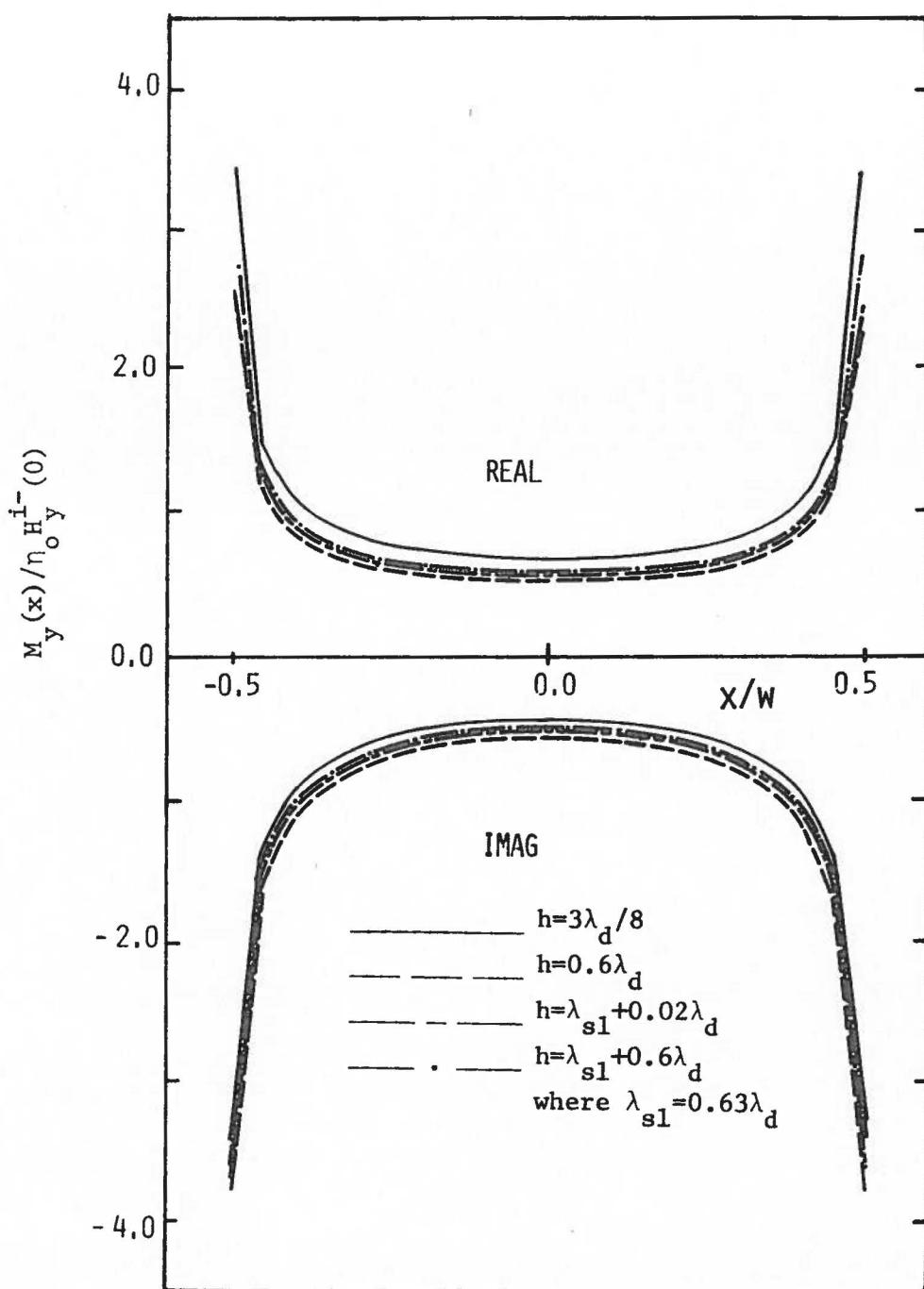


Fig. 5.2b Equivalent magnetic current $M_y(x)$ ($= E_x^a$) for a slot of width $0.1\lambda_o$, subject to normally incident TE excitation for various slab thicknesses.

Fig. 5.2 shows the slot magnetic current distribution normalized by the product of the magnetic field $H_y^1(0)$ incident upon the center of the slot and the free space wave impedance. Thickness h of the slab is given in terms of dielectric slab wavelength λ_d . The term Free Space in each figure indicates a case in which the dielectric slab thickness has receded to zero. The results for the Free Space case are simply those for a slot in a conducting screen situated in free space (i.e. without a dielectric slab). The Free Space case is important since none of the electromagnetic radiation penetrating the screen couples into surface wave modes in the dielectric slab and therefore no interaction between the slot field and the dielectric slab occurs. When compared to the Free Space case, results for all other cases give some indication as to the extent of the coupling between the slot and the dielectric slab. Since, for the case of transverse electric (TE) excitation of a slot at least one transverse magnetic (TM) surface wave mode exists for all slab thicknesses [45], it is expected that surface wave mode coupling is partially responsible for the differences between the Free Space case and each of the other cases pictured in Fig. 5.2.

It is evident that, as the slot becomes larger (see Figs. 5.3, 5.4 and 5.5), then slot-dielectric-slab interaction becomes more pronounced for the various slab thicknesses chosen. For the case of a slot of width $0.1\lambda_o$ very little change is seen in the slot magnetic current for various slab thicknesses as compared to significant changes shown in the case of a slot of width $3.0\lambda_o$ for the same slab thicknesses.

One consequence of the interaction between the slot and the dielectric slab can be related directly to the action of surface waves. It is shown

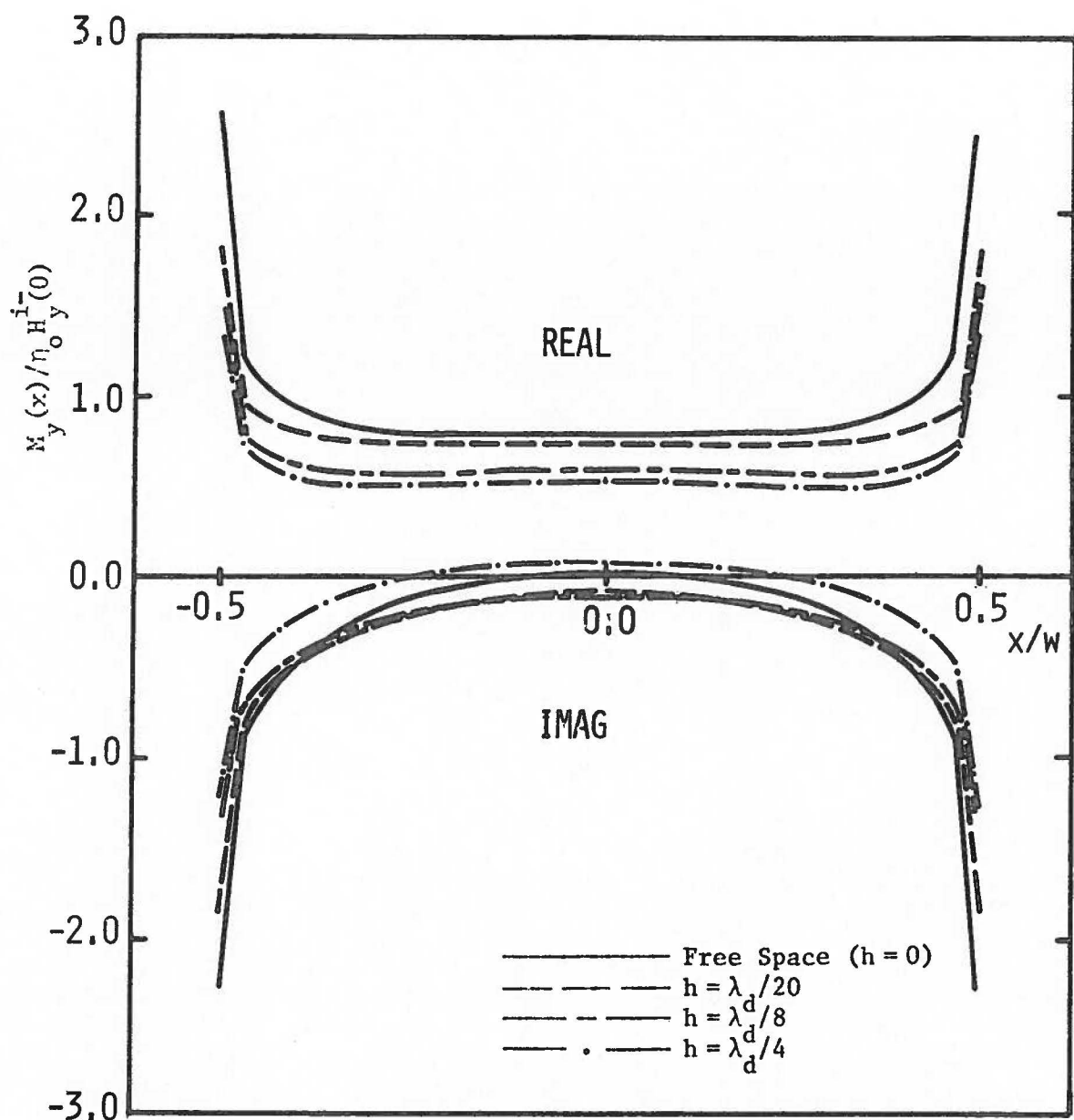


Fig. 5.3a Equivalent magnetic current $M_y(x) (= E_y^a)$ for a slot of width $0.5\lambda_o$, subject to normally incident TE excitation for various slab thicknesses.

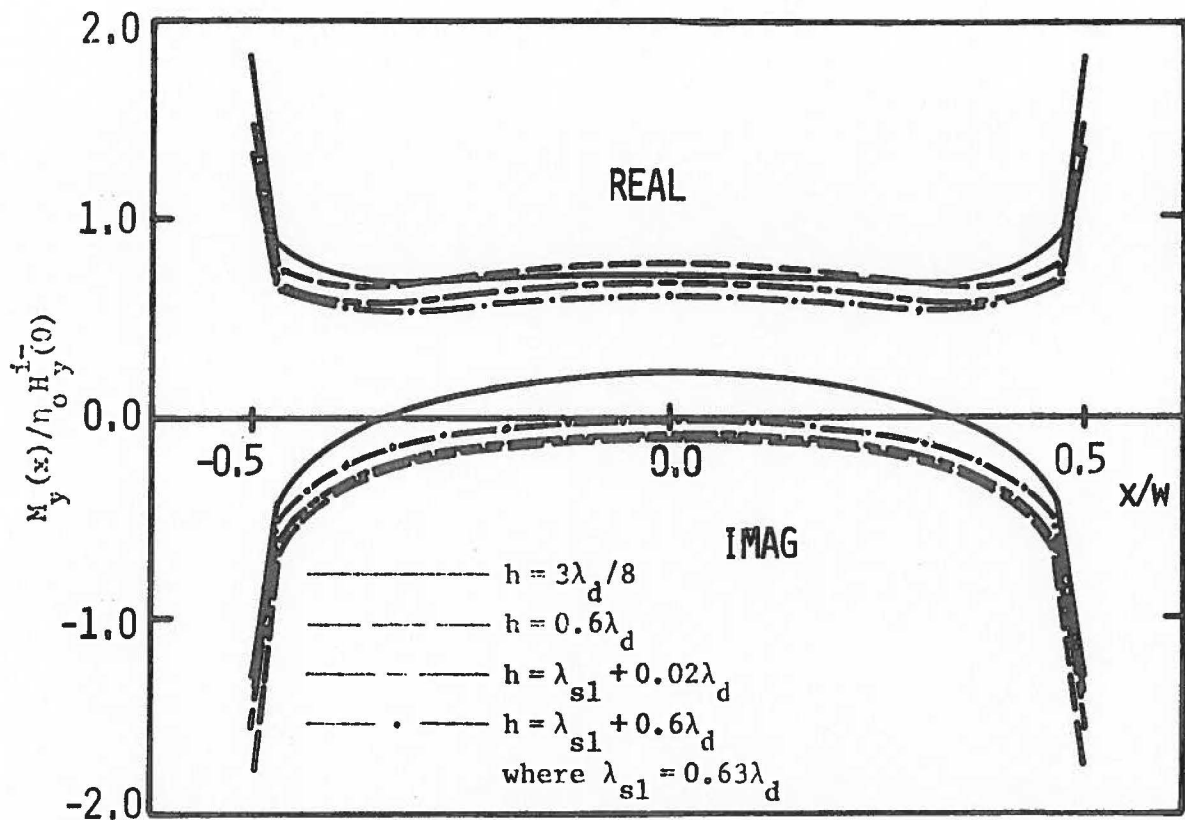


Fig. 5.3b Equivalent magnetic current $M_y(x)$ ($= E_x^a$) for a slot of width $0.5\lambda_o$, subject to normally incident TE excitation for various slab thicknesses.

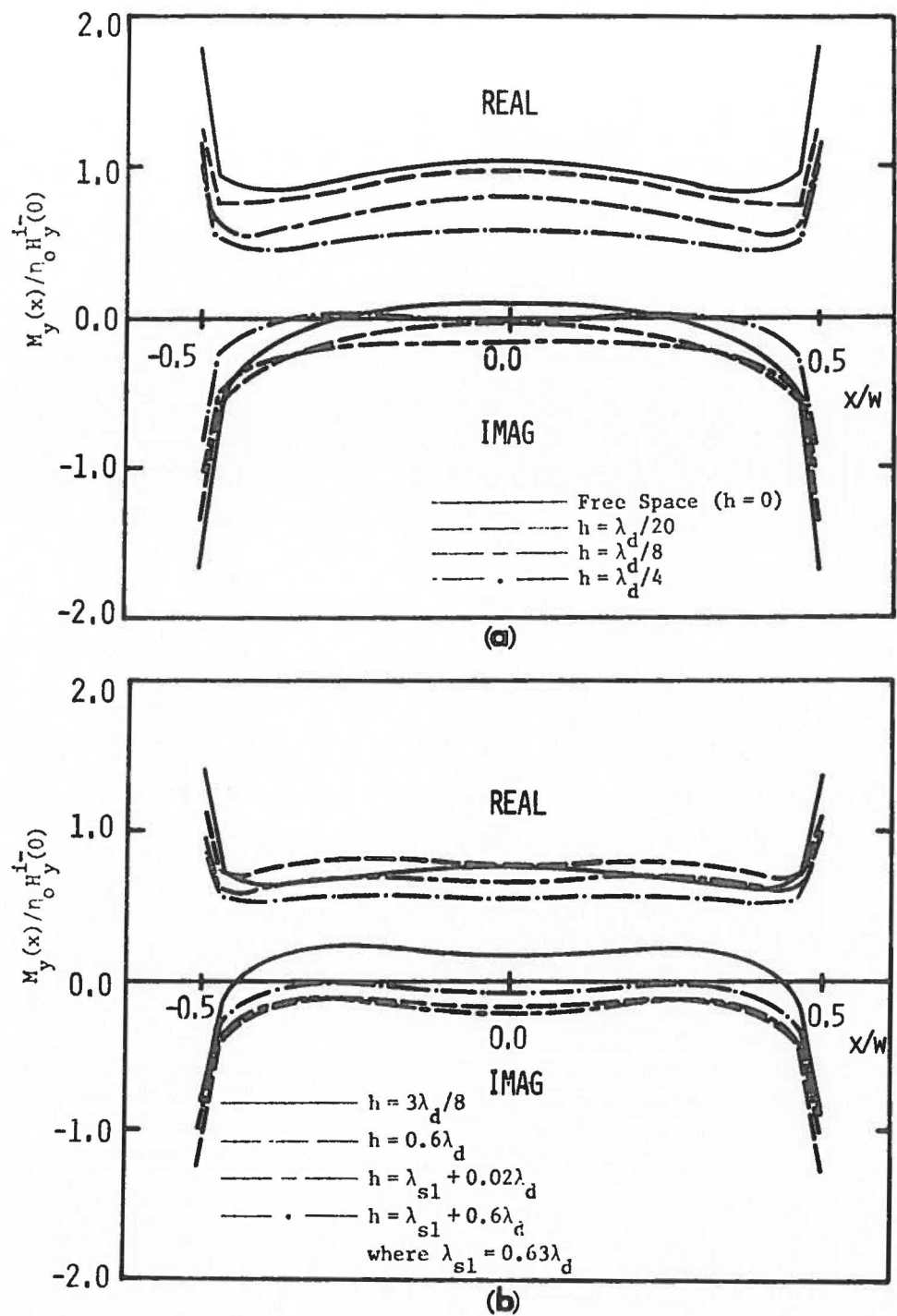


Fig. 5.4 Equivalent magnetic current $M_y(x)$ ($= E_y^a$) for a slot of width $1.0\lambda_o$, subject to normally incident TE excitation for various slab thicknesses.

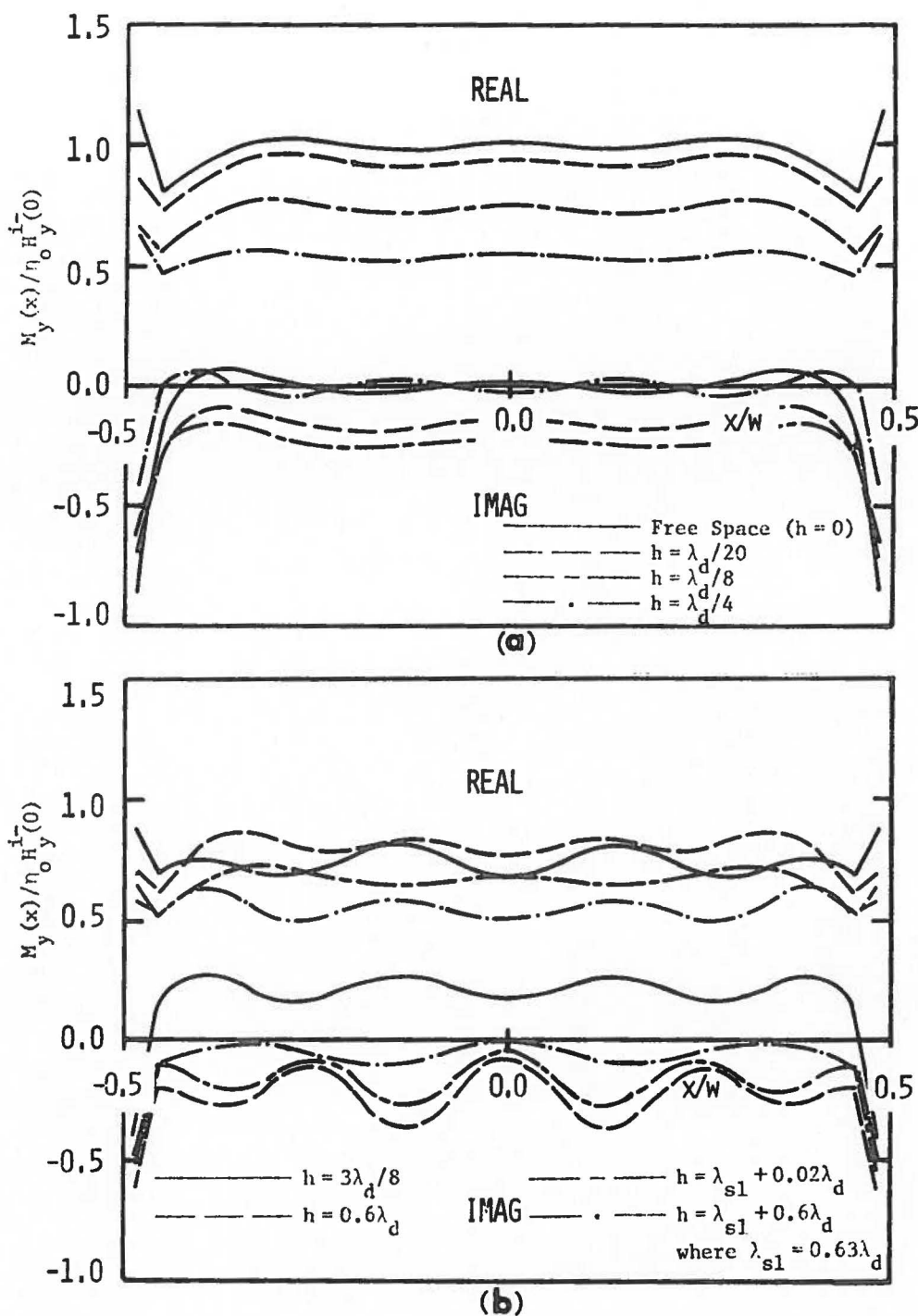


Fig. 5.5 Equivalent magnetic current $M_y(x) (= E_x^a)$ for a slot of width $3.0\lambda_0$, subject to normally incident TE excitation for various slab thicknesses.

in Appendix C that the surface-wave-mode wave number k_s is directly related to the thickness of the dielectric slab. As the thickness of the dielectric slab increases the wave number k_s increases and consequently the wavelength of the surface wave decreases. Surface waves which travel in both the positive and negative x-direction in the dielectric slab are launched at each of the edges of the slot. Surface waves traveling in opposite directions in the slab tend to set up a standing wave pattern which is evident in the slot electric field.

An excellent example of this standing wave interference phenomena is shown in Fig. 5.5(a) for the case of a three wavelength slot. A very thin dielectric slab will produce a surface wave with frequency close to that of the excitation field frequency. The standing wave pattern formed in the case of a thin dielectric slab is relatively undetectable. However, as the thickness of the slab is increased, the frequency of the surface wave increases resulting in a pronounced change in the slot electric fields. As one continues to increase the thickness of the slab a second surface wave is produced at the lower end of the surface wave frequency spectrum. The effect of standing wave pattern due to the second surface wave is not seen until the thickness of the slab is further increased. However the relatively smooth curve shown in Fig. 5.5(b) for the case of a slab thickness near the onset of a third surface wave, tends to indicate that a combination of several standing wave patterns will yield a relatively smooth resultant pattern. Table 5.1 shows the close correlation that exists between the period of the slot electric field standing wave pattern calculated by the integral equation method and the period of the surface wave

DIELECTRIC THICKNESS h	SURFACE WAVE WAVELENGTH λ_s (M)	PERIOD OF SLOT E-FIELD (M)	PERCENT DIFFERENCE
$\lambda_d/20$.99	.95	4%
$\lambda_d/8$.98	.90	8%
$\lambda_d/4$.936	.87	7%
$3\lambda_d/8$.884	.85	4%
$.6\lambda_d$.771	.76	3%
$.65\lambda_d$.755	.75	1%

Table 5.1 A comparison of the period of the slot tangential electric field with surface wave wavelength for various slab thicknesses ($\lambda_d = \lambda_0 \sqrt{\epsilon_d}$ where λ_0 is free space wavelength and $\epsilon_d = 2.7$)

modes which exist in a dielectric slab located in free space.

Some of the results for the $\ell = 1.0\lambda_0$ case (Fig. 5.6) are plotted and compared to those of a Two-Media slot problem [44]. By Two-Media slot problem it is meant that an infinite slot perforated ground screen separates half spaces of different, but homogeneous, electrical properties. If the slab thickness h is increased to infinity for the case of a dielectric slab covered slotted screen, then eventually the Two-Media case would be approached. Although it is possible that the slab would not have to be excessively thick in order to produce similar results for the two problems, it would be a difficult numerical problem to substantially increase the size of the slab since the number of surface wave modes increases in the slab in proportion to the thickness of the slab and thus the number of singularities in the Sommerfeld integral integrand increases. However, in the results shown in Fig. 5.6 there is a good indication that the two media case is being approached even though the slab thickness is $h = 1.23\lambda_d$ and only two surface waves exists for this thickness.

5.1b Convergence Tests

In order to establish numerical accuracy for the various results of this chapter several convergence tests were run. In each case an adequate number of pulses was taken in order to insure accuracy of the moment method solution. For example, for the case of TE excitation of a slot of width $\ell = 3.0\lambda_0$ and dielectric slab thickness $h = 3.0\lambda_d/8.0$, it was determined that 33 pulses were required for convergence to the fifth decimal place. By 'convergence' it is meant that the magnetic current

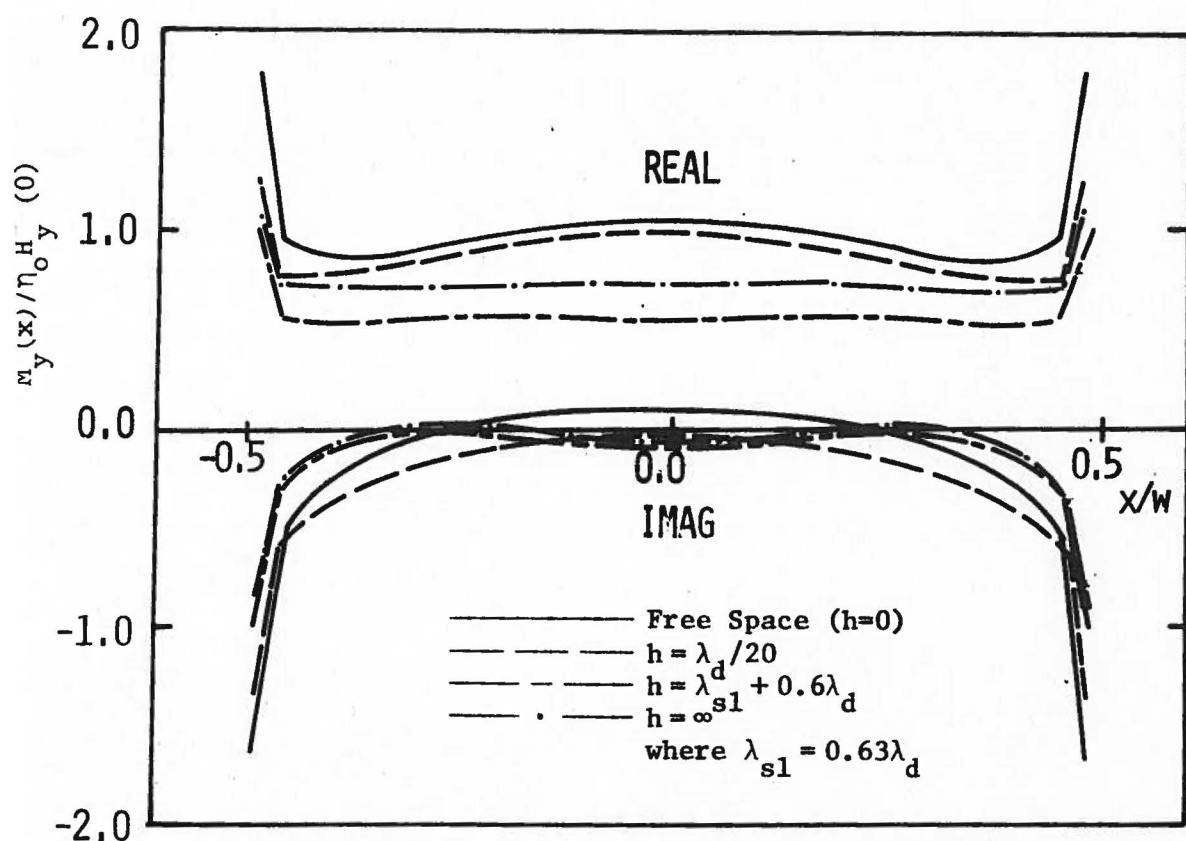


Fig. 5.6 Equivalent magnetic current $M_y(x)$ ($= E_x^a$) for a slot of width $1.0\lambda_o$, subject to normally incident TE excitation showing transition from the Free Space ($h=0$) case to the Two Media ($h=\infty$) case.

in the center of the slot does not change significantly with an increase in the number of basis set subdomains in the moment method solution.

5.1c Plausibility Test

To determine the general plausibility of the analytical (and numerical) solution a comparison test was run between the analytically derived electric field for plane wave incidence upon a dielectric slab of infinite extent lying in free space and the electric field obtained by numerical solution of the TE case integral equations at the center of a dielectric covered screen containing an electrically large slot. The slot width was chosen to be electrically large so that edge singularities would not effect the field at the center of the slot.

Fig. 5.7 shows a comparison between the analytically derived electric field at a dielectric slab-air interface for a dielectric slab of infinite extent and results taken for a dielectric-covered screen with a slot width $\ell = 3.0\lambda_0$. As is expected, the results show a close correlation between the two cases except near the thicknesses where a second surface wave is excited. Differences between the two curves may be accounted for by the action of standing waves mentioned previously in this section.

5.1d TE Case Far Fields

In the following presentation of the far fields a distinction is made between the space wave field and the surface wave field. The space wave is that portion of the slot field which has been radiated to the far field as opposed to the surface wave portion which is delivered to the far field via the guiding structure of the dielectric slab. The space wave predominates at large distances above the dielectric slab, whereas the

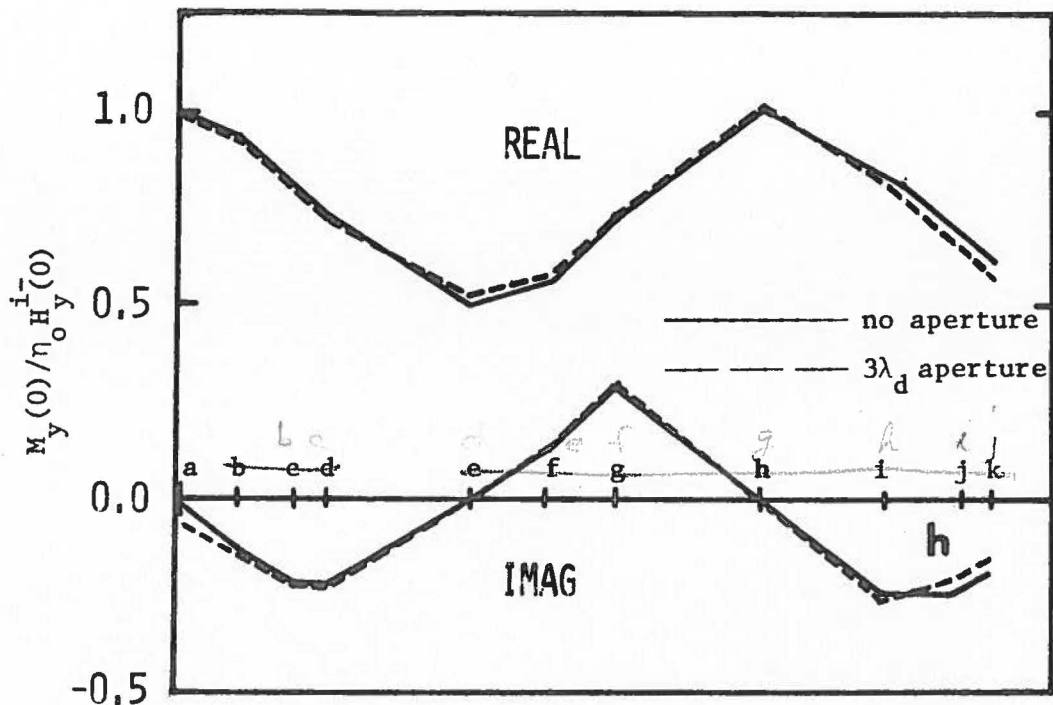


Fig. 5.7 Plausibility test showing center-of-slot equivalent magnetic current $M_y(0) = E_x^a$ for a slot of width $3.0\lambda_o$ subject to normally incident TE excitation as a function of slot thicknesses $h = [a(\lambda_d/50), b(\lambda_d/10), c(\lambda_d/8), d(\lambda_d/4), e(5\lambda_d/16), f(3\lambda_d/8), g(\lambda_d/2), h(.6\lambda_d), i(.63\lambda_d), j(\lambda_{sl} + \lambda_d/50), k(\lambda_{sl} + \lambda_d/20)]$, where $\lambda_{sl} = .63\lambda_d$.

surface wave is larger close to and on the interior of the slab.

The magnitude of the space wave portion of the far field H_y^0 component shown in Fig. 5.8 for the region $z > 0$ is calculated using the equivalent magnetic current distributions shown in Fig. 5.2. The far magnetic field space wave is normalized to the magnitude of the broadside ($\theta = 0^\circ$) magnetic field ($H_y^0(0)$) at the center of the slot when the dielectric slab thickness h is zero (Free Space case). The $\bar{E}(\theta)$ component of the far field can be easily calculated from the $H_y^0(\theta)$ component. The space wave portion of the far magnetic field shown in Fig. 5.2 is not valid past an angle of 88° (except for the Free Space case) because at this angle the field point intersects the dielectric slab at the radial distance chosen for these numerical results. Inside the dielectric slab the space wave portion of the far field is found by applying the field equations appropriate to the interior region.

Some insight into the mechanism by which surface waves are excited may be gained through a study of the far field radiation patterns. For a narrow slot (Fig. 5.8) the far field pattern is relatively omnidirectional as is expected when no slab exists over the slot. Since TE excitation of a slot will produce TM surface waves (no lower cut-off wavelength regardless of slab thickness), the introduction of a thin slab will still yield a relatively omni-direction pattern since a surface wave in a thin slab will not capture much of the energy transmitted through the slot. However as the slab thickness is increased the main lobe of the far field pattern appears in the broadside direction ($\theta = 0^\circ$). As one continues to increase the thickness of the slab, part of the main lobe breaks away into a

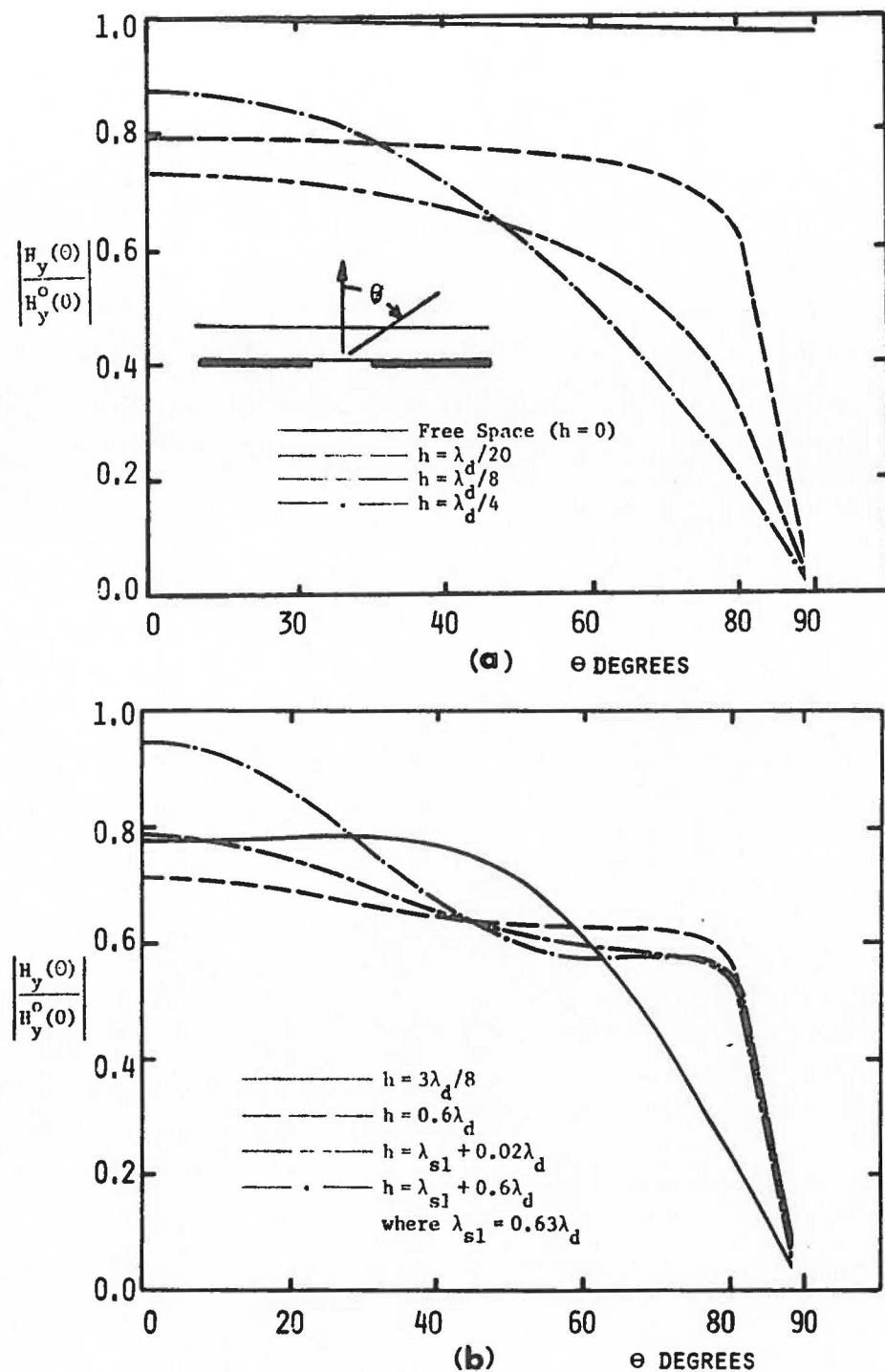


Fig. 5.8 Normalized space wave portion of the far magnetic field component $H_y(\theta)$ for a slot of width $0.1\lambda_0$, subject to normally incident TE excitation for various slab thicknesses.

secondary lobe (Fig. 5.8(b)) and moves toward the end-fire position ($\theta = 90^\circ$). The secondary lobe reaches the end-fire direction coincident with the production of a second surface wave ($h = \lambda_{s1}$). This process continues with increasing dielectric slab thickness. The onset of a third surface wave is shown in the figures for the case of a dielectric slab thickness $h = \lambda_{s1} + .6\lambda_d$.

For wider slots (Figs. 5.9, 5.10 and 5.11) the initial far field pattern tends to be concentrated in the broadside direction. Although one can still view the production of surface waves at the same dielectric slab thickness as they occur for the narrower $0.1\lambda_o$ slot, it is obvious that less of the total radiated power is taken up for the production of surface waves in the wider slot cases.

The space wave and surface wave components of the far magnetic field were calculated close to and in the region interior to the dielectric slab. It was found that interior to the slab the H_y space wave component always approached an amplitude of zero near the surface of the perfectly conducting screen. However, a null in the space wave at $\theta=90^\circ$ is typically observed only for certain slot widths when a conducting screen lies in a homogeneous medium. Although transferal of energy from the space wave to a surface wave mode does occur in the slab a more extensive explanation for the presence of the space wave null at $\theta=90^\circ$ must await further investigation.

The surface wave fields for the case of a $0.1\lambda_o$ slot are shown in Fig. 5.12. The vertical hash-marks on the various curves indicate the point of intersection of the observation point and the dielectric slab-air interface. It is evident in the figure that some energy is absorbed

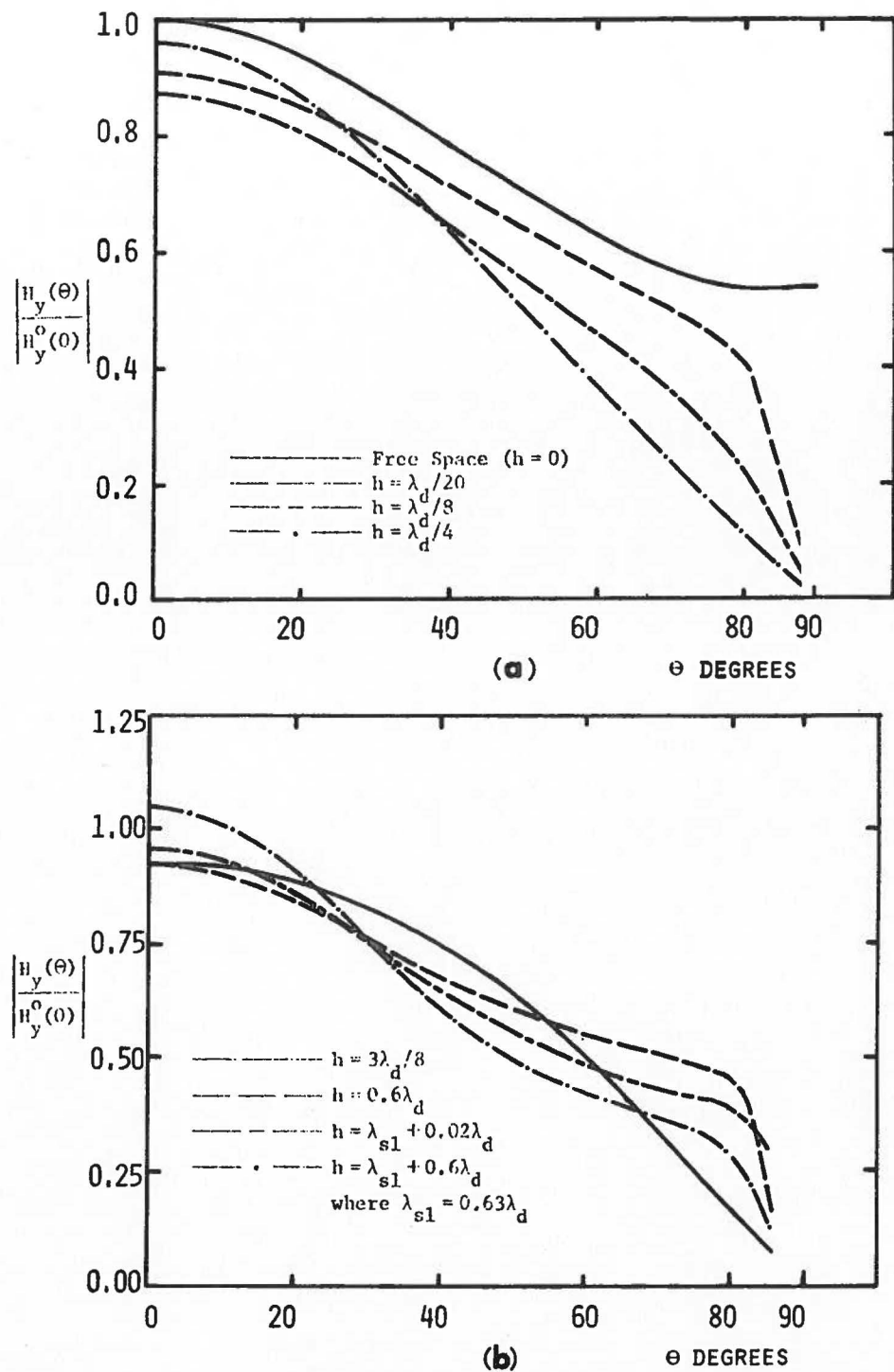


Fig. 5.9 Normalized space wave portion of the far magnetic field component $H_y(\theta)$ for a slot of width $0.5\lambda_o$, subject to normally incident TE excitation for various slab thicknesses.

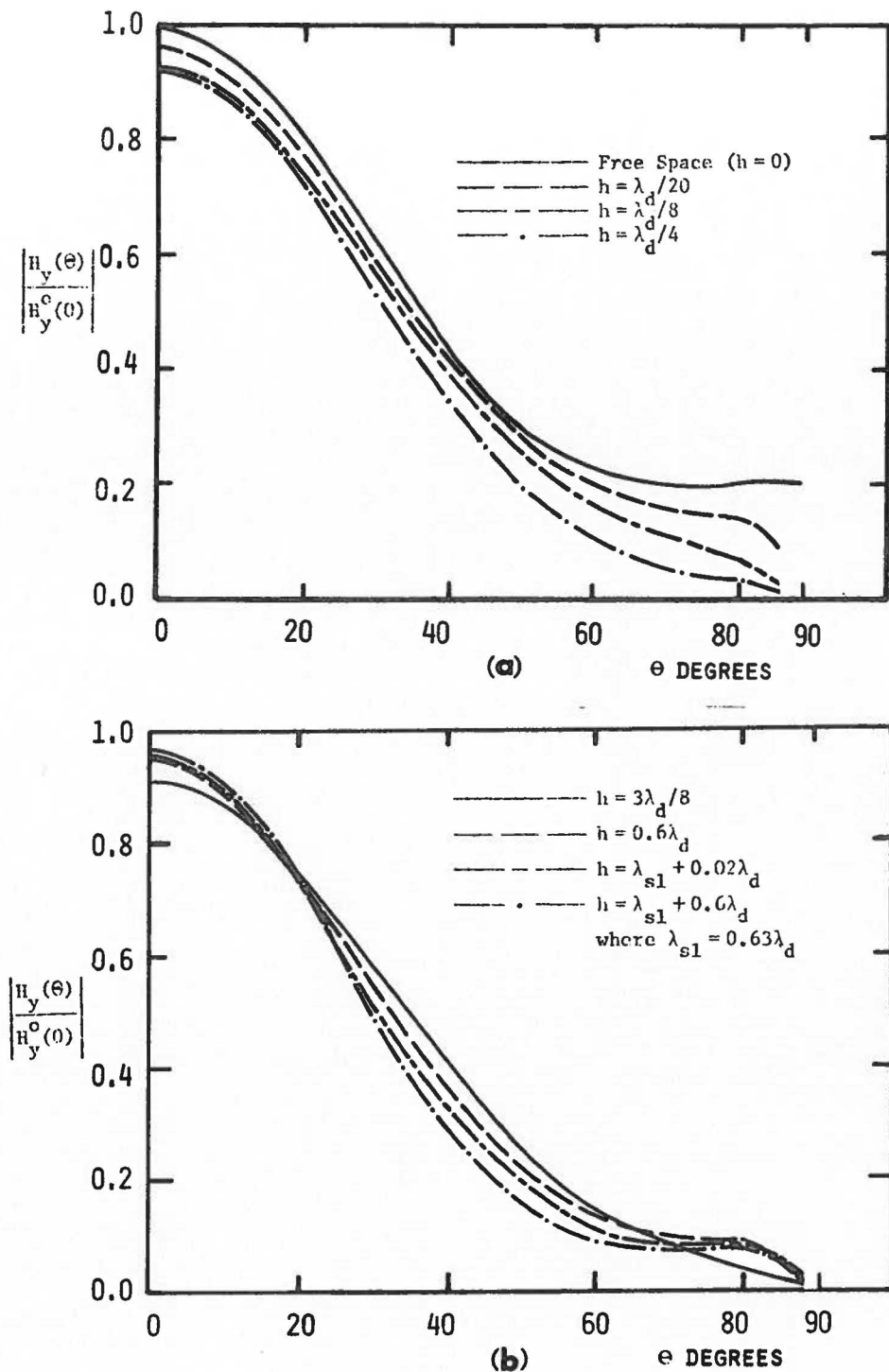


Fig. 5.10 Normalized space wave portion of the far magnetif field component $H_y(\theta)$ for a slot of width $1.0\lambda_o$, subject to normally incident TE excitation for various slab thicknesses.

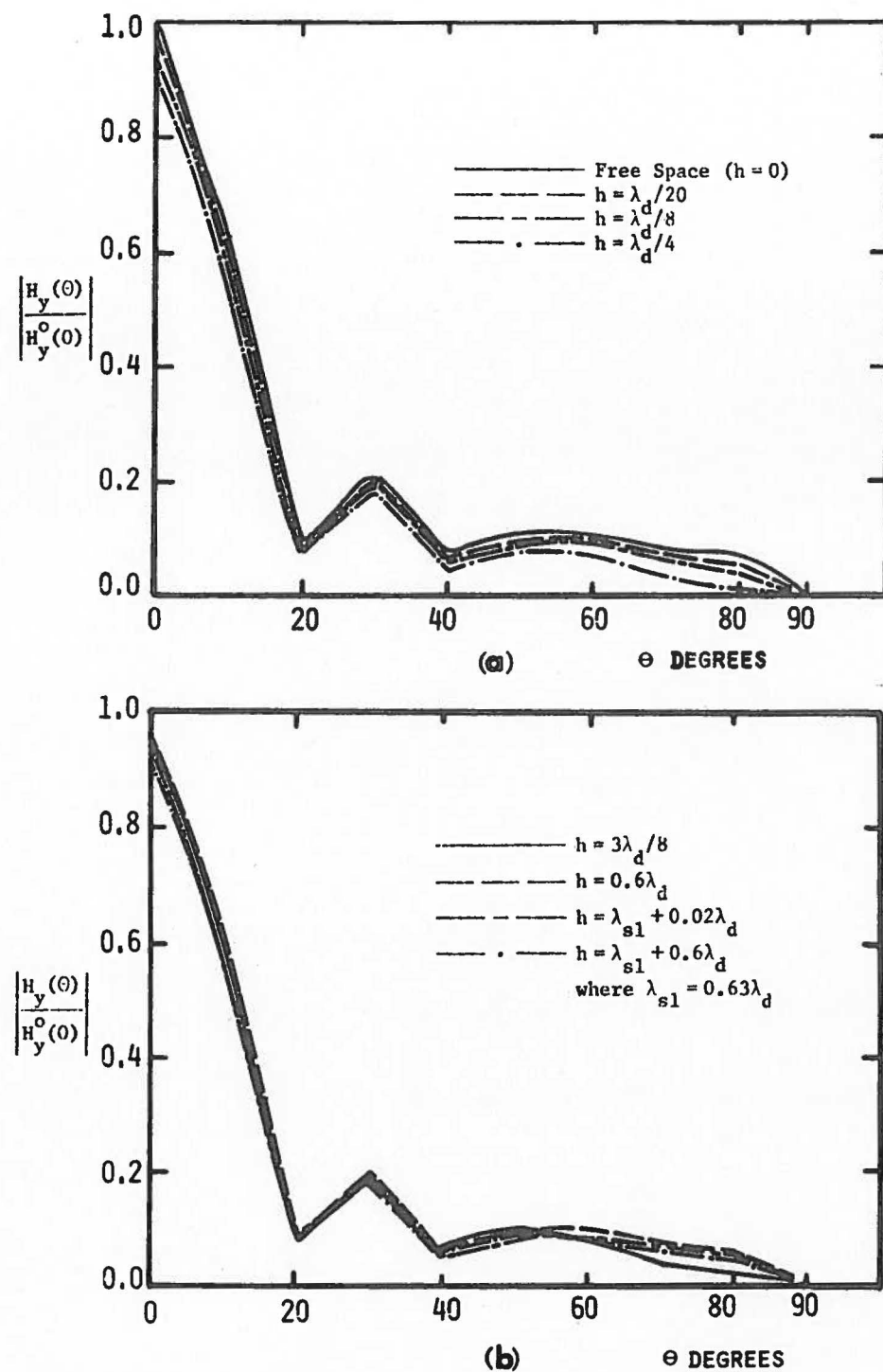


Fig. 5.11 Normalized space wave portion of the far magnetic field component $H_y(\theta)$ for a slot of width $3.0\lambda_o$, subject to normally incident TE excitation for various slab thicknesses.

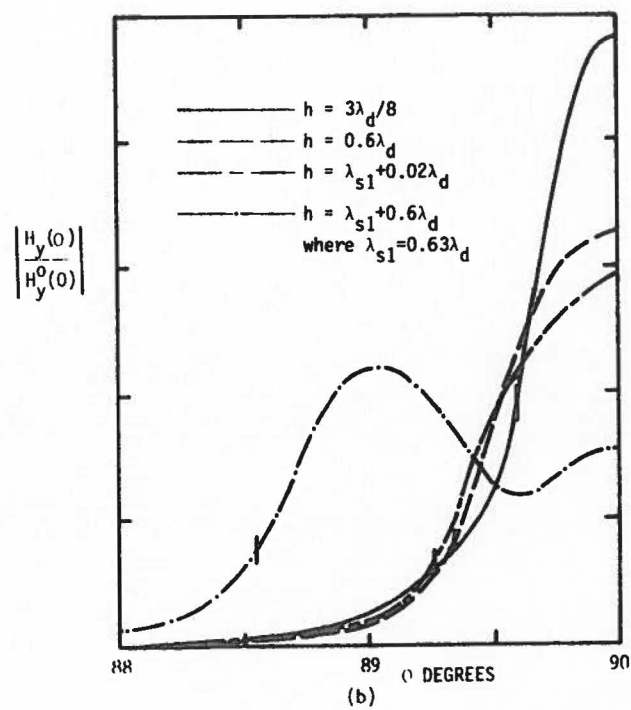
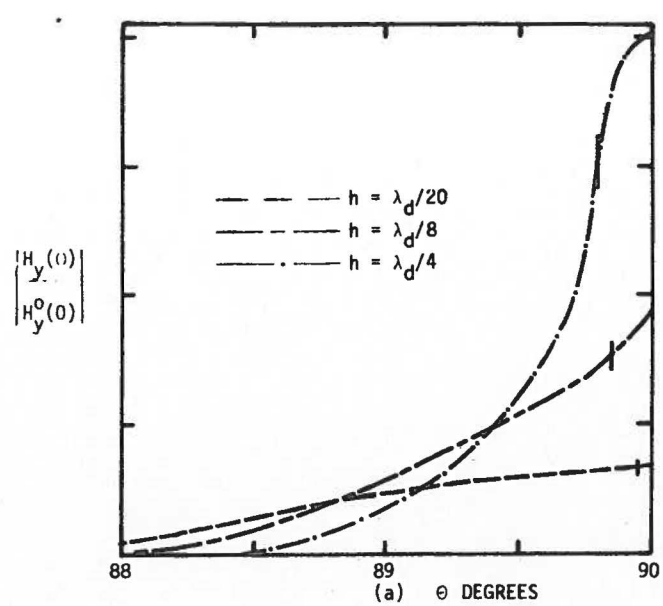


Fig. 5.12 Normalized surface wave portion of the far magnetic field $H_y(\theta)$ for a slot of width $0.1\lambda_0$, subject to normally incident TE excitation for various slab thicknesses.

in the surface wave even in very thin slabs. As the slab thickness is increased the amplitude of the H_y component of the magnetic field increases. As the thickness of the slab is further increased the maximum amplitude of the tangential magnetic field component decreases, however the total energy coupled into the surface wave continues to increase.

5.1e TE Case as a Function of Angle of Incidence

Fig. 5.13 shows the equivalent magnetic current in a slot which is excited by a TE plane wave at a variety of angles of incidence. Fig. 5.14 pictures the far field H_y magnitude as a function of angle. As expected the total transmitted power decreases as the angle of incidence approaches 90 degrees. Although the thickness of the dielectric remains constant at $h = \lambda_d / 8$ the power transmitted into the surface wave tends to decrease as the angle of incidence of the plane wave excitation approaches 90°. No new surface waves are produced when the angle of incidence of the excitation field is varied.

5.2 TM Excitation of a Slot in a Ground Screen Covered by a Dielectric Slab

5.2a TM Slot Magnetic Current Distribution

Fig. 5.15 displays the numerical results obtained as a function of dielectric thickness for the case of TM excitation of a slot in the dielectric slab covered screen pictured in Fig. 5.1. For the results shown in this figure the selection of dielectric slab thickness is different from those chosen in the case of TE illumination presented in the previous sections. This is done since TE surface waves, which are excited by TM slot illumination, occur at different wave number values from those of

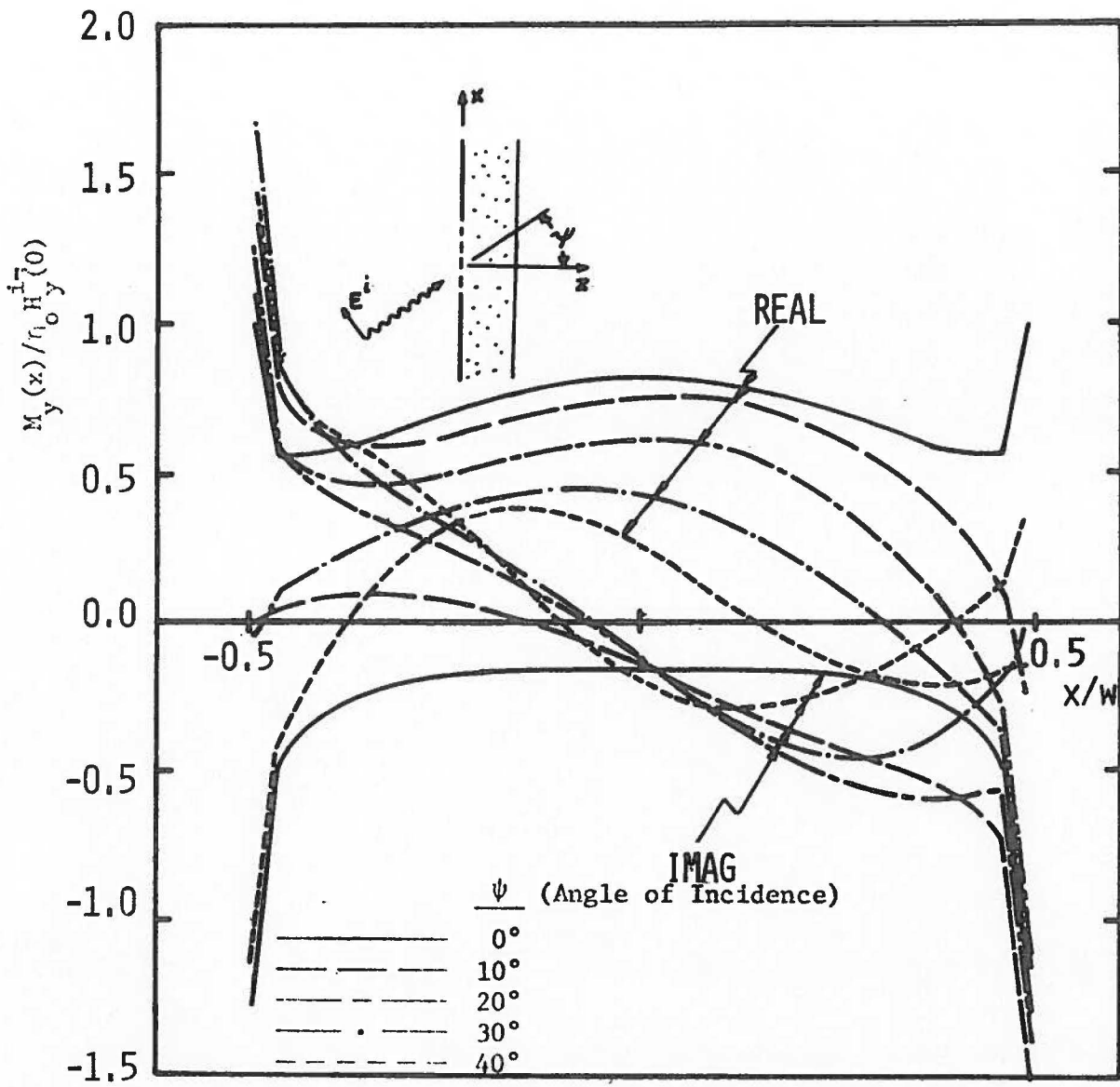


Fig. 5.13a Equivalent magnetic current $M_y(x)$ ($= E_x^a$) for a slot of width $1.0\lambda_0$ and dielectric slab thickness $h = \lambda_d/8$, subject to TE excitation at a variety of angles of incidence.

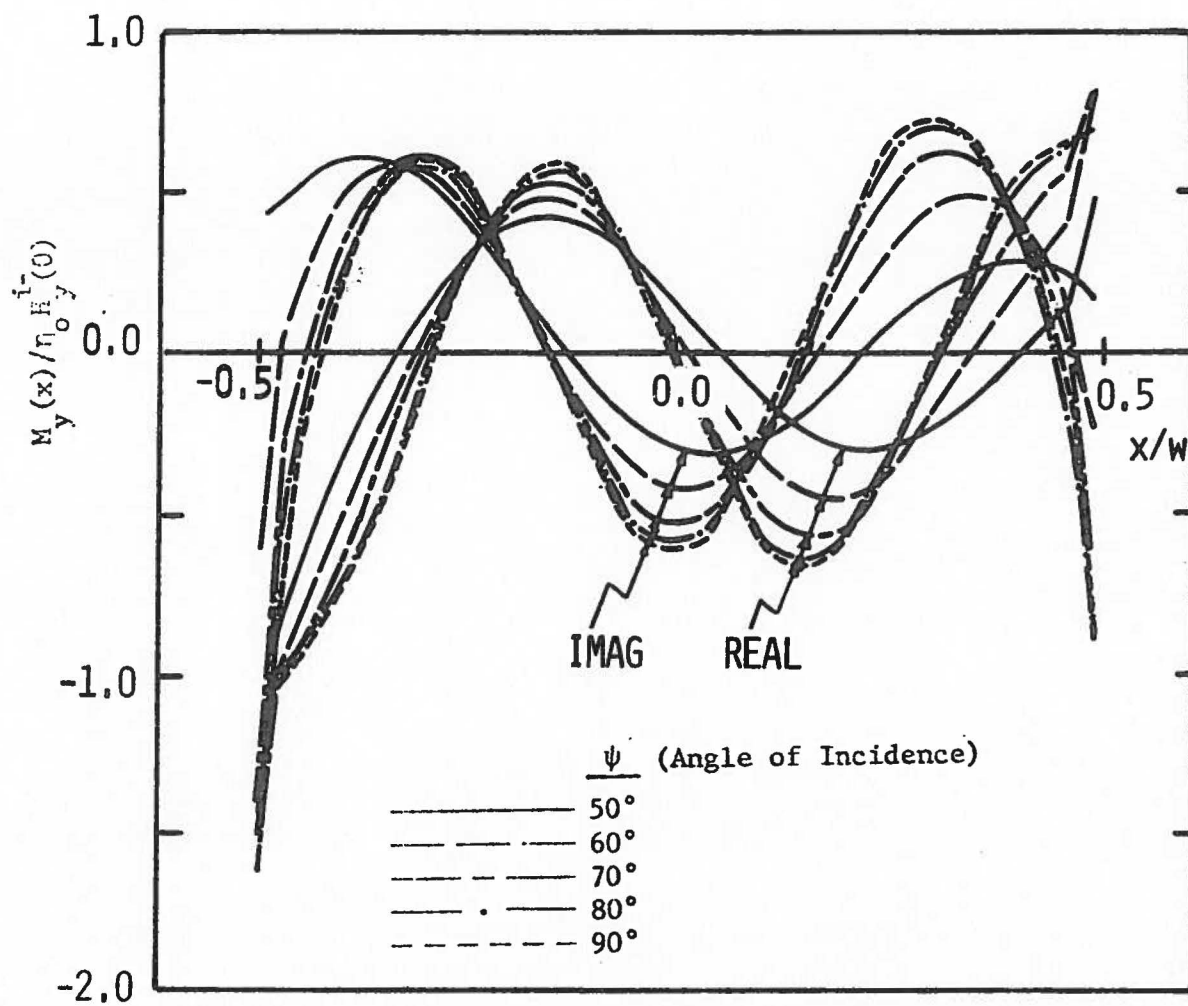


Fig. 5.13b Equivalent magnetic current $M_y(x) (= E_x^a)$ for a slot of width $1.0\lambda_0$ and dielectric slab thickness $h = \lambda_d/8$, subject to TE excitation at a variety of angles of incidence.

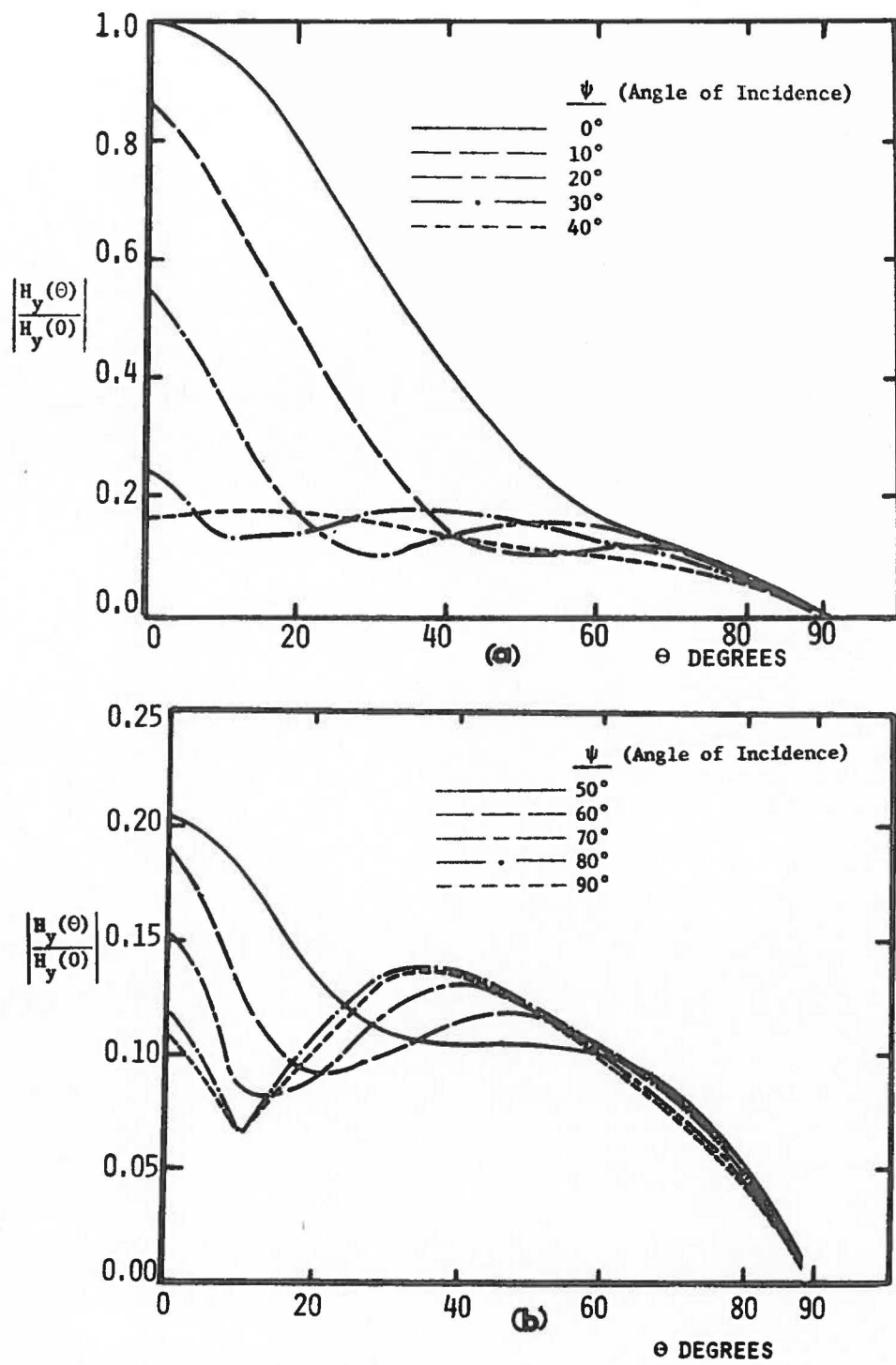


Fig. 5.14 Normalized space wave portion of the far magnetic field $H_y(\theta)$ for a slot of width $1.0\lambda_0$ and dielectric slab thickness $h = \lambda_d/8$, subject to TE excitation at a variety of angles of incidence.

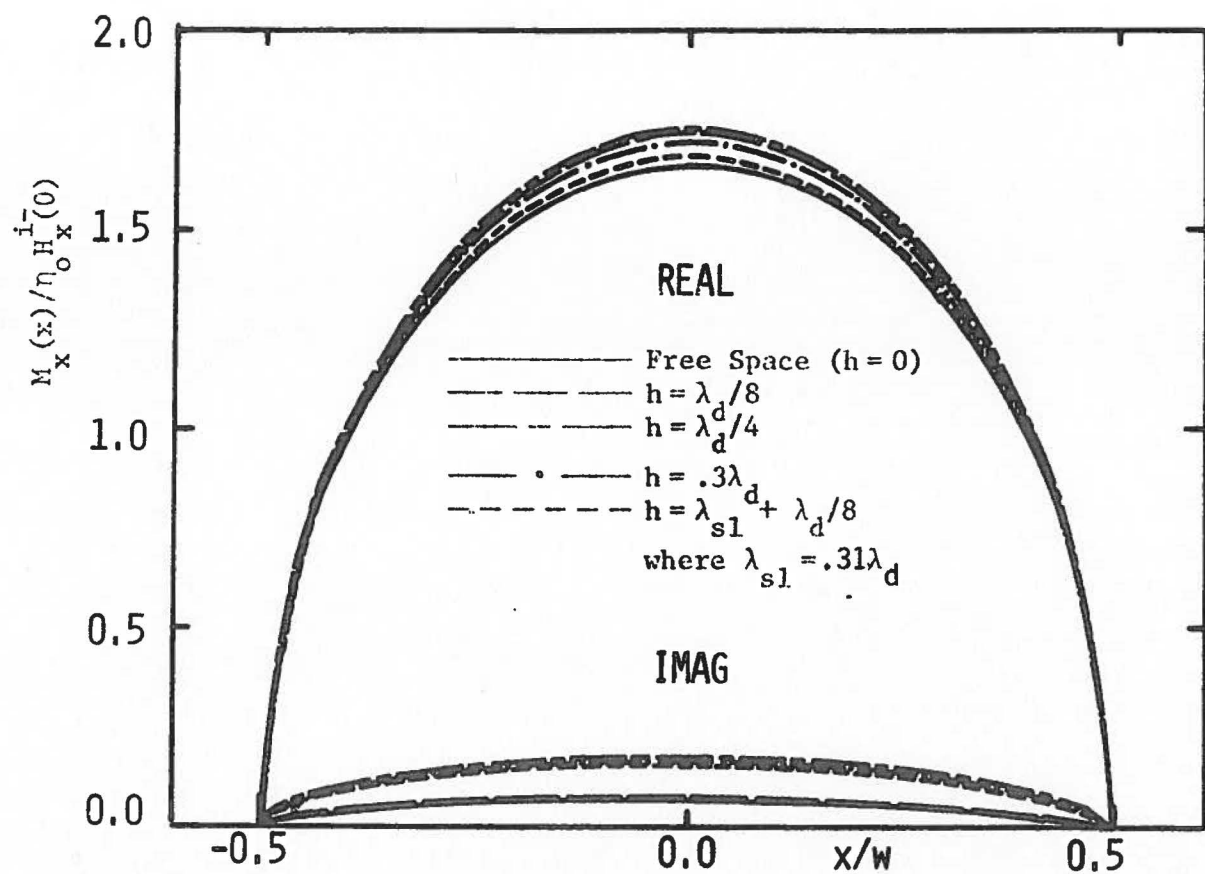


Fig. 5.15 Equivalent magnetic current $M_x(x) (= E_y^a)$ for a slot of width $0.1\lambda_0$, subject to normally incident TM excitation for various slab thicknesses.

TM surface wave for the same slab thickness. The magnetic current distribution is, in this case, normalized by the product of the magnetic field $H_x^1(0)$ incident upon the center of the slot and the free space wave impedance η . Figs. 5.16 and 5.17 show results for TM excitation of slots much wider than that shown in Fig. 5.15.

It is apparent in Figs. 5.15, 5.16 and 5.17 that as the slab thickness approaches zero the real and imaginary parts of the magnetic current approaches respectively the real and imaginary parts of the magnetic current for the Free Space ($h = 0$) case. Fig. 5.18 is a plot of the magnetic current for the Two Media problem ($h = \infty$) along with curves for several other thicknesses for a slot width of $\lambda_0/2$. In Fig. 5.18 it is observed that the magnetic current for cases of a dielectric slab of thickness larger than that at which a single surface wave is excited approaches the magnetic current of the Two Media case. Only one TE surface wave mode exists in the dielectric slab when the slab has a thickness of $\lambda_{sl} + \lambda_d/8$, where $\lambda_{sl} = .3\lambda_d$ is the wave number for which the first TE surface wave mode occurs.

5.2b TM Case Far Fields

The magnitude of the space wave portion far field E_y component for the region $z > 0$ is calculated using the magnetic current distributions in Fig. 5.15 and is shown in Fig. 5.19. The far field component of the magnetic field can be readily found from the far field E_y component. The space wave portion far electric field shown is not valid for angles greater than 88° (except for the Free Space case) since for the observation radius chosen the field point lies inside the dielectric slab.

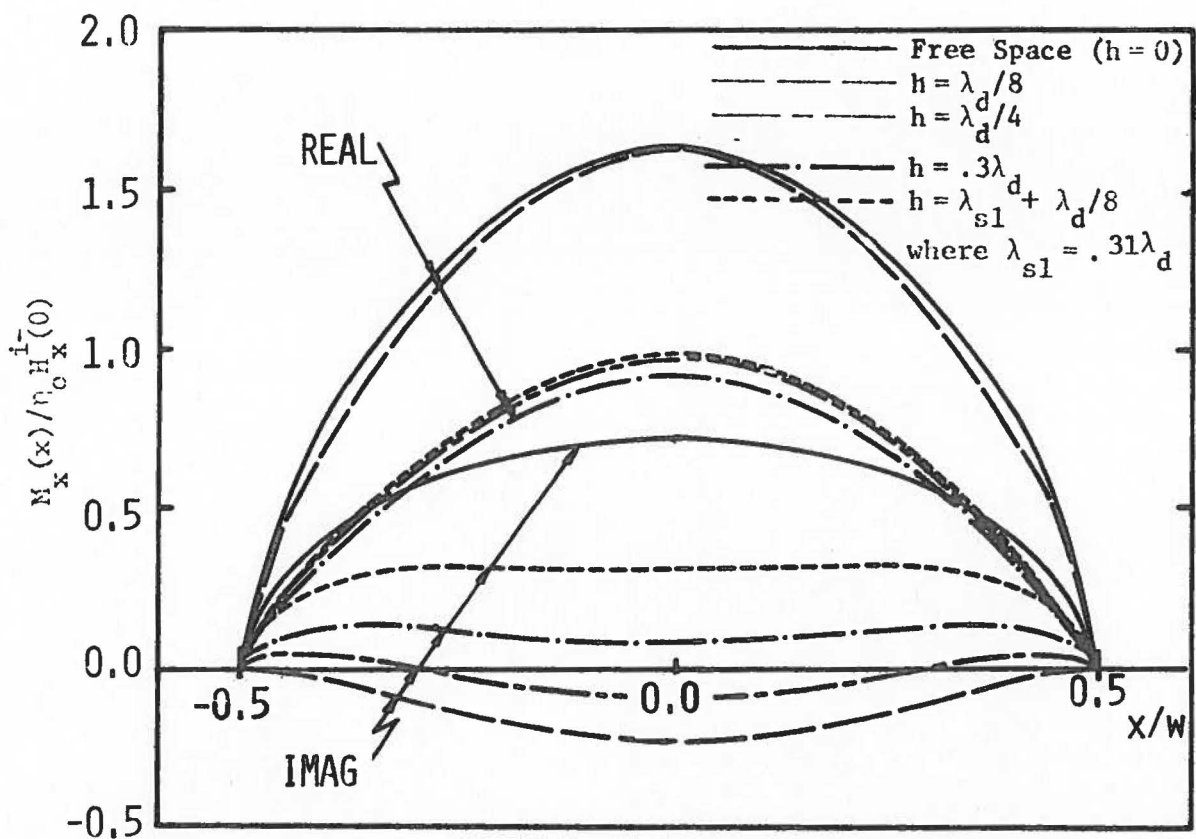


Fig. 5.16 Equivalent magnetic current $M_x(x) (= E_y^a)$ for a slot of width $0.5\lambda_0$, subject to normally incident TM excitation for various slab thicknesses.

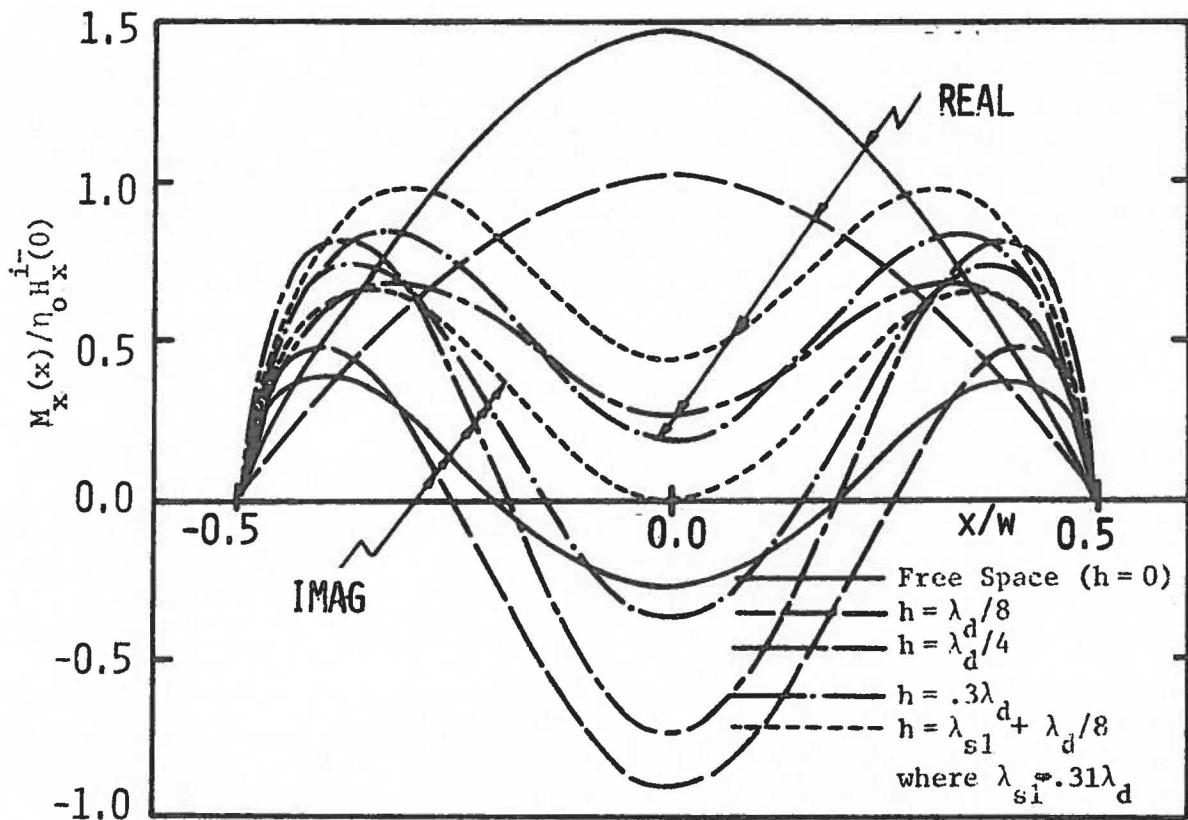


Fig. 5.17 Equivalent magnetic current $M_x (= E_y^a)$ for a slot of width $1.0\lambda_o$, subject to normally incident TM excitation for various slab thicknesses.

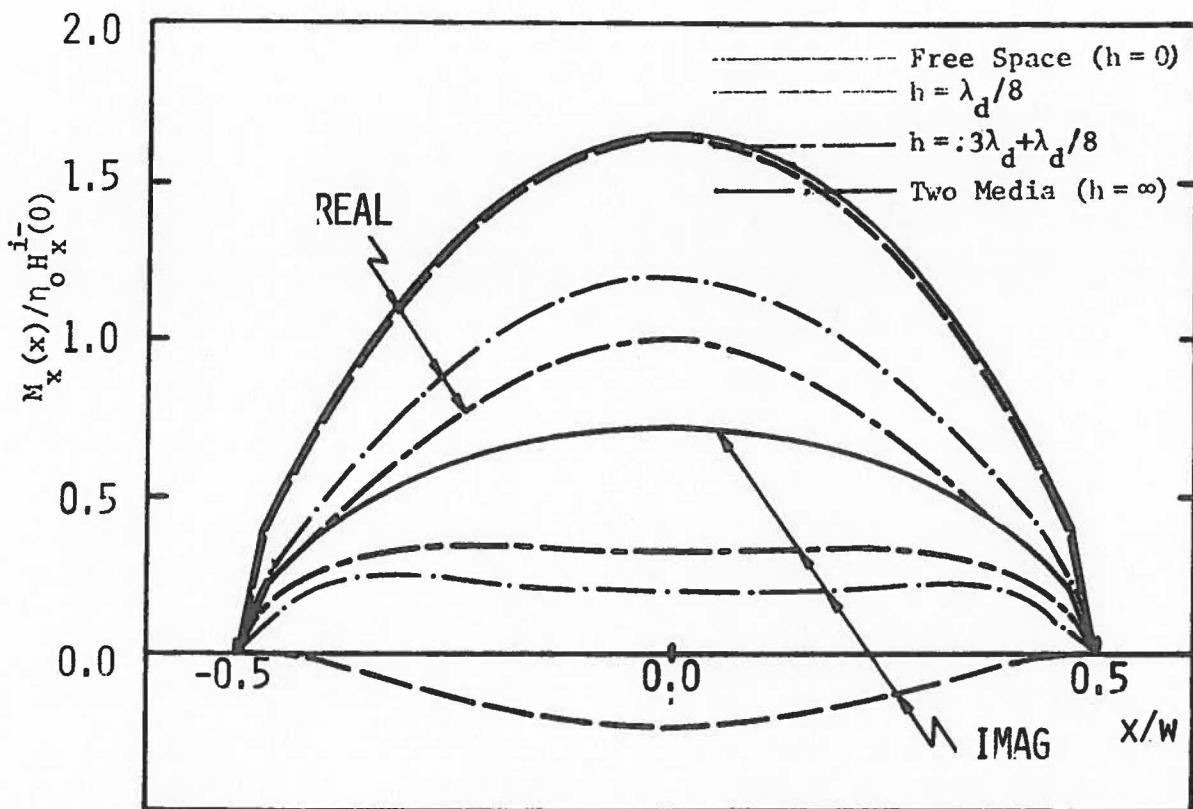


Fig. 5.18 Equivalent magnetic current $M_x(x)/\eta_0 H_x^i(0)$ for a slot of width $0.5\lambda_0$, subject to normally incident TM excitation for selected slab thicknesses.

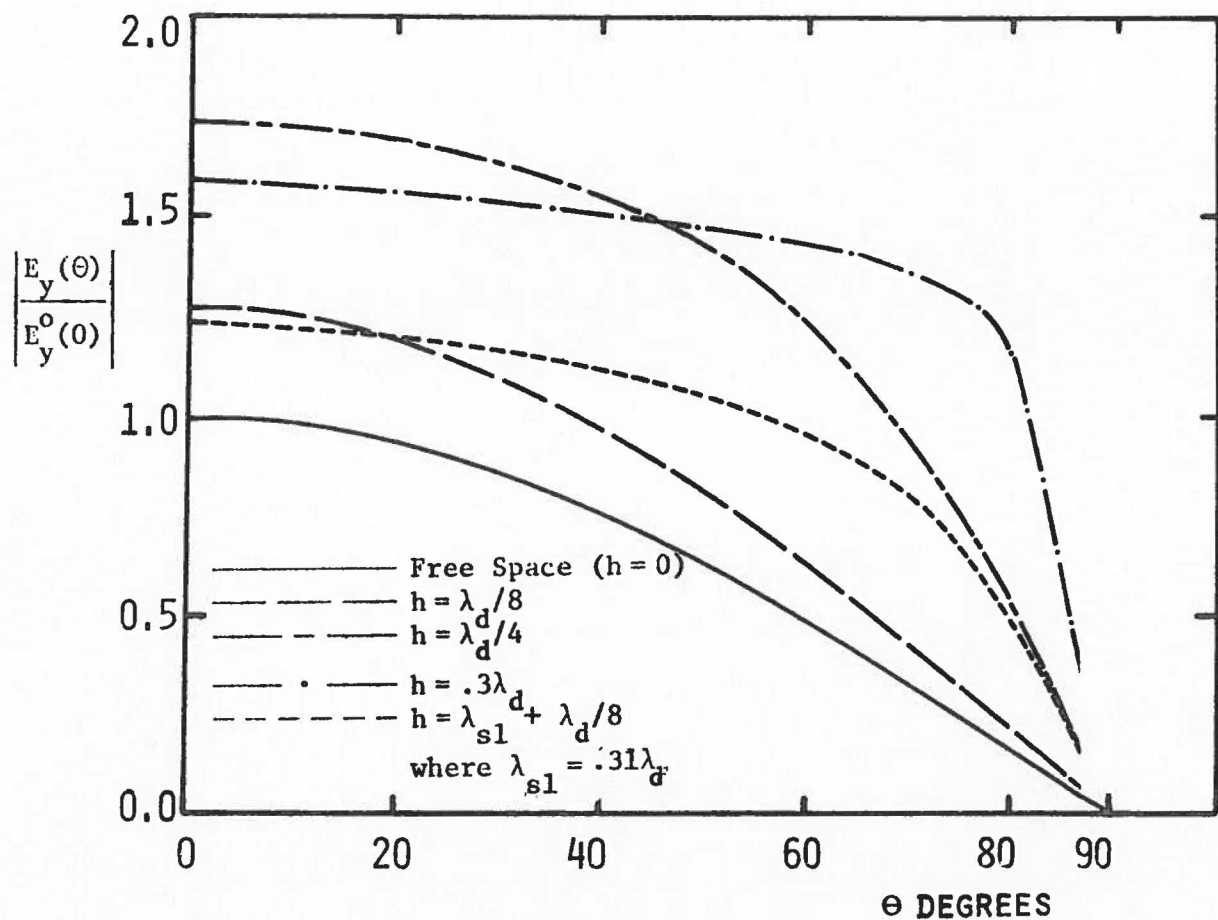


Fig. 5.19 Normalized space wave portion of the far electric field component $E_y(\theta)$ for a slot of width $0.1\lambda_0$, subject to normally incident TM excitation at various slab thicknesses.

Inside the dielectric slab the space wave portion of the far field is found by applying the field equations appropriate to the interior region.

As mentioned above, TE surface waves, unlike TM surface waves, have a cut-off frequency. The cut-off frequency is related to the dielectric slab thickness. For the case of a relative dielectric constant of $\tilde{\epsilon}_d = 2.7$ the smallest dielectric thickness which will support surface waves is $h = 0.31\lambda_d$. It is observed in Fig. 5.19 that as the thickness of the slab is increased the space wave electric field pattern becomes skewed toward the end-fire ($\theta = 90^\circ$) position. As the thickness of the slab is increased to sizes greater than that for which the first surface wave is launched the maximum of the electric field pattern once again becomes more pronounced in the broadside ($\theta = 0^\circ$) direction. This skewing of the main lobe phenomena also occurs in the wider slots (see Figs. 5.20 and 5.21). In the case of a one wavelength slot (Fig. 5.21) a minor lobe tends to occur at thickness prior to that which will support a surface wave mode. At thicknesses slightly greater than that which will support a surface wave mode the minor lobe appears to have collapsed, supporting the contention that energy from the space wave has been transferred to the surface wave. Fig. 5.22 shows the form of a typical surface wave for the case of TM illumination of the slot.

5.3 TE Excitation of Two Slots in a Ground Screen Covered by a Dielectric Slab

We consider here a dielectric-slab-covered thin conducting plate of infinite extent, perforated by two parallel slots of infinite length and specified width. As in the single slot cases discussed in previous sec-

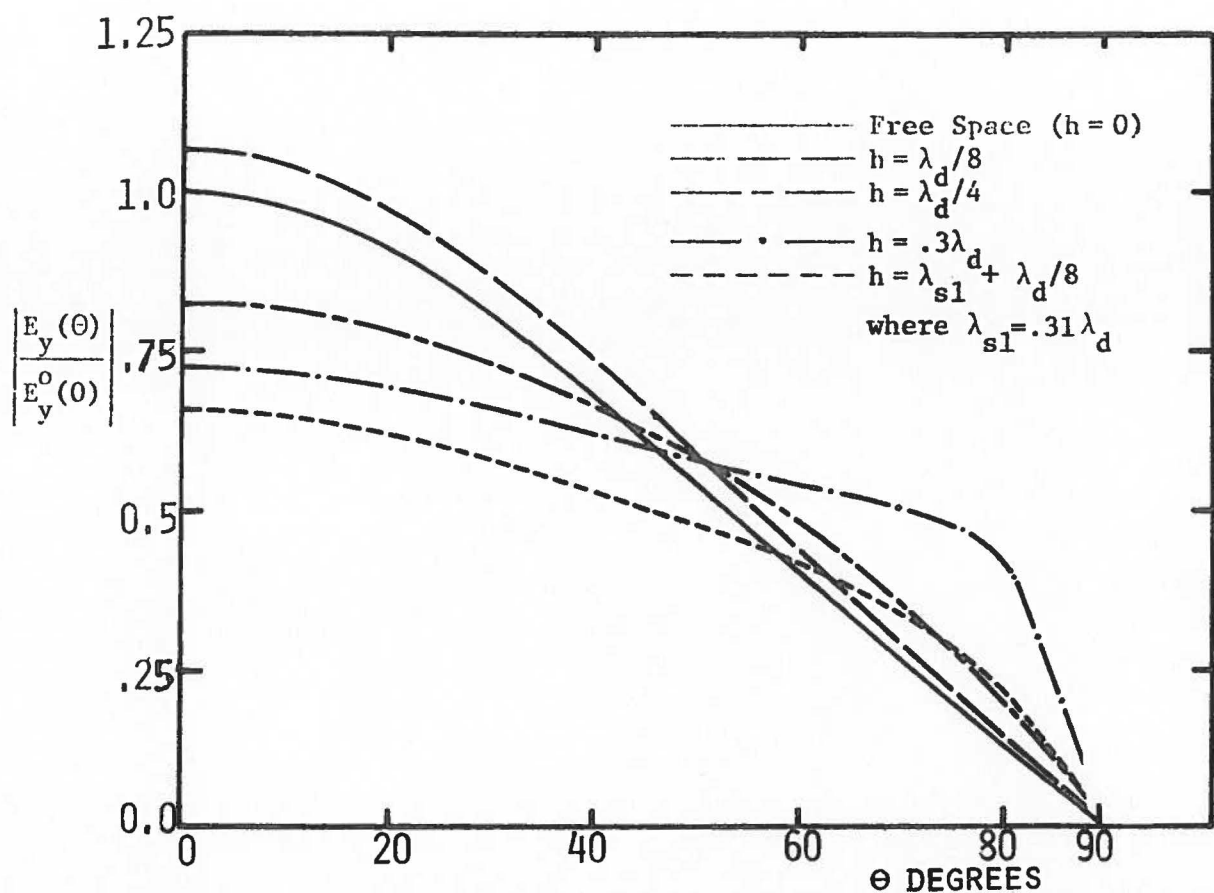


Fig. 5.20 Normalized space wave portion of the far electric field component $E_y(\theta)$ for a slot of width $0.5\lambda_0$, subject to normally incident TM excitation at various slab thicknesses.

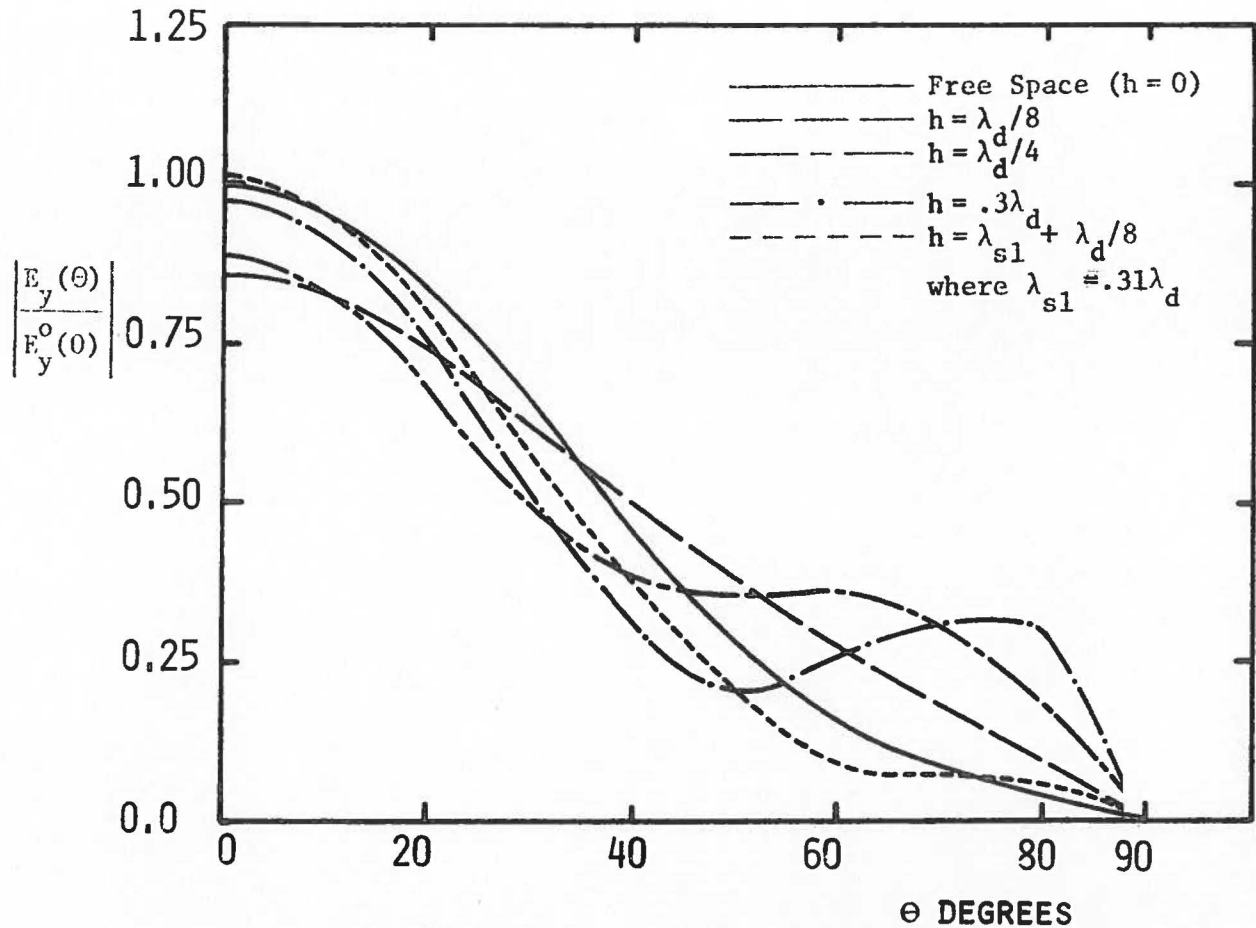


Fig. 5.21 Normalized space wave portion of the far electric field component $E_y(\theta)$ for a slot of width $1.0\lambda_o$, subject to normally incident TM excitation at various slab thicknesses.

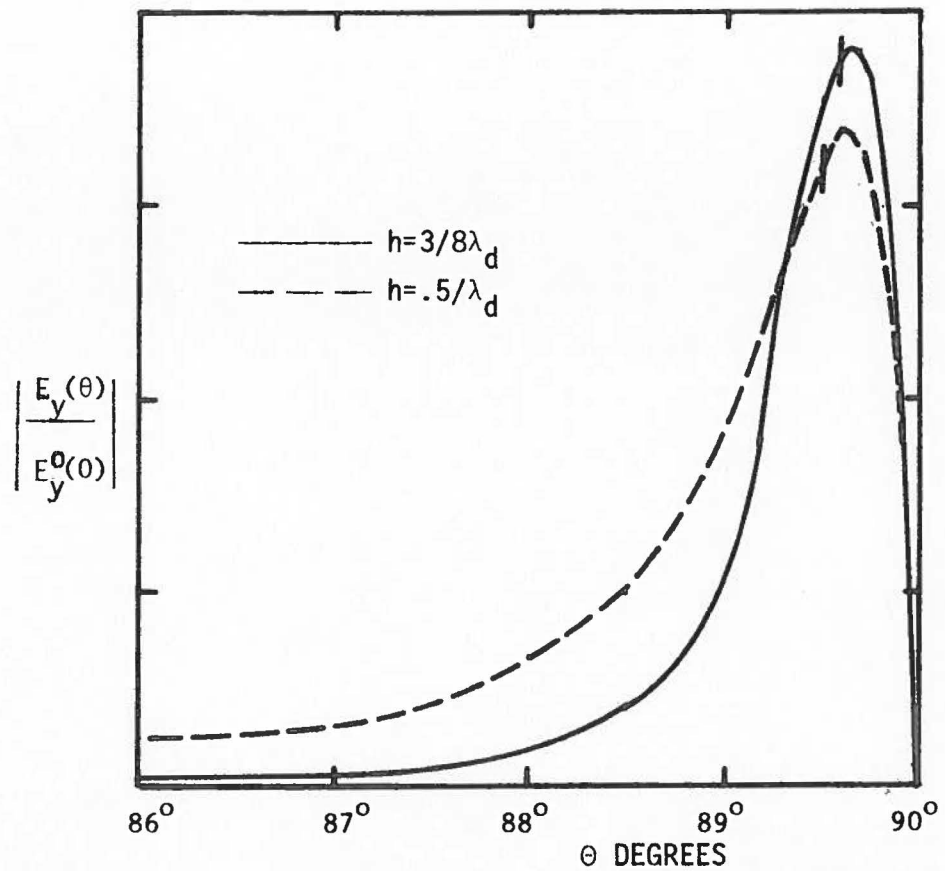


Fig. 5.22 Normalized surface wave portion of the far electric field component $E_y(\theta)$ for a slot of width $0.1\lambda_0$, subject to normally incident TM excitation at various slab thicknesses.

tions of this chapter, a dielectric slab lies only on the shadow side of the screen.

Fig. 5.23 shows the normalized magnetic current distribution in both slots as a function of dielectric slab thickness. The separation distances between the two slots measured from the centers of the slots in Fig. 5.23 is $s = .125\lambda_0$ and each slot has a different width. Coupling between the two slots is indicated by the fact that the magnetic slot current is assymetrical about the center of each slot even though excitation is due to a normally incident plane wave. Since all future figures for the case of two slots are of equal width and therefore produce magnetic current distributions which are an even function about the origin, only the $x > 0$ slot will be pictured. Fig. 5.24 shows the equivalent slot-magnetic-current as a function of dielectric slab thickness when the two slots are of equal width and separated by a distance $s = 0.5\lambda_d$. The corresponding normalized far magnetic field is shown in Fig. 5.25.

Fig. 5.26 pictures the equivalent slot-magnetic-current as a function of spacing s between the two slot axises for the Free Space ($h = 0$) case. For the same slot spacings s , Fig. 5.27 shows the equivalent slot-magnetic-current when a dielectric slab of thickness $h = \lambda_d/8$ lies over the ground screen. Significant differences are seen in the plotted results.

Fig. 5.28 shows the equivalent slot-magnetic-current for a large separation distance s between the slot axises when a dielectric slab of width $\lambda_d/8$ lies over the screen. Regardless of slot separation distance for the two slot case, significant distortion due to the surface

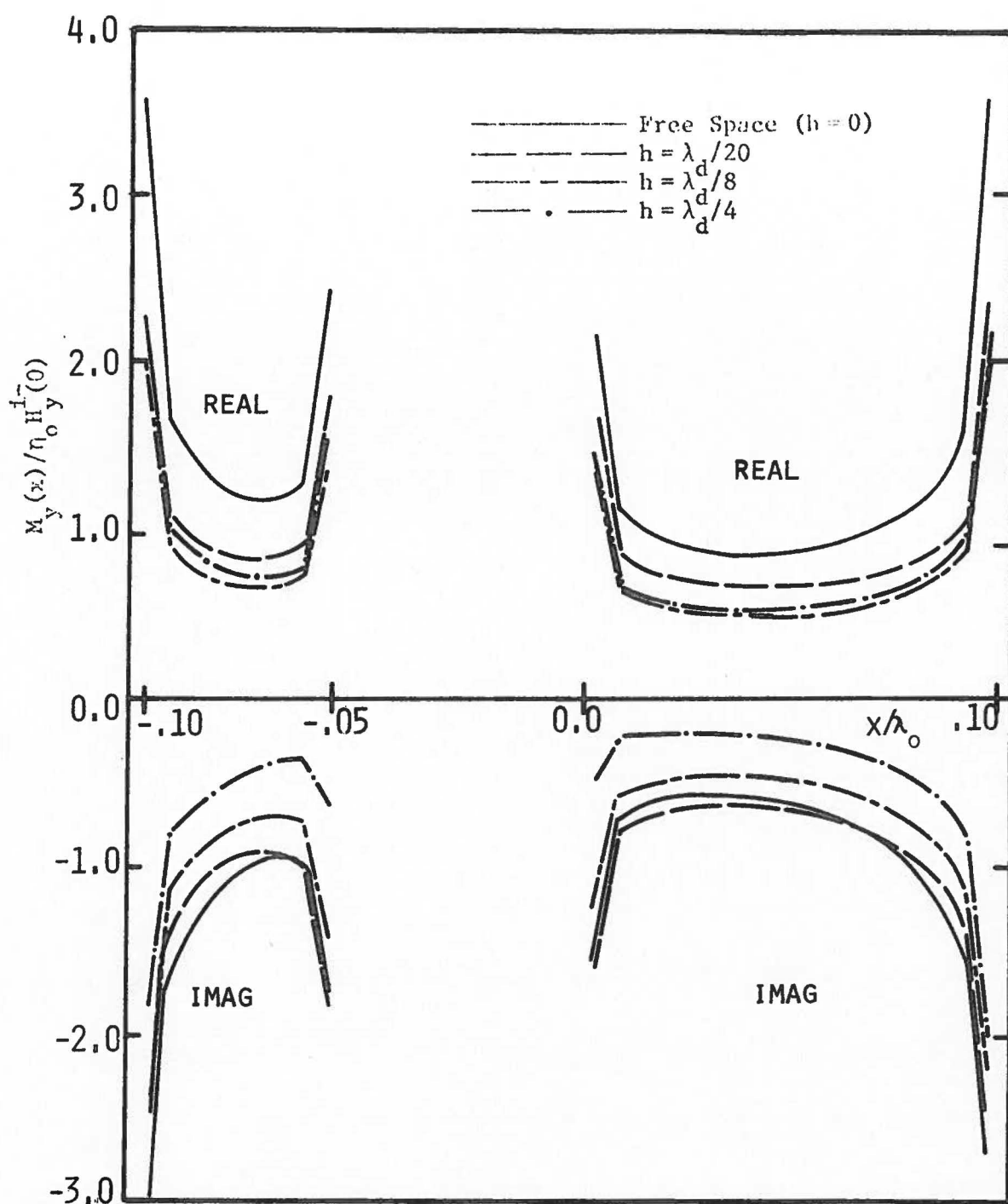


Fig. 5.23a Equivalent magnetic current $M_y (=E_x^a)$ for two slots of width $0.1\lambda_0$ and $0.5\lambda_0$, subject to normally incident TE excitation for various slab thicknesses.

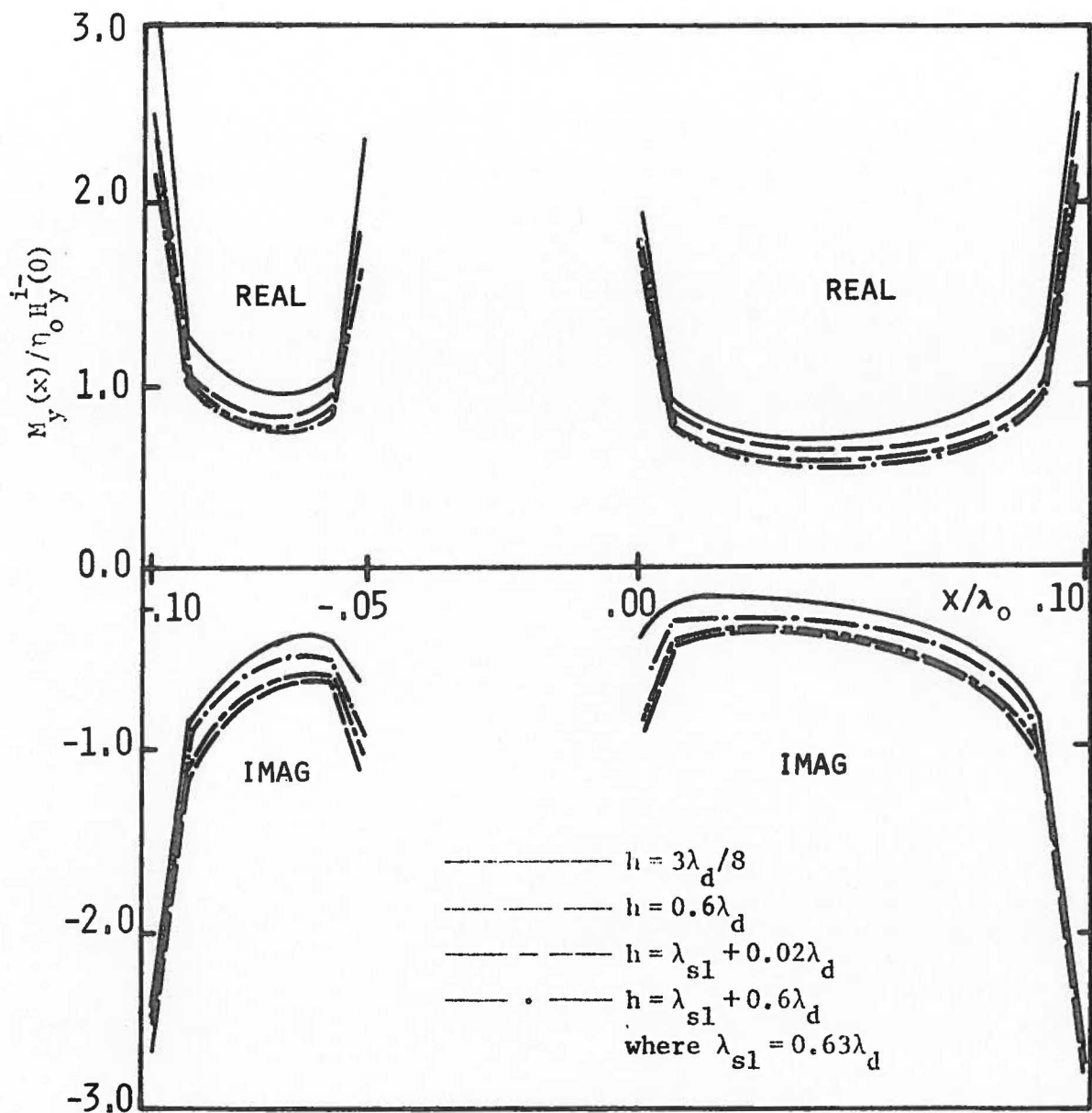


Fig. 5.23b Equivalent magnetic current $M_y(x)/\eta_0 H_y(0)$ for two slots of width $0.1\lambda_0$ and $0.05\lambda_0$, subject to normally incident TE excitation for various slab thicknesses.

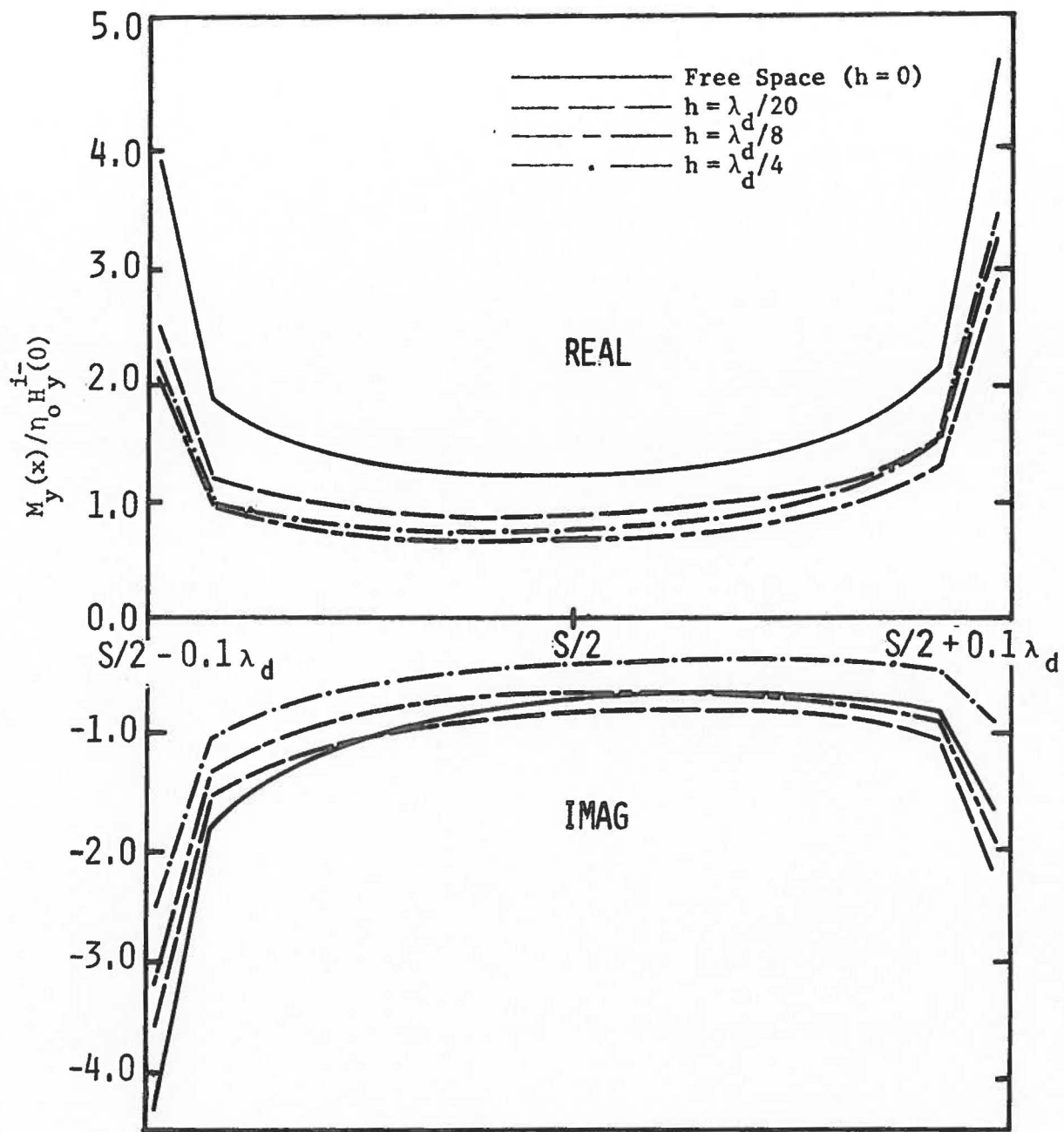


Fig. 5.24a Equivalent magnetic current $M_y (= E_x^a)$ for two slots of width $0.1\lambda_o$, subject to normally incident TE excitation for various slab thicknesses, $s = 0.5\lambda_d$ center-of-slot separation distance.

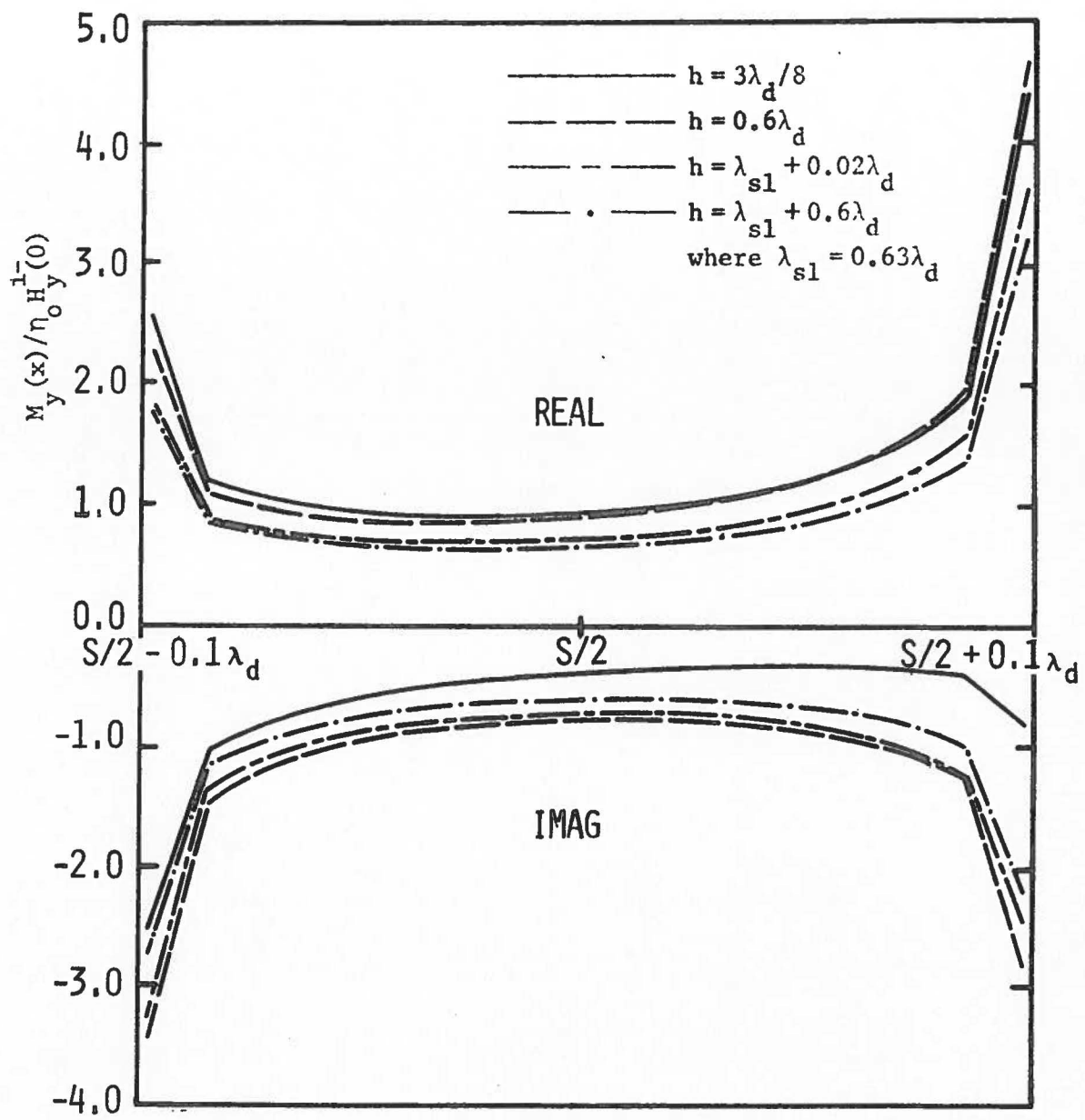


Fig. 5.24b Equivalent magnetic current $M_y(x) (= E_x^a)$ for two slots of width $0.1\lambda_o$, subject to normally incident TE excitation for various slab thicknesses, $s = 0.5\lambda_d$ center-of-slot separation distance.

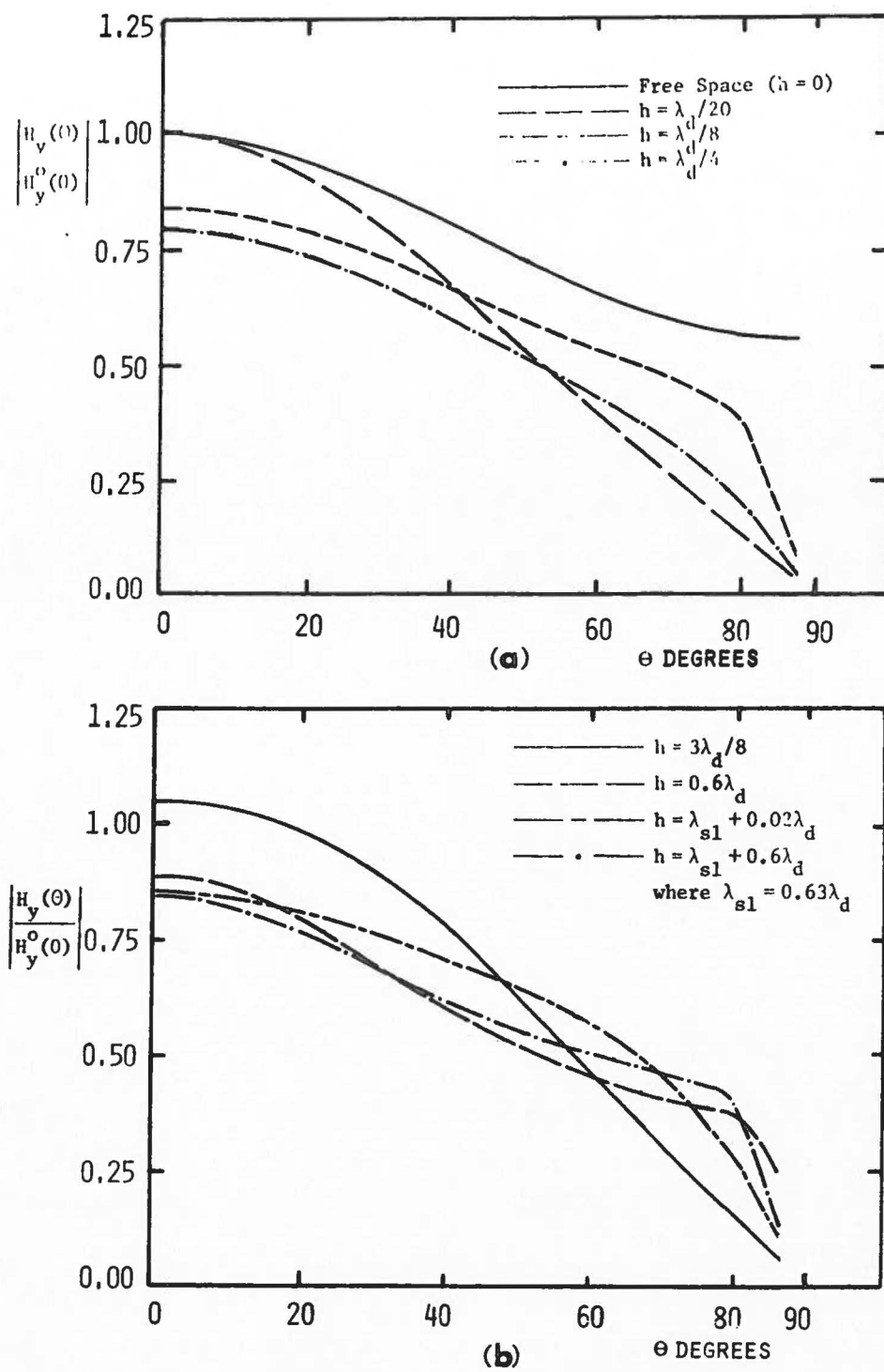


Fig. 5.25 Normalized far magnetic field $H_y(\theta)$ for two slots of width $0.1\lambda_o$ and separation distance $s = 0.5\lambda_d$ subject to TE excitation for various slab thicknesses.

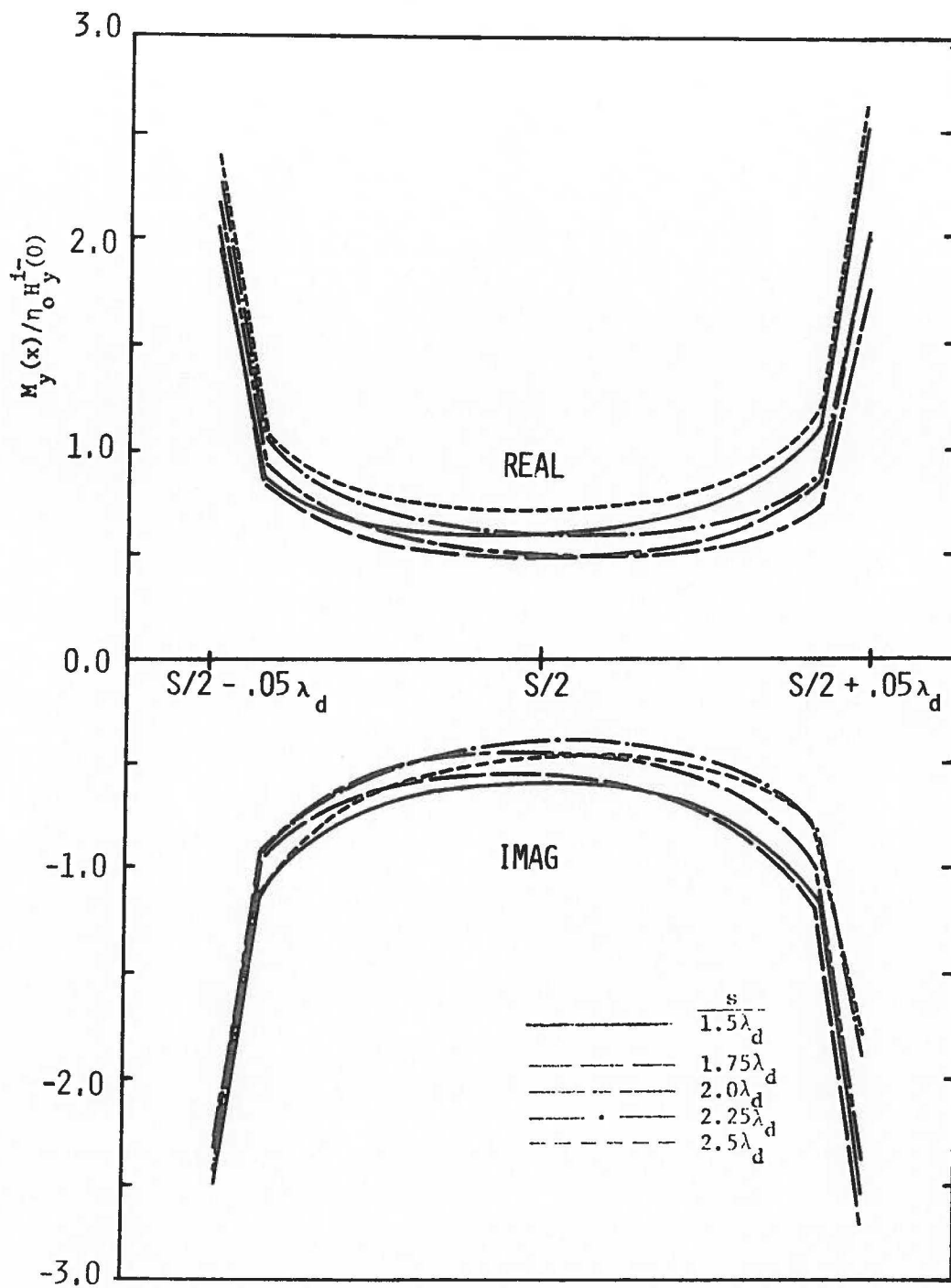


Fig. 5.26 Equivalent magnetic current $M_y (= E_x^a)$ for two slots of width $0.1\lambda_0$ and various slot separation distances s , subject to normally incident TE excitation with dielectric slab thickness $h = 0$.

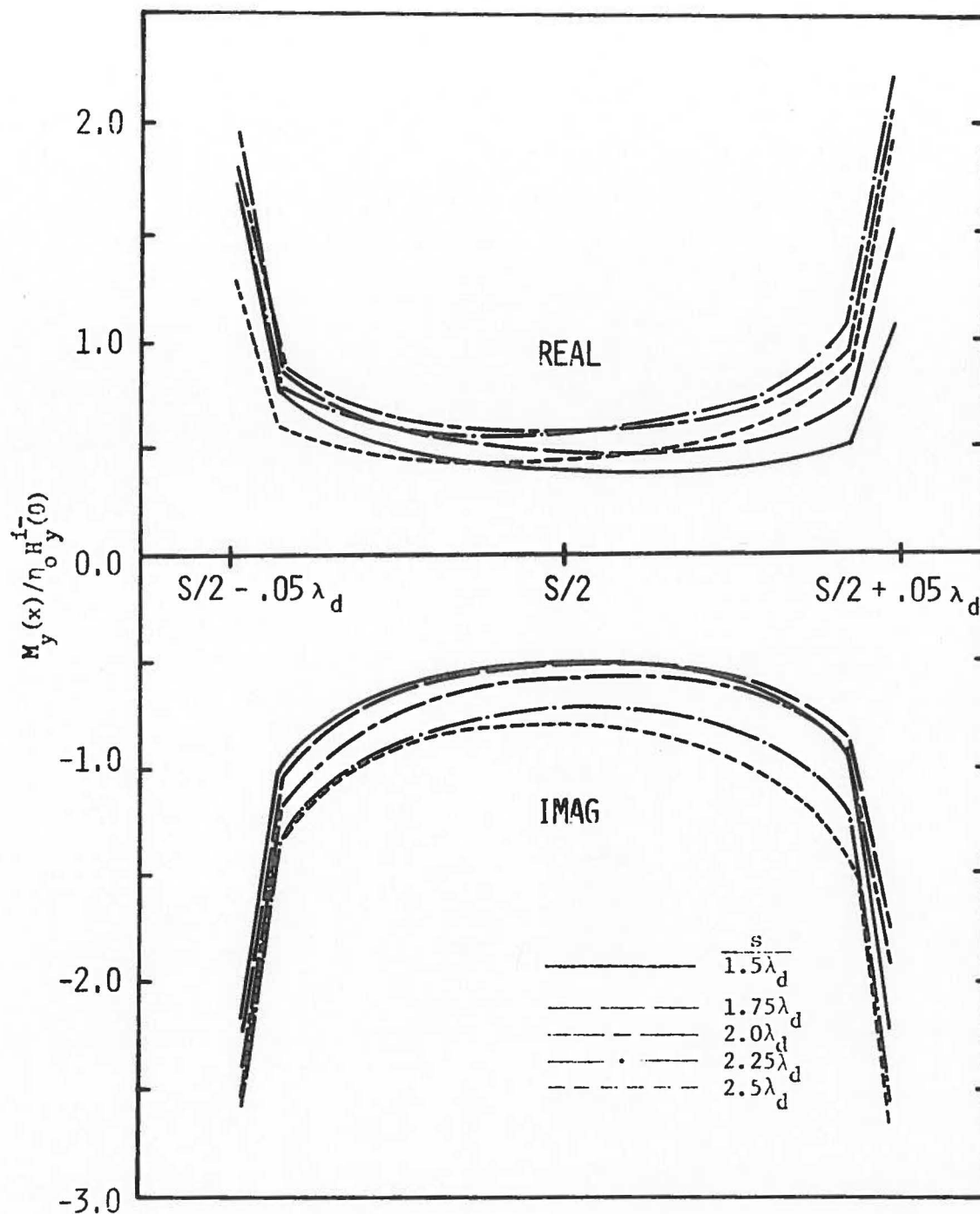


Fig. 5.27 Equivalent magnetic current $M_y(x)/n_0 H_0^t$ for two slots of width $0.1\lambda_d$ and various slot separation distances s , subject to normally incident TE excitation with dielectric slab thickness $h = \lambda_d/8$.

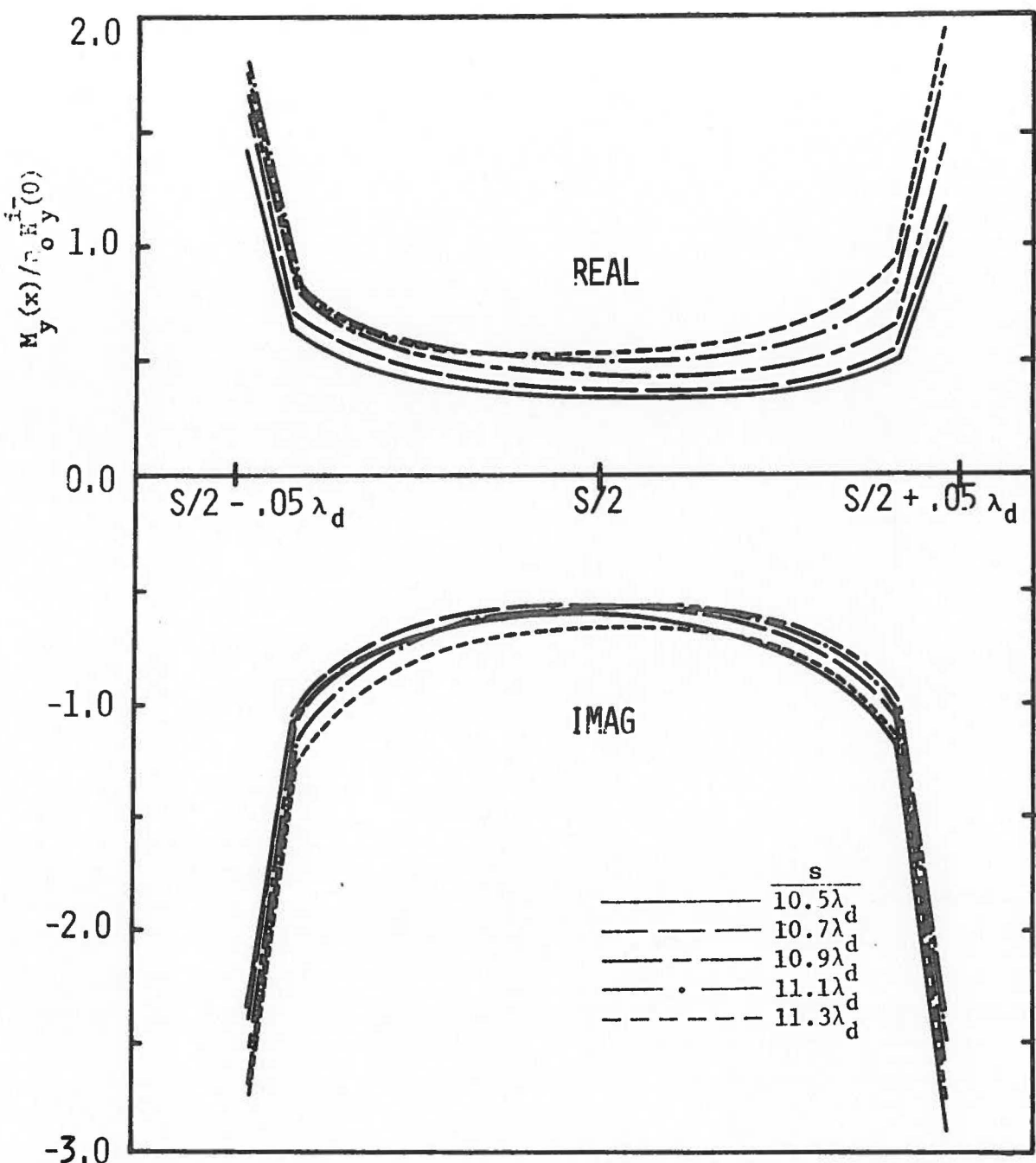


Fig. 5.28 Equivalent magnetic current $M_y (= E_x^a)$ for two slots of width $0.1\lambda_o$, subject to normally incident TE excitation when slot separation s is large and a slab of thickness $\lambda_d/8$ lies on the ground screen.

waves is evident in the slot magnetic current. Since a look at the slot magnetic current for the case of coupled slots without a dielectric slab cover indicates free space slot coupling is insignificant for separation distances greater than one free space wavelength, it is inferred that the mechanism of the surface wave is an important factor in the consideration of aperture design and analysis with applications in antenna theory.

5.4 Excitation of a Notch in a Ground Screen Covered by a Dielectric Slab

Figs. 5.29-5.34 show the equivalent magnetic currents in the aperture of a notch in a ground screen. The region above the dielectric slab covering the ground screen is assumed to be free space as is the region inside the notch. Excitation is by means of a single surface wave which is traveling in the $+x$ direction in the TE_x mode. Results are given as a function of dielectric slab thickness at a variety of notch widths and notch depths.

Normalized far magnetic field patterns are shown in Figs. 5.35-5.40 for the corresponding current distributions shown in Figs. 5.29-5.34. An interesting difference is noted between the far field patterns in conjunction with a change in the notch-slot width. The narrower notch (figs. 5.35-5.37) tends to have a broad-side far field pattern which changes toward an end-fire pattern as the slab thickness increases. Since an end-fire field pattern indicates the onset of a surface wave, then for a case in which a surface wave is yielding power to the slot a broad-side pattern would mean that power is being removed from the surface

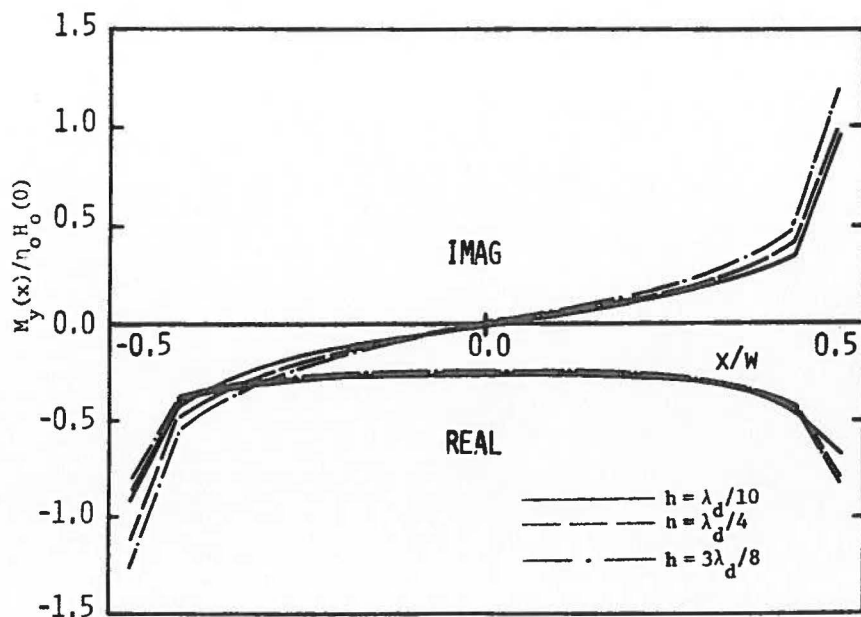
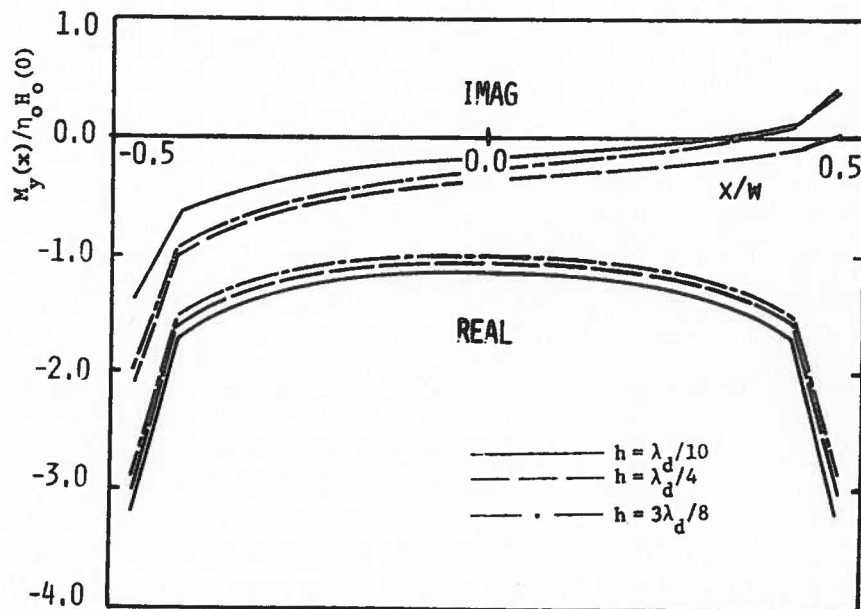
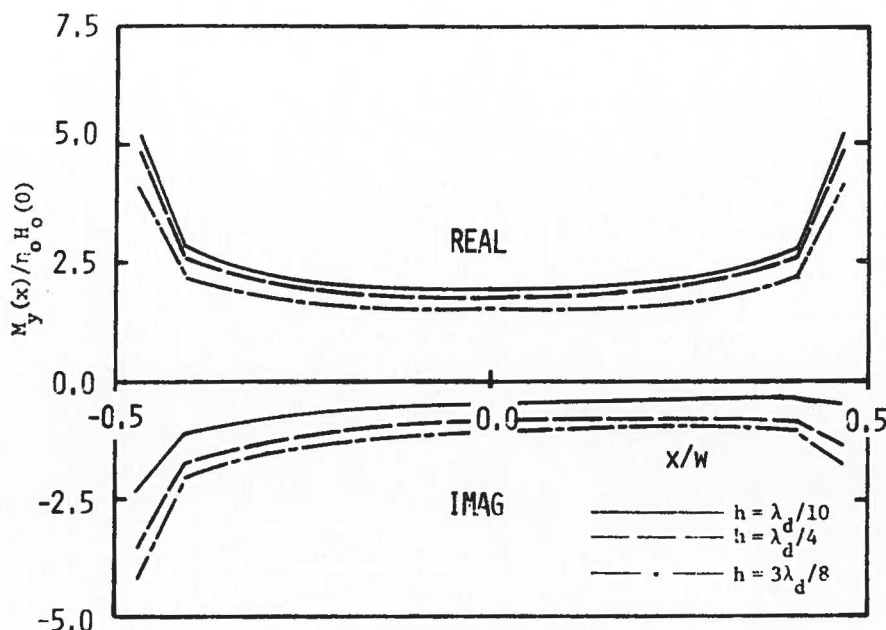


Fig. 5.29 Equivalent magnetic current $M_y(x)/H_0^H(0)$ for a notch of width $0.02\lambda_0$ and depth $0.05\lambda_0$, subject to surface wave TM_x excitation for several slab thicknesses.



5.30 Equivalent magnetic current $M_y(x)/H_0^H(0)$ for a notch of width $0.02\lambda_0$ and depth $0.125\lambda_0$, subject to surface wave TM_x excitation for several slab thicknesses.



5.31 Equivalent magnetic current $M_y (= E_x^a)$ for a notch of width $0.02\lambda_0$ and depth $0.25\lambda_0$, subject to surface wave TM_x excitation for several slab thicknesses.

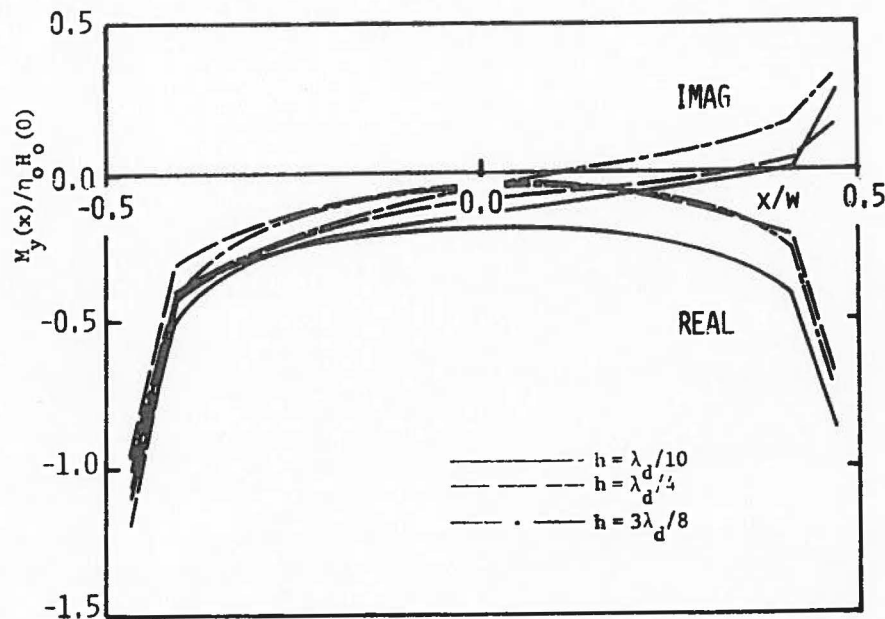


Fig. 5.32 Equivalent magnetic current $M_y (= E_x^a)$ for a notch of width $0.25\lambda_0$ and depth $0.05\lambda_0$, subject to surface wave TM_x excitation for several slab thicknesses.

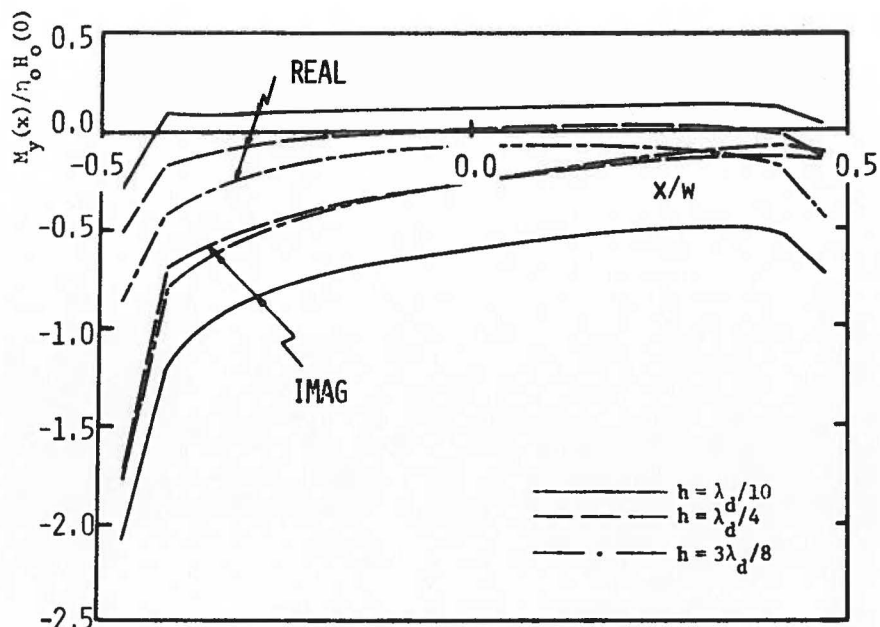


Fig. 5.33 Equivalent magnetic current $M_y (=E_x^a)$ for a notch of width $0.25\lambda_o$ and depth $0.125\lambda_o$, subject to surface wave TM_x excitation for several slab thicknesses.

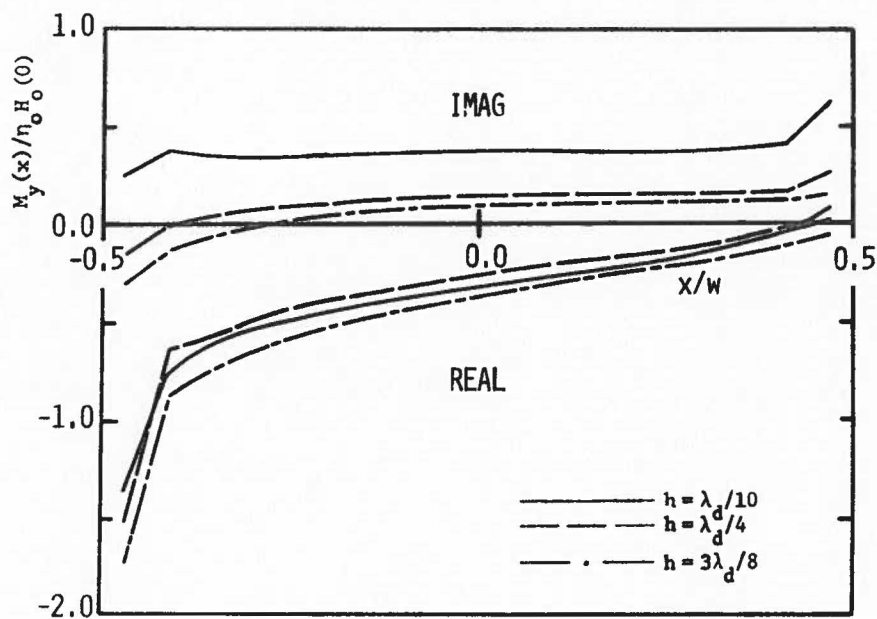


Fig. 5.34 Equivalent magnetic current $M_y (=E_x^a)$ for a notch of width $0.25\lambda_o$ and depth $0.25\lambda_o$, subject to surface wave TM_x excitation for several slab thicknesses.

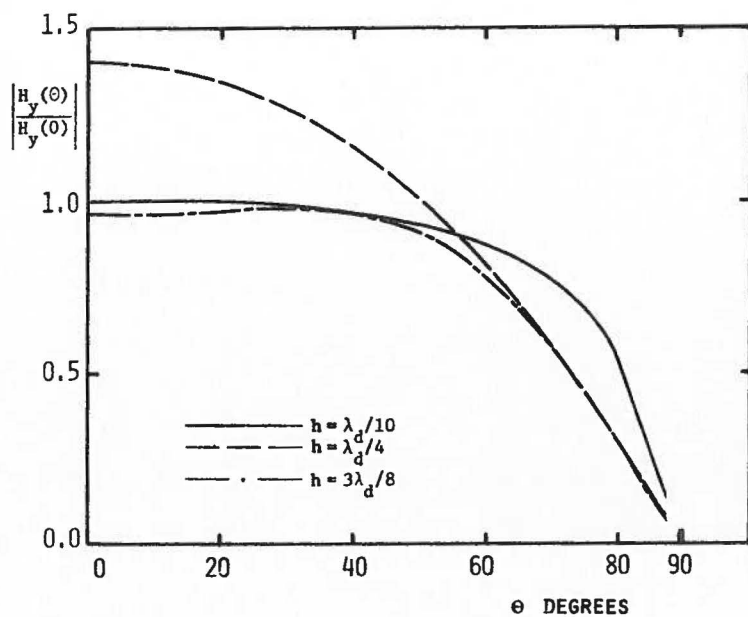


Fig. 5.35 Normalized far magnetic field for a notch of width $0.02\lambda_0$ and depth $0.05\lambda_0$, subject to surface wave TM_x excitation for several slab thicknesses.

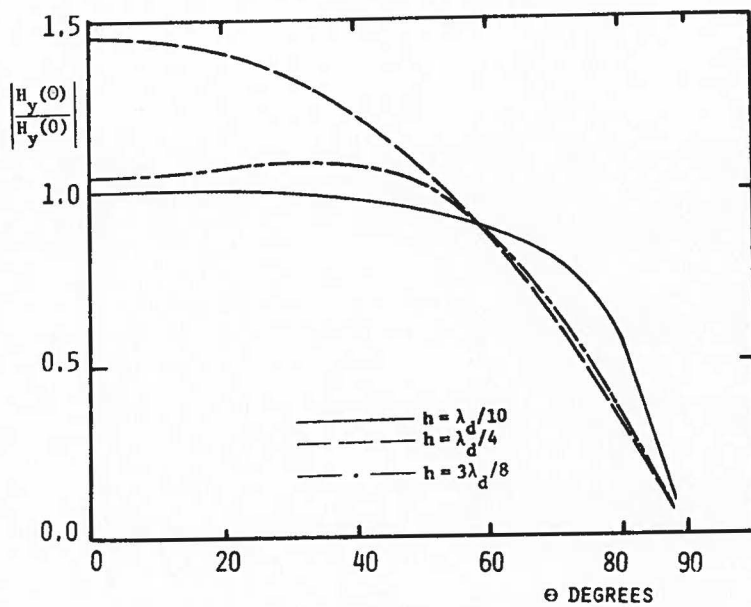


Fig. 5.36 Normalized far magnetic field for a notch of width $0.02\lambda_0$ and depth $0.125\lambda_0$, subject to surface wave TM_x excitation for several slab thicknesses.

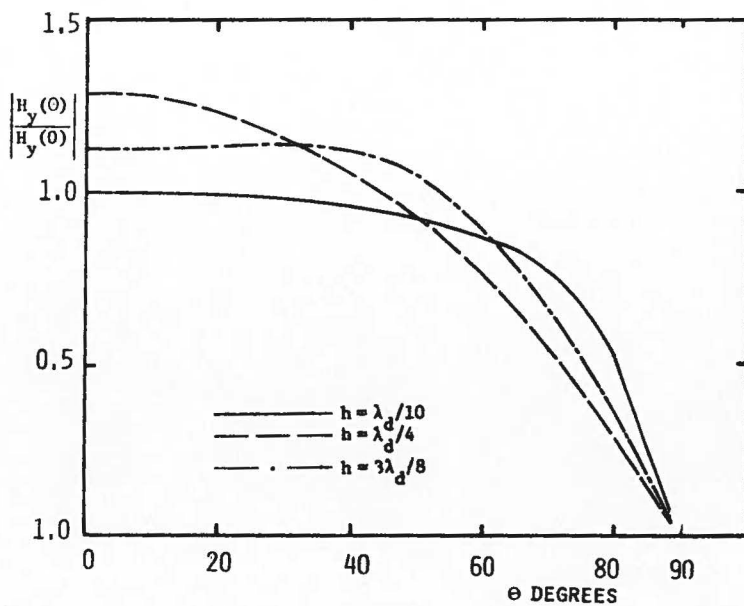


Fig. 5.37 Normalized far magnetic field for a notch of width $0.02\lambda_0$ and depth $0.25\lambda_0$, subject to surface wave TM_x excitation for several slab thicknesses.

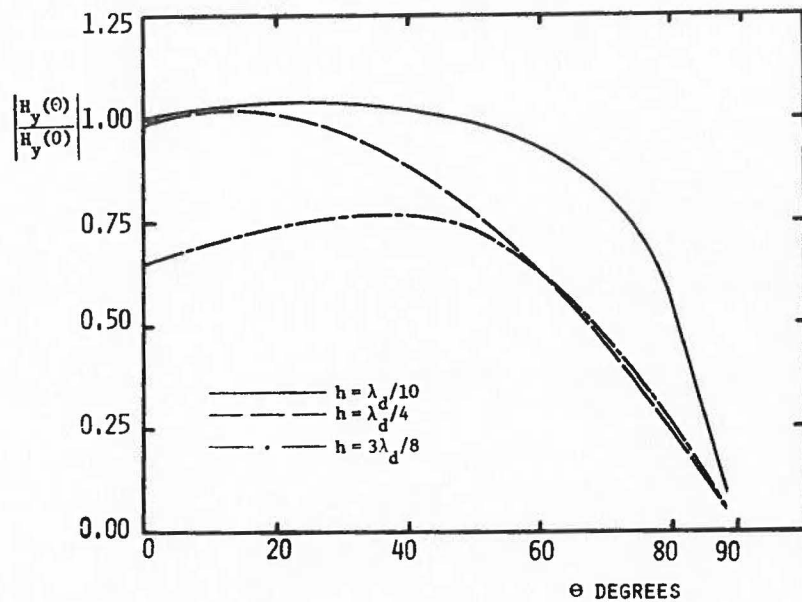


Fig. 5.38 Normalized far magnetic field for a notch of width $0.25\lambda_0$ and depth $0.05\lambda_0$, subject to surface wave TM_x excitation for several slab thicknesses.

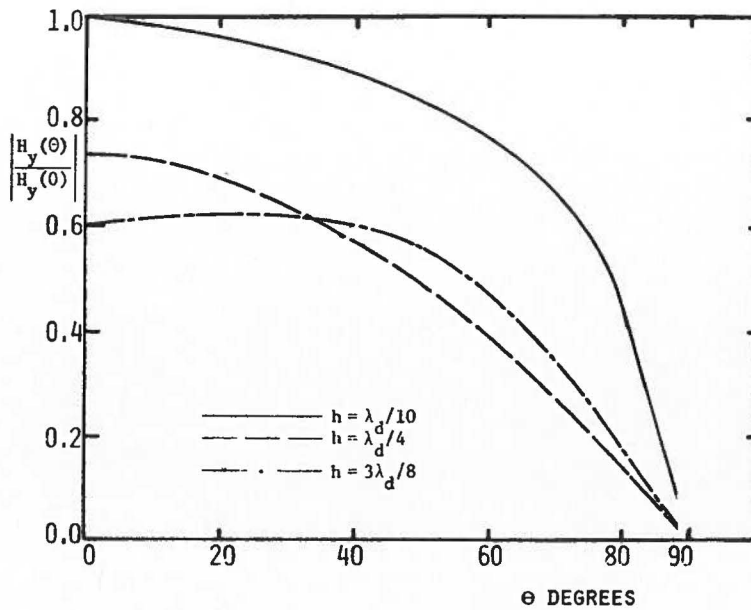


Fig. 5.39 Normalized far magnetic field for a notch of width $0.25\lambda_0$ and depth $0.125\lambda_0$, subject to surface wave TM_x excitation for several slab thicknesses.

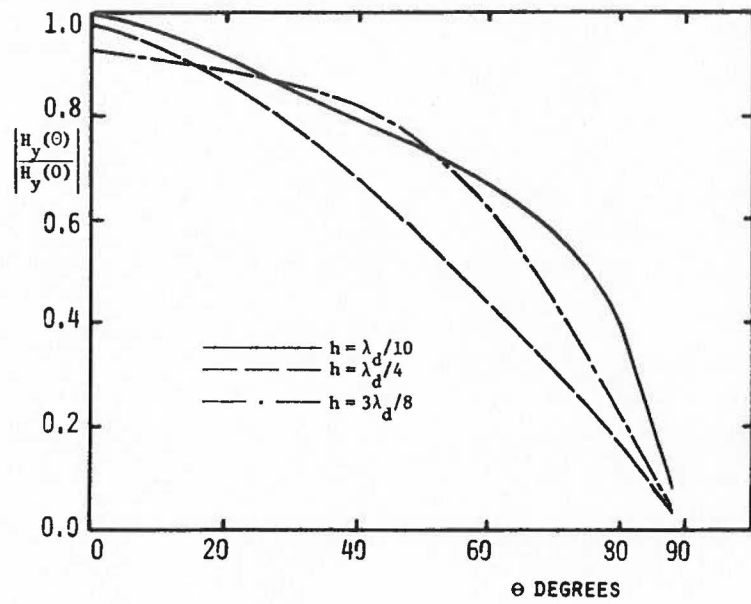


Fig. 5.40 Normalized far magnetic field for a notch of width $0.25\lambda_0$ and depth $0.25\lambda_0$, subject to surface wave TM_x excitation for several slab thicknesses.

wave and transmitted outside the dielectric slab. In each case the results show that the depth of the notch also has a decided effect upon the occurrence of surface waves.

For power considerations and due to the introduction of these variable parameters - notch depth (w), notch width (ℓ) and dielectric thickness (h) - a scattering s-parameter analysis is decidedly more convenient method of viewing results than the far field approach. The s-parameters are given in Chapter III for the case of a TM mode surface wave incident upon the region of the notch. It should be noted that applications in the area of surface and leaky wave antennas are indicated. Such applications would probably be most efficiently investigated through numerical optimization techniques geared toward varying the three above mentioned parameters in order to obtain the desired far field pattern.

APPENDIX A

GREEN'S FUNCTION SOLUTION FOR A LINE SOURCE IMBEDDED IN A DIELECTRIC SLAB

A.1 Polarization in the Direction of the Line Source

The problem of an infinite magnetic line source polarized in the direction of the infinite line and imbedded in a dielectric slab is shown in Fig. A1. The current which is y-directed and situated at a general point $z = 0$, $x = x'$ can be expressed as

$$\bar{M} = m\delta(x - x')\delta(z)\hat{y}$$

For the problems considered in this dissertation we are concerned with a situation where the region $z < 0$ is an image of the region $z > 0$. This means that regions (a) and (c) consist of the same material (i.e. $\epsilon_c = \epsilon_a$ and $\mu_c = \mu_a$). It may therefore be concluded that the electric vector potential is an even function of z . The equations for the vector potential in the three regions shown are

$$(\nabla_{xz}^2 + k_a^2)F_y^a = 0, \quad z \geq h \quad (A.1a)$$

$$(\nabla_{xz}^2 + k_b^2)F_y^b = -\epsilon_b m\delta(x - x')\delta(z), \quad h \leq z \leq -h \quad (A.1b)$$

$$(\nabla_{xz}^2 + k_a^2)F_y^c = 0, \quad z \leq -h \quad (A.1c)$$

The electric and magnetic fields can be expressed in terms of the electric vector potential in each of the three regions as

$$\bar{E} = -\frac{1}{\epsilon} \nabla \times \bar{F}$$

$$\bar{H} = -\frac{j\omega}{k^2} (k^2 + \nabla \nabla \cdot) \bar{F}$$

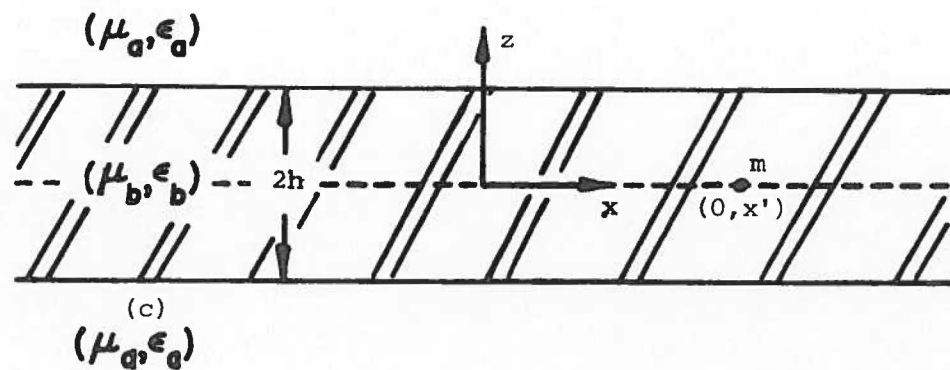


Fig. A.1 Infinite magnetic line source embedded in a dielectric slab and polarized in the y -direction.

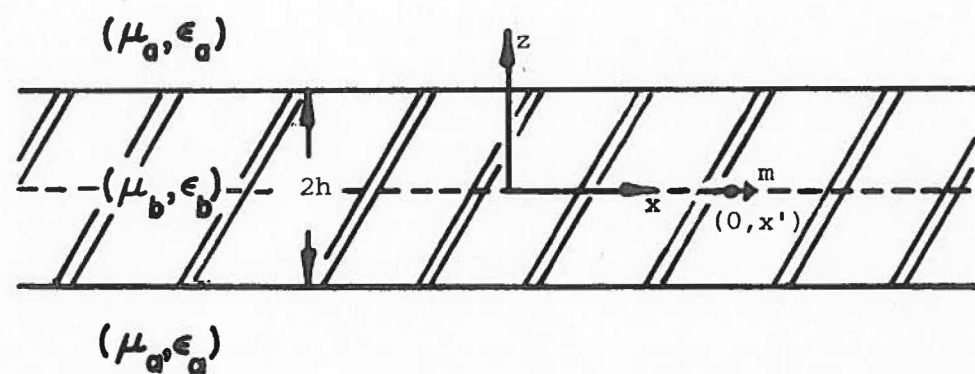


Fig. A.2 Infinite magnetic line source embedded in a dielectric slab and polarized in the x -direction.

Expanding in terms of rectangular coordinates, one finds

$$\tilde{E}_x^t = \frac{1}{\epsilon_t} \frac{\partial}{\partial z} \tilde{F}_y^t \quad (A.2a)$$

$$\tilde{E}_z^t = - \frac{1}{\epsilon_t} \frac{\partial}{\partial x} \tilde{F}_y^t \quad (A.2b)$$

$$\tilde{H}_y^t = - j\omega \tilde{F}_y^t ; t = a, b \text{ or } c \quad (A.2c)$$

The boundary conditions are found by enforcing continuity of tangential electric and magnetic fields at $z = h$. From Eq. (A.2c)

$$\tilde{F}_y^a = \tilde{F}_y^b , z = h \quad (A.3a)$$

and from (A.2a)

$$\frac{1}{\epsilon_a} \frac{\partial}{\partial z} \tilde{F}_y^a = \frac{1}{\epsilon_b} \frac{\partial}{\partial z} \tilde{F}_y^b , z = h \quad (A.3b)$$

A tilde (\sim) in the above expressions indicates that a Fourier transform has been taken in x so that the solution procedure may be accomplished in the k_x transform domain.

Constructing solutions in each region, we postulate

$$\tilde{F}_y^a = Ae^{-j\beta_a(z-h)} , z \geq h \quad (A.4a)$$

$$\tilde{F}_y^b = B \cos(\beta_b z) e^{-j\beta_b h} - \frac{j\epsilon_b^{me}}{2} e^{-jk_x x'} \frac{e^{-j\beta_b |z|}}{\beta_b} , |z| \leq h \quad (A.4b)$$

$$\tilde{F}_y^c = Ae^{j\beta_a(z+h)} , z \leq -h \quad (A.4c)$$

where

$$\beta_t = \begin{cases} \sqrt{\frac{2}{k_t^2 - k_x^2}} , k_t \geq k_x & \text{where } t = a \text{ or } b \\ -j\sqrt{\frac{2}{k_x^2 - k_t^2}} , k_t \leq k_x & \end{cases}$$

It is interesting to note that the term $\cos\beta_b z$ is due to a standing wave and is multiplied in Eq. (A.4b) by an anticipated term $e^{-j\beta_b h}$.

In (A.4b) the first term on the right forms the homogeneous solution of the transformed wave equation where B is an unknown constant coefficient to be evaluated. The second term on the right in Eq. (A.4b) is the particular solution of Eq. (A.1b) (transformed) and is the result one gets when an infinite line source lies in a homogeneous medium of infinite extent characterized by (μ_b, ϵ_b) .

From (A.3a), (A.4a) and (A.4b)

$$A = B \cos(\beta_b h) e^{-j\beta_b h} - \frac{j\epsilon_b^m}{2} e^{-jk_x' x'} \frac{e^{-j\beta_b h}}{\beta_b}, \quad z = h \quad (A.5)$$

Rearranging (A.5) one obtains

$$A - B \cos(\beta_b h) e^{-j\beta_b h} = \frac{-j\epsilon_b^m}{2} e^{-jk_x' x'} \frac{e^{-j\beta_b h}}{\beta_b}, \quad z = h \quad (A.6a)$$

From (A.3b), (A.4a) and (A.4b)

$$\begin{aligned} \left(\frac{-j\beta_a}{\epsilon_a} \right) A + \left(\frac{\beta_b}{\epsilon_b} \sin(\beta_b h) e^{-j\beta_b h} \right) B \\ = \left(\frac{-j\beta_b}{\epsilon_b} \right) \left(\frac{-j\epsilon_b^m}{2} e^{-jk_x' x'} \frac{e^{-j\beta_b h}}{\beta_b} \right), \quad z = h \end{aligned} \quad (A.6b)$$

A simultaneous solution of Eqs. (A.6a) and (A.6b) yields the coefficients A and B

$$A = \frac{-\frac{m}{2} e^{-jk_x' x'}}{\left(\frac{\beta_b}{\epsilon_b} \sin(\beta_b h) - j \frac{\beta_a}{\epsilon_a} \cos(\beta_b h) \right)} \quad (A.7)$$

$$B = \frac{\frac{m\epsilon_b}{2\beta_b} \left(\frac{\beta_b}{\epsilon_a} - \frac{\beta_b}{\epsilon_b} \right) e^{-jk_x x'}}{\left(\frac{\beta_b}{\epsilon_b} \sin \beta_b h - j \frac{\beta_a}{\epsilon_a} \cos \beta_b h \right)} \quad (A.8)$$

Placing the above constants into (A.4a) and (A.4b), then transforming with respect to k_x , we get

$$F_y^a = -\frac{m}{4\pi} \int_{k_x=-\infty}^{\infty} \frac{e^{-j\beta_a(z-h)} e^{jk_x(x-x')}}{\frac{\beta_b}{\epsilon_b} \sin \beta_b h - j \frac{\beta_a}{\epsilon_a} \cos \beta_b h} dk_x, \quad z \geq h \quad (A.9)$$

$$F_y^b = \frac{m\epsilon_b}{4\pi} \int_{k_x=-\infty}^{\infty} \frac{\left(\frac{\beta_a}{\epsilon_a} - \frac{\beta_b}{\epsilon_b} \right) \cos \beta_b z \frac{e^{-j\beta_b h}}{\beta_b} e^{jk_x(x-x')}}{\frac{\beta_b}{\epsilon_b} \sin \beta_b h - j \frac{\beta_a}{\epsilon_a} \cos \beta_b h} dk_x$$

$$-\frac{jme_b}{4\pi} \int_{k_x=-\infty}^{\infty} \frac{e^{-j\beta_b|z|} e^{jk_x(x-x')}}{\beta_b} dk_x, \quad |z| \leq h \quad (A.10)$$

With a rearrangement of terms, the two integrals on the right hand side of (A.10) can be combined to form the expression

$$F_y^b = -\frac{jme_b}{4\pi} \int_{k_x=-\infty}^{\infty} \left(\frac{1 - \Gamma_k e^{-j2\beta_b(h-|z|)}}{1 + \Gamma_k e^{-j2\beta_b h}} \right) \frac{e^{-j\beta_b|z|} e^{jk_x(x-x')}}{\beta_b} dk_x, \quad |z| \leq h \quad (A.11)$$

However, it is also recognized (see Chapter IV) that the second term on the right hand side of (A.10) is a Hankel function of the second kind. Again,

with a modification of terms, we arrive at an alternative form of Eq. (A.10)

$$F_y^b = \frac{-jm\epsilon_b}{4} \left[-\frac{4}{\pi} \int_{k_x=-\infty}^{\infty} \left(\frac{\Gamma_k e^{-j2\beta_b h}}{1 + \Gamma_k e^{-j2\beta_b h}} \right) \frac{\cos\beta_b z \cos k_x (x-x')}{\beta_b} dk_x + H_0^2(k_b \sqrt{z^2 + (x-x')^2}) \right], \quad |z| \leq h \quad (A.12)$$

where

$$\Gamma_k = \frac{\beta_a \epsilon_b - \beta_b \epsilon_a}{\beta_a \epsilon_b + \beta_b \epsilon_a}$$

and

$$\beta_a = \begin{cases} \frac{\sqrt{k_a^2 - k_x^2}}{b}, & k_a \geq k_x \\ -j \sqrt{\frac{k_x^2 - k_a^2}{b}}, & k_a \leq k_x \end{cases} \quad (A.13)$$

Close inspection of (A.11) and (A.12) reveals that each of these two forms of F_y^b has its own particular advantages and disadvantages when viewed from a numerical integration standpoint. For example, the integrand of (A.11) contains only one singularity, which occurs predictably at the point in k_x marked by the initiation of a surface wave. However, past $k_x = k_b$ the integrand decays very slowly and, as a result, time consuming integration techniques are required for evaluation of the integral. Form (A.12) has the familiar Hankel function representing a source in a homogeneous space, plus an integral which is the Sommerfeld correction term accounting for the presence of the dielectric slab. This correction

term contains a surface wave singularity as well as a singularity resulting from the removal of the Hankel function. The correction term integral, however, may be readily evaluated by various numerical integration techniques. Form (A.12) is therefore chosen as a representative solution for F_y^b and is used throughout this paper.

The expression for vector potential in the region $z \geq h$ can also be placed in a convenient form,

$$F_y^a = \frac{-jme_a}{2\pi} \int_{k_x=0}^{\infty} \left(\frac{1 + \Gamma_k}{1 + \Gamma_k e^{-j2\beta_b h}} \right) \frac{e^{-j\beta_b h} e^{-j\beta_a (z-h)}}{\beta_a} \cos k_x (x-x') dk_x$$

, $z \geq h$ (A.14)

Caution must be exercised when taking the square root in Eq. (A.14) above. If k_a is real then as k_x goes from zero to infinity the value of β_a in the complex plane changes from a purely real to a purely imaginary quantity. If the medium is complex, then k_a in the practical case lies in the fourth quadrant (i.e., have a positive real and negative imaginary part). It is also necessary that β_a lie in the fourth quadrant in order that F_y^a represent an outwardly propagating, exponentially decaying field.

For a detailed explanation of the problem, the reader should refer to Section A.III.

A.II Polarization Perpendicular to the Direction of the Line Source and Parallel to the Interface

Fig. A2 depicts the case of a line source which is polarized parallel to the dielectric interface. The current is situated at a general point $z = 0$, $x = x'$ and is written as

$$\bar{M} = m\delta(x-x')\delta(z)\hat{x} .$$

It is found in Section A.I that the vector potential is an even function with respect to z . This observation, which allows a reduction by one in the number of unknowns in the problem, is also made in the present case. The dielectric materials composing regions (a) and (c) are therefore assumed to have identical electrical properties. It is then necessary to apply boundary conditions only at the interface between regions (a) and (b). The equations for the vector potential in these two regions are

$$(\nabla_{xz}^2 + k_a^2)F_x^a = 0 , \quad z \geq h$$

and

$$(\nabla_{xz}^2 + k_b^2)F_x^b = -\epsilon_b m\delta(x-x')\delta(x) , \quad |z| \leq h$$

where it is assumed that no variation occurs in the vector potential with respect to the y -direction. The electric and magnetic fields in terms of these potentials are

$$E_y^a = -\frac{1}{\epsilon_a} \frac{\partial}{\partial z} F_x^a \quad (A.15a)$$

$$H_x^a = -\frac{j\omega}{k_a^2} (k_a^2 + \frac{\partial^2}{\partial x^2}) F_x^a \quad (A.15b)$$

$$H_z^a = -\frac{j\omega}{k_a^2} \frac{\partial^2}{\partial x \partial z} F_x^a \quad (A.15c)$$

From (A.15a) or (A.15c) and continuity of field at the interface

$$\frac{1}{\epsilon_b} \frac{\partial}{\partial z} \tilde{F}_x^b = \frac{1}{\epsilon_a} \frac{\partial}{\partial z} \tilde{F}_x^a , \quad z = h \quad (A.16)$$

and from (A.15b)

$$\frac{\beta_b^2}{k_b^2} \tilde{F}_x^b = \frac{\beta_a^2}{k_a^2} \tilde{F}_x^a , \quad z = h \quad (A.17)$$

where the tilde (\sim) once again indicates Fourier transformation with respect to the x coordinate.

Constructing solutions in the transform domain for the two regions of interest, we arrive at

$$\tilde{F}_x^b = A \cos \beta_b z e^{-j\beta_b h} - \frac{j\epsilon_m}{2\beta_b} e^{-jk_x' x'} e^{-j\beta_b |z|} , \quad |z| \leq h \quad (A.18)$$

$$\tilde{F}_x^a = B e^{-j\beta_a (z-h)} , \quad z \geq h \quad (A.19)$$

Application of the boundary conditions (A.16) and (A.17) to Eqs. (A.18) and (A.19) yields two equations with the two unknowns A and B . Solving these two equations simultaneously, we arrive at expressions for the constants

$$A = \frac{jm\epsilon_b}{\beta_b} e^{-jk_x' x'} \left(\frac{\frac{\Gamma}{g} e^{-j\beta_b h}}{\frac{\Gamma}{g} e^{-j2\beta_b h} + 1} \right) \quad (A.20)$$

$$B = \frac{-jm\beta_b k_a^2 e^{-jk_x' x'}}{\beta_a \omega^2 (\beta_b \mu_a + \beta_a \mu_b)} \left(\frac{e^{-j\beta_b h}}{\frac{\Gamma}{g} e^{-j2\beta_b h} + 1} \right) \quad (A.21)$$

where

$$\Gamma_g = \frac{\beta_b^\mu a - \beta_a^\mu b}{\beta_b^\mu a + \beta_a^\mu b}$$

and ω represents the frequency of the excitation field.

When the constants from Eqs. (A.20) and (A.21) are placed into the expressions for vector potential, the solutions are

$$F_x^b = \frac{-jme_b}{4\pi} \int_{k_x=-\infty}^{\infty} \left(\frac{1 - \frac{\Gamma_g e^{-j2\beta_b(h-|z|)}}{e^{-j2\beta_b h}}}{1 + \frac{\Gamma_g e^{-j2\beta_b h}}{e^{-j2\beta_b h}}} \right) \frac{e^{-j\beta_b |z|} e^{jk_x(x-x')}}{\beta_b} dk_x , \quad |z| < h \quad (A.22a)$$

or

$$F_x^b = \frac{-jme_b}{4} \left[H_0^{(2)} \left(k_b \sqrt{(x-x')^2 + z^2} \right) - \frac{4}{\pi} \int_{k_x=0}^{\infty} \left(\frac{\frac{\Gamma_g e^{-j2\beta_b h}}{e^{-j2\beta_b h}}}{\frac{\Gamma_g e^{-j2\beta_b h}}{e^{-j2\beta_b h}} + 1} \right) \frac{\cos k_x(x-x') \cos \beta_b z}{\beta_b} dk_x \right], \quad |z| \leq h \quad (A.22b)$$

and

$$F_x^a = \frac{-jme_a}{4\pi} \int_{k_x=-\infty}^{\infty} \left(\frac{1 + \frac{\Gamma_g}{e^{-j2\beta_b h}}}{1 + \frac{\Gamma_g e^{-j2\beta_b h}}{e^{-j2\beta_b h}}} \right) \frac{e^{-j\beta_b h} e^{-j\beta_a(z-h)} e^{jk_x(x-x')}}{\beta_a} dk_x , \quad z \geq h \quad (A.23)$$

A.III Integration Path and Branch Cut Specification

The Sommerfeld integral is not completely specified until the allowable region for the path of integration is indicated and the branch cuts

are constrained to approach infinity in the proper fashion. It will be shown in this section that a determination of the allowable region for the path of integration will automatically constrain the branch cut in the desired manner. The purpose of this analysis is two-fold. First, although the path of integration of the Sommerfeld integral is generally defined to be along the real axis, allowance must be made for the proper circumvention of the surface wave poles and branch points which in certain cases lie on the real axis. In making a path deformation around a pole or branch point it is necessary to know whether the deformation should be above or below the pole or branch point. This information is supplied by a specification of the allowable region. Secondly, evaluation of the Sommerfeld integral by closure of the path of integration at infinity has proven to be more expeditious in certain particular cases than real axis evaluation. In such cases the branch cut must approach infinity in a manner which allows the integrand of Sommerfeld to approach zero. In this section the proper branch of β , a representative square root term, is found and the branch cuts due to the multivalued nature of β are suitably constrained.

The Sommerfeld integral may be written in the general form

$$I(x, z) = \int_{k_x = -\infty}^{\infty} f(x, k_x) e^{-j\beta z} dk_x \quad (A.24)$$

where z is a large positive real parameter and β is defined

$$\beta = \begin{cases} \sqrt{k^2 - k_x^2}, & k_x \leq k \\ -j\sqrt{k_x^2 - k^2}, & k_x \geq k \end{cases}$$

The technique presented here can with minor modifications also be applied to determine the proper branch cut for negative values of z .

Finding the proper form of the branch cut entails defining a proper Riemann sheet over which the integration of Eq. (A.24) may be carried out. For positive z , the requirements of exponential decay and outward propagation place the following restrictions on β

$$\operatorname{Re}\beta > 0$$

$$\operatorname{Im}\beta < 0 \quad (\text{A.25})$$

Using the above conditions, we require that the top sheet of the complex β -plane now be defined as having $\operatorname{Im}\beta < 0$.

Let

$$\beta^2 = Ae^{j\theta}$$

so

$$\beta = A^{\frac{1}{2}}e^{j\theta/2}$$

where A is real. This means that, if $\operatorname{Im}(\beta) < 0$, then $-\pi < \theta/2 < 0$ or $-2\pi < \theta < 0$, so that the branch cut in the β^2 -plane is along the positive real axis (i.e., $\operatorname{Re}\beta^2 > 0$, $\operatorname{Im}\beta^2 = 0$ on the branch cut), (see Fig. A3). We shall now undertake a procedure to map from the β^2 -plane into the complex k_x^2 -plane.

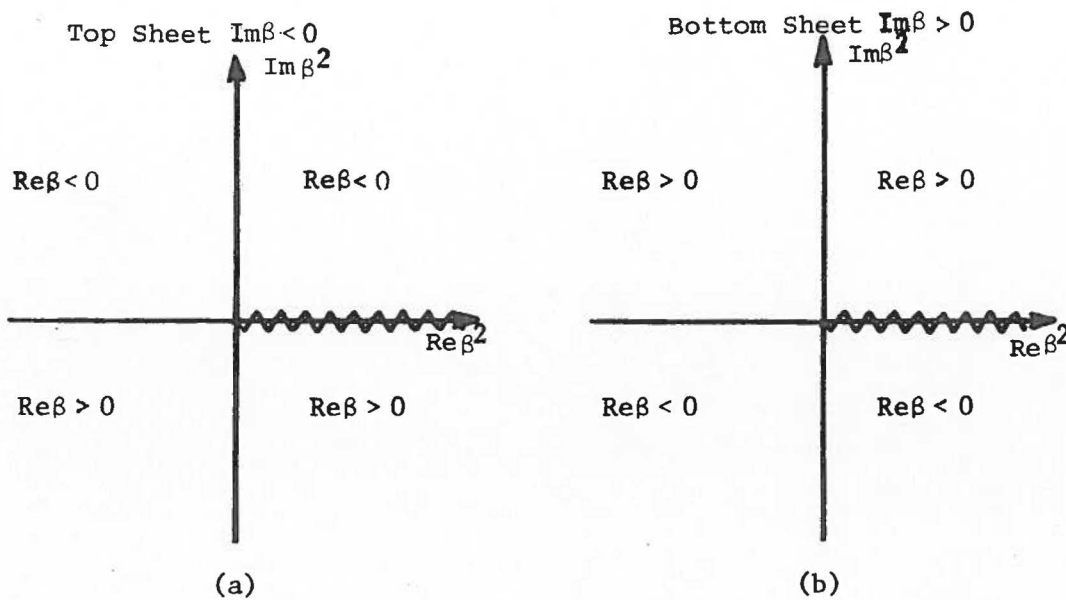


Fig. A.3 Top and bottom sheets of the Riemann surface for the β^2 -plane.

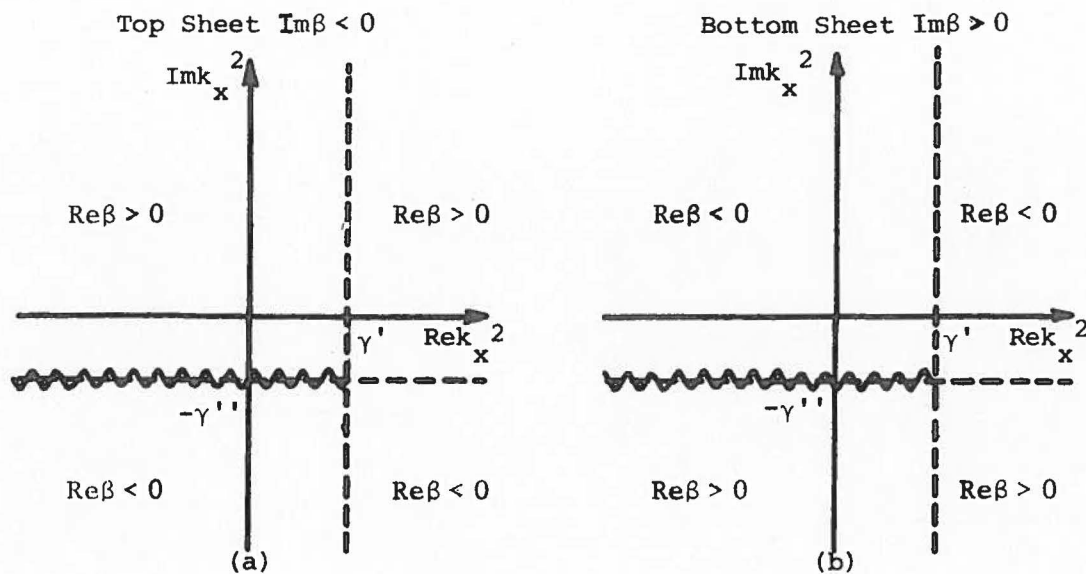


Fig. A.4 Top and bottom sheets of the Riemann surface for the k_x^2 -plane.

In practical situations k^2 has the form

$$k^2 = \omega^2 \mu \epsilon - j\omega \mu \sigma = \gamma' - j\gamma''$$

where γ' and γ'' are positive real quantities. Since

$$\begin{aligned} k_x^2 &= -\beta^2 + k^2 \\ &= -\beta^2 + \gamma' - j\gamma'' \end{aligned} \quad (\text{A.26})$$

a mapping from the β^2 -plane to the k_x^2 -plane may be easily performed. We

see from Fig. A4a that on the top sheet along the cut

$$\operatorname{Re} k_x^2 \leq \gamma' \quad (\text{A.27})$$

$$\operatorname{Im} k_x^2 = -\gamma'' \quad (\text{A.28})$$

The value of β in each quadrant of the k_x^2 -plane is determined by noticing that in the β^2 -plane $\operatorname{Im} \beta < 0$ on the top sheet and vice versa on the bottom sheet. With regard to the relative value of $\operatorname{Re} \beta$ we thus see from Eq. (A.26) that the positive imaginary part of the k_x^2 -plane is directly related to the negative imaginary part of the β^2 -plane with $\operatorname{Im} k^2$ accounting for a small downward shift in the definition of these two regions.

In order to map the k_x^2 -plane into the k_x -plane let

$$k_x = k_{x_r} + jk_{x_i} \quad (\text{A.29})$$

or

$$k_x^2 = (k_{x_r}^2 - k_{x_i}^2) + j2k_{x_r} k_{x_i} \quad (\text{A.30})$$

So from the properties of Eqs. (A.27) and (A.28) we see that the branch cut in the k_x -plane must satisfy the following conditions:

$$\operatorname{Re} k_x^2 = k_{x_r}^2 - k_{x_i}^2 \leq \gamma' \quad (\text{A.31})$$

$$\operatorname{Im} k_x^2 = 2k_{x_r} k_{x_i} = -\gamma'' \quad (\text{A.32})$$

Conditions (A.31 and A.32) are plotted in Figs. A5a and A5b respectively in the complex k_x -plane. Notice that Eq. (A.31) involves a region whereas Eq. (A.32) involves a pair of hyperbolic curves. Combining (A.31) and (A.32) one arrives at the desired branch cut for the top and bottom sheets of the Riemann surface in the k_x -plane (see Fig. A6). It is noted from the k_x^2 -plane that, when $\operatorname{Im} k_x^2 > -\gamma''$ then $\operatorname{Re}\beta > 0$. Thus, the allowable region in the k_x -plane for which $\operatorname{Re}\beta > 0$ is that where $2k_{x_r} k_{x_i} > -\gamma''$. This region is shaded in Fig. A6.

The preferred conditions ($\operatorname{Re}\beta > 0$, $\operatorname{Im}\beta < 0$) now occur everywhere in the crosshatched region of the k_x -plane in Fig. A6a. We also point out that in the region not crosshatched the wave is propagating in an improper direction but will decay to zero when $z \rightarrow \infty$ because $\operatorname{Im}\beta < 0$ on the top sheet.

Notice that along the cut in the k_x -plane $\operatorname{Im}\beta = 0$. This must be true since on the top sheet $\operatorname{Im}\beta < 0$ and on the bottom sheet, which is accessed through the cut, $\operatorname{Im}\beta > 0$. Also along the dashed line extension to the cut $\operatorname{Re}\beta = 0$. However, $\operatorname{Re}\beta \neq 0$ along the cut since the sign of $\operatorname{Re}\beta$ does not change when passing from one sheet of the Riemann surface to another. This means that the exponential term in Eq. (A.26), when evaluated along a branch cut on either side, will be purely oscillatory

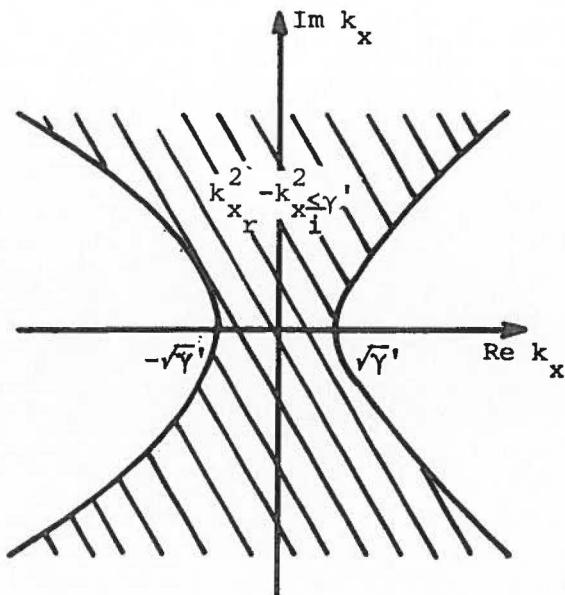


Fig. A.5a Region of validity for $k_{x_r}^2 - k_{x_i}^2 \leq \gamma'$ in the k_x -plane.

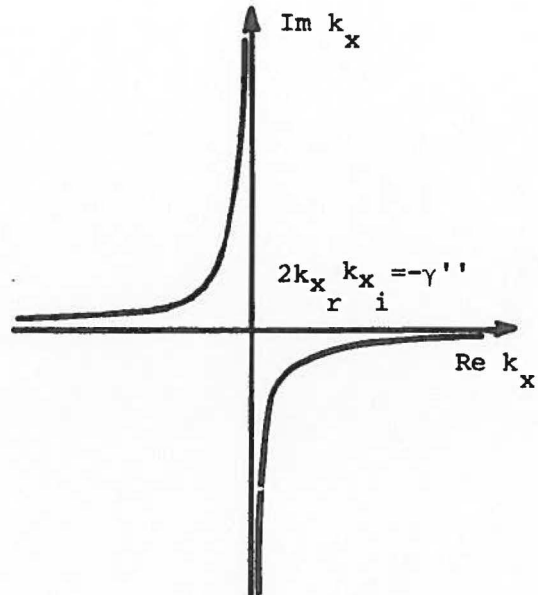


Fig. A.5b Curves in the k_x -plane satisfying $2k_{x_r} k_{x_i} = -\gamma''$.

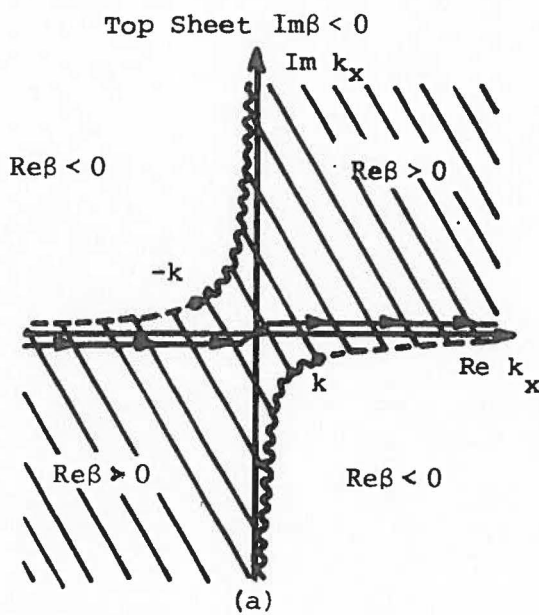
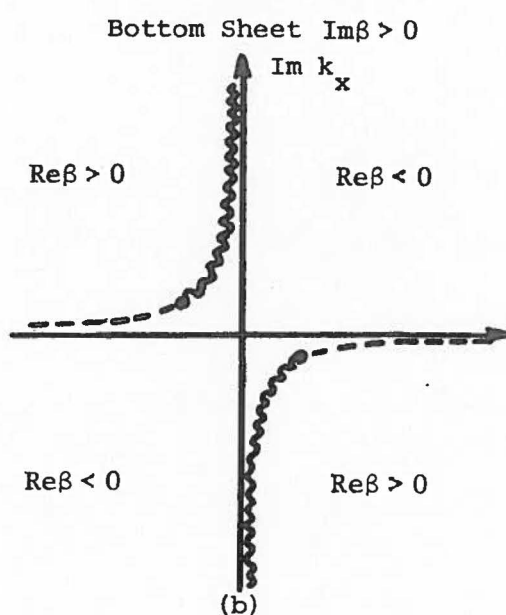


Fig. A.6 Top and bottom sheets of the Riemann surface for the k_x -plane.



due to the absence of a real part in the exponential exponent. However, for the integrals considered in this paper decay does occur if the integrant of (A.24) is evaluated along the imaginary k_x -axis due to the fact that $f(x, k_x)$ is made up of an exponential term $\exp jk_x(x-x')$.

APPENDIX B

FAR FIELDS

It is often necessary to know the field distribution at a distance many wavelengths from the vicinity of the slot. This far field problem for dielectric covered slots is investigated in the following sections. This study is accomplished by first expressing the magnetic field outside and inside the dielectric slab region in terms of the known slot electric field which has been found by numerical solution of the integral equations in the previous chapters. In order to rid the Sommerfeld integral of a branch cut and also form an integral more easily handled by asymptotic techniques a mapping to the angular domain (α -plane) is undertaken. The integral appearing in the resulting expression for the magnetic field is evaluated using the saddle point integration procedure. A discussion of surface and leaky-wave poles and how their residues are contained in the magnetic field expression is also included in the following sections.

B.1 A General Magnetic Field Expression

Using the Green's function derived in Appendix A, the electric vector potential can be written

$$F_y^a = -\frac{j\epsilon_a}{4\pi} \int_{x'=-l/2}^{l/2} 2M(x') \left[\int_{k_x=-\infty}^{\infty} \left(\frac{1 + \Gamma_k}{1 + \Gamma_k e^{-j2\beta_b h}} \right) \right. \\ \left. x' \frac{e^{-j\beta_b h}}{\beta_a} \frac{e^{-j\beta_a(z-h)}}{e^{jk_x(x-x')}} dk_x \right] dx' , z \geq h \quad (B.1)$$

$$F_y^b = \frac{-j\epsilon_b}{4\pi} \int_{x'=-l/2}^{l/2} 2M(x') \left[\int_{k_x=-\infty}^{\infty} \left(\frac{1 - \Gamma_k e^{-j2\beta_b(h-z)}}{1 + \Gamma_k e^{-j2\beta_b h}} \right) x' \frac{e^{-j\beta_b z} e^{jk_x(x-x')}}{\beta_b} dk_x \right] dx', \quad 0 \leq z \leq h \quad (B.2)$$

where

$$\Gamma_k = \frac{\beta_a \epsilon_b - \beta_b \epsilon_a}{\beta_a \epsilon_b + \beta_b \epsilon_a}$$

with the wave number for regions (a) and (b) defined

$$\beta_{ab} = \begin{cases} \sqrt{\frac{k_a^2}{b} - k_x^2}, & k_x \leq \frac{k_a}{b} \\ -j \sqrt{\frac{k_x^2}{b} - \frac{k_a^2}{b}}, & k_x \geq \frac{k_a}{b} \end{cases}$$

which have propagation constants

$$\frac{k_a}{b} = \omega \sqrt{\frac{\mu_a \epsilon_a}{b b}}$$

Although we always choose, for numerical results in this paper, situations where the electrical parameters of the medium outside the dielectric slab are those of free space, it improves the generality of a mathematical formulation of the far fields to assume a dielectric constant ϵ_a containing a lossy part. Therefore, unless otherwise specified, ϵ_a and ϵ_b are assumed to be complex quantities.

The magnetic field is found from the vector potential equation

$$\frac{ex}{H_y^{in}} = -\frac{j\omega}{k_a^2} (k_a^2 + \nabla \cdot) \frac{a}{b} F_y^b(x, z) \hat{y}$$

which, due to the absence of a y -variation in vector potential, yields

$$H_y^{in} = -j\omega F_y^b(x, z)$$

Substituting Eqs. (B.1) and (B.2) into the above equation results in the following expressions for the magnetic field

$$H_y^{ex} = -\frac{k_a}{2\pi n_a} \int_{x'=-l/2}^{l/2} M(x') \int_{k_x=-\infty}^{\infty} \left(\frac{1 + \Gamma_k}{1 + \Gamma_k e^{-j2\beta_b h}} \right) x \frac{e^{-j\beta_b h} - j\beta_b (z-h)}{\beta_a} \frac{e^{jk_x(x-x')}}{dk_x dx'} , z \geq h \quad (B.3)$$

$$H_y^{in} = -\frac{k_b}{2\pi n_b} \int_{x'=-l/2}^{l/2} M(x') \int_{k_x=-\infty}^{\infty} \left(\frac{1 - \Gamma_k e^{-j2\beta_b (h-z)}}{1 + \Gamma_k e^{-j2\beta_b h}} \right) x \frac{e^{-j\beta_b z} - j\beta_b (x-x')}{\beta_b} dk_x dx' , 0 \leq z \leq h \quad (B.4)$$

It would be excessively difficult to perform the above integrations numerically. Of major concern in attempting a numerical procedure is numerous oscillations of the integrand brought about by large values of z and x which designate the far field observation point. We resolve this

difficulty by resorting to a combination of numerical and analytical methods. This technique has proven to be effective and is outlined in the following paragraphs for the integrals of the type displayed in Eqs. (B.3) and (B.4).

First, we note that the value of $M(x)$ is already known at discrete points along the slot since the integral equations have been solved for the various cases in previous chapters. If we assume as before that

$$M(x) = \sum_{n=1}^N u_n(x) C_n$$

where

$$u_n(x) = \begin{cases} 1 & , \quad x \in (x_n - \Delta/2, x_n + \Delta/2) \\ 0 & , \quad \text{otherwise} \end{cases}$$

and interchange the order of integration in (B.3) then we get the following form

$$H_y^{ex} = -\frac{k_a}{2\pi n_a} \sum_{n=1}^N C_n \int_{k_x=-\infty}^{\infty} \left(\frac{1 + \Gamma_k}{1 + \Gamma_k e^{-jk_x h}} \right) \frac{e^{-jk_b h} e^{-jk_a (z-h)}}{\beta_a} e^{jk_x x} dk_x$$

$$x \left(\int_{x'=x_n - \Delta/2}^{x_n + \Delta/2} e^{-jk_x x'} dx' \right) dk_x, \quad z \geq h$$

where Δ is the distance between match points in the numerical solution procedure. Performing the integration of the bracketed term above, the magnetic field now becomes

$$H_y^{ex} = -\frac{k_a \Delta}{2\pi n_a} \sum_{n=1}^N c_n \int_{k_x=-\infty}^{\infty} \left(\frac{1 + \Gamma_k e^{-j2\beta_b h}}{1 + \Gamma_k e^{-j2\beta_b h}} \right) \frac{e^{-j\beta_b h} e^{-j\beta_a (z-h)} e^{jk_x (x-x_n)}}{\beta_a} \\ \times \left(\frac{\sin \frac{k_x \Delta}{2}}{\frac{k_x \Delta}{2}} \right) dk_x, \quad z \geq h \quad (B.5)$$

and

$$H_y^{in} = -\frac{k_b \Delta}{2\pi n_b} \sum_{n=1}^N c_n \int_{k_x=-\infty}^{\infty} \left(\frac{1 - \Gamma_k e^{-j2\beta_b (h-z)}}{1 + \Gamma_k e^{-j2\beta_b h}} \right) \frac{e^{-j\beta_b z} e^{jk_x (x-x_n)}}{\beta_b} \\ \times \left(\frac{\sin \frac{k_x \Delta}{2}}{\frac{k_x \Delta}{2}} \right) dk_x, \quad 0 \leq z \leq h \quad (B.6)$$

It is next noted that for the determination of the far fields either z or x or both must be a large quantity. With this requirement in hand one can appeal to the large body of knowledge concerning the evaluation of integrals by the use of asymptotic methods [28,29]. In dealing with the particular integrals in Eqs. (B.5) and (B.6) we rely on several books [31,32,33] which treat various phases of the problem in some detail.

B.2 Surface and Leaky Wave

Before proceeding with a detailed explanation of how to handle the integrals in Eqs. (B.5) and (B.6) it is best to first consider the problem determination of the surface waves in a dielectric slab over a ground plane. A conclusion concerning the range of k_x over which surface waves

occur is not easily drawn from simple observation of the integrands of (B.5) and (B.6). With this knowledge, one can gain a better understanding of how each section of the spectral distribution contributes to the determination of the far fields. A method for finding the propagation constants for surface waves has been included in this paper as Appendix C. Reference to this section indicates that surface wave poles lie in the range $k_a < |k_x| < k_b$. It is also shown in Appendix C that an approximation of the pole locations for TM surface waves is made by use of graphical techniques by determining points of intersection of the following two equations,

$$(\beta_a h)^2 + (\beta_b h)^2 = (k_a h)^2 (\hat{\mu}_b \hat{\epsilon}_b - 1) \quad (B.7)$$

$$\hat{\epsilon}_b \beta_a h = \beta_b h \tan \beta_b h \quad (B.8)$$

where $\hat{\epsilon}_b = \epsilon_b / \epsilon_a$ and $\hat{\mu}_b = \mu_b / \mu_a$.

Surface waves are only the real roots of (B.7) and (B.8). A set of complex roots also exists, but these roots are located on an improper sheet of the Riemann surface in the k_x plane. However, after a transformation for the purpose of applying the steepest descents method it is found that the complex roots become a necessary and important part of the analytical solution for the far fields. The complex roots give rise to what is most commonly referred to in the literature as leaky waves.

Although it is a relatively simple matter to calculate the complex roots by use of graphical techniques when ϵ_a and ϵ_b are real quantities [32], this calculation for both TE and TM cases is more readily handled

by use of numerical methods. A computer program was written to determine the complex roots (and more accurately determine the real roots) by use of the Muller method [35].

B.3 A Physical Interpretation

From the information we now have, a physical interpretation of the various regions of the spectral distribution can be given [6]. The integrals (B.5) and (B.6) indicate that waves have been excited in the region $h \geq z \geq 0$ with a transverse wave number k_x ranging from $-\infty$ to ∞ . Waves are transmitted to the far field only when they have a wave number in the range $|k_x| \leq k_a$. The region $k_a < |k_x| < k_b$ is the allowable range for surface waves to occur. The remaining section $|k_x| \geq k_b$ gives rise to evanescent waves which are attenuated away from the plane of excitation.

Having now gathered all the necessary information about the integral of Eqs. (B.5) and (B.6) we proceed with a brief explanation as to how this integral may be solved analytically.

B.4 Evaluation of the Magnetic Field Integral

B.4a Determination of the Proper Branch

Appendix A outlines a technique for determination of the proper branch for the general case of a lossy region having a dielectric constant k_a . For application to the problems of proceeding sections k_a is replaced by the free space propagation constant k_0 which contains no complex part. Also β_a is replaced by β_0 in the following sections. The branch cuts

now collapses onto the axes as shown in Fig. B1. This figure also illustrates how the path of integration, which extends from $-\infty$ to $+\infty$ along $\text{Re}k_x$, must be deformed to account for the branch cut, the existence of typical surface wave poles at $\pm k_s$ and the branch points at $\pm k_o$.

B.4b Transformation into α -plane ($z \geq h$)

In order to evaluate Eq. (B.5) asymptotically by the saddle point method, it is convenient to change from rectangular $\text{Re}(k_x)$, $\text{Im}(k_x)$ coordinates to cylindrical coordinates r, θ . In doing so, we will be mapping from the k_x -plane to the α -plane. Let

$$k_x = k_o \sin \alpha \quad (\text{B.9})$$

$$\beta_o^{\text{ex}} = k_o \cos \alpha \quad (\text{B.10})$$

also let

$$x - x_n = r_n \sin \theta_n \quad (\text{B.11})$$

$$z = r_n \cos \theta_n \quad (\text{B.12})$$

where r_n is the distance from the nth match point in the slot to the observation point and θ_n is the angle of observation measured from a normal constructed at the nth match point perpendicular to the plane of the slot. The angle θ_n is positive for $x - x_n$ positive and negative for $x - x_n$ negative.

The exterior magnetic field can be rewritten as

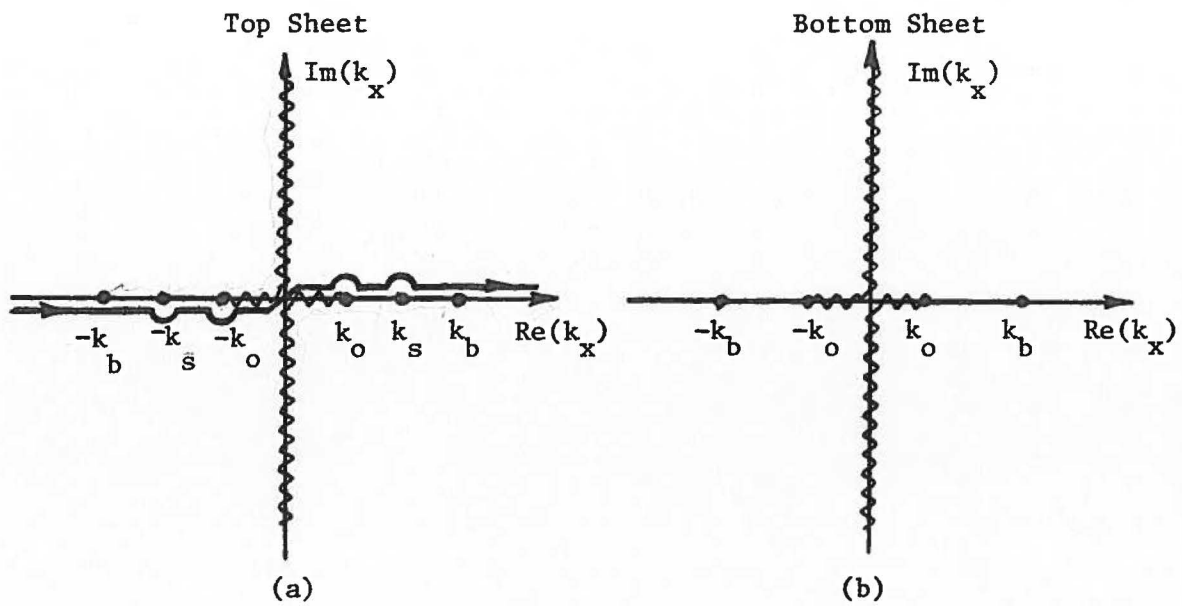


Fig. B.1 Top and bottom sheets of the complex k_x -plane for the case of a dielectric slab with no loss.

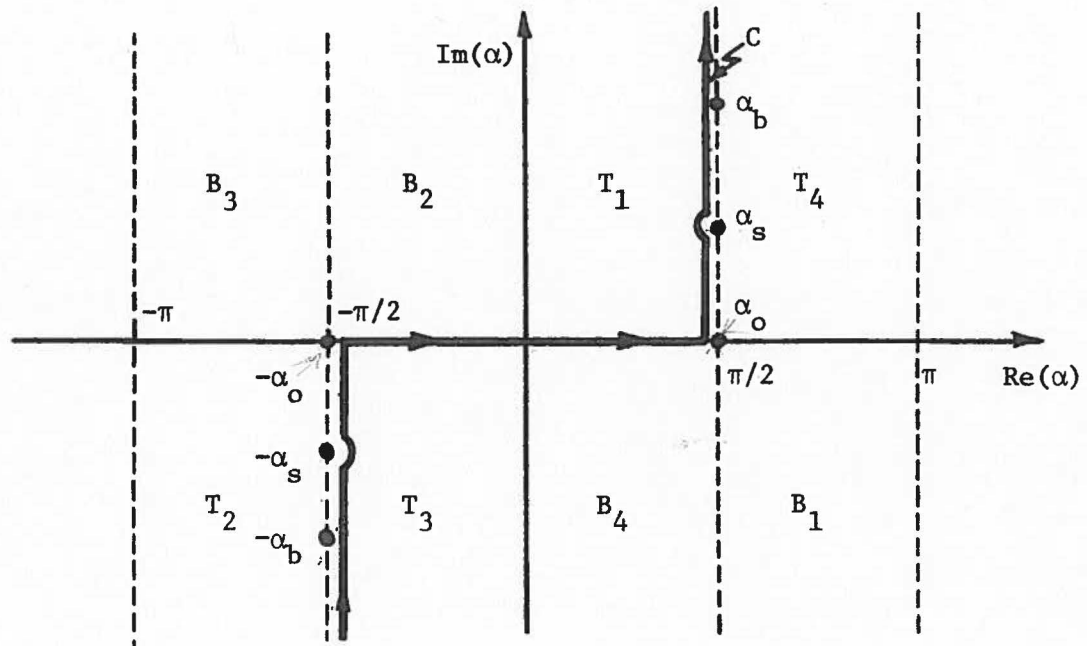


Fig. B.2 Complex α -plane segmented to indicate quadrants mapped from the top (T) and bottom (B) of the k_x -plane.

$$H_y^{ex} = \frac{-k_o \Delta}{2\pi\eta_o} \sum_{n=1}^N c_n \int_C \left(\frac{1 + r_k^{ex}}{1 + r_k^{ex} e^{-j2h\beta_b^{ex}}} \right) e^{jh(\beta_o^{ex} - \beta_b^{ex})} X e^{-jk_o r_n \cos(\alpha + \theta_n)} \left(\frac{\sin \frac{\Delta k_o \sin \alpha}{2}}{\frac{\Delta k_o \sin \alpha}{2}} \right) d\alpha , z \geq h \quad (B.13)$$

where

$$\beta_b^{ex} = \sqrt{k_b^2 - k_o^2 \sin^2 \alpha}$$

and

$$r_k^{ex} = \frac{\epsilon_b \beta_o^{ex} - \epsilon_a \beta_b^{ex}}{\epsilon_b \beta_o^{ex} + \epsilon_a \beta_b^{ex}}$$

Now that the proper form of the integral in the α -plane is available it is necessary to determine the exact path followed by the contour C . To do this let α be represented by a complex number, $\alpha = u + jv$. From (B.9) we then get

$$\operatorname{Re}(k_x) = k_o \sin u \cosh v \quad (B.14)$$

$$\operatorname{Im}(k_x) = k_o \cos u \sinh v \quad (B.15)$$

It is assumed that $\operatorname{Im}(\beta_o^{ex}) < 0$ on the top sheet of the Riemann surface.

Since $\beta_o^{ex} = k_o \cos u \cosh v - j k_o \sin u \sinh v$, then using the fact that

$\operatorname{Im}\beta_o^{ex} < 0$ which implies that $k_o \sin u \sinh v > 0$ it can be determined

whether various sections of the α -plane surface were transformed from the top (T) or bottom (B) k_x -plane. The subscripts shown in Fig. B.2 which designate the quadrants of the k_x -plane, are found by substituting various

values of u and v into (B.14) and (B.15) (e.g., if at some point in the α -plane $u = a$, $v = b$ where $k_o \sin a \sinh b > 0$ and $\operatorname{Re}(k_x) = k_o \sin a \cosh b > 0$, $\operatorname{Im}(k_x) = k_o \cos a \sinh b > 0$ then this point in the α -plane corresponds to a point on the top sheet in the first quadrant of the k_x -plane and so on). The path of integration is shown by the arrows in Fig. B2. The part of the integration path from $-\pi/2$ to $\pi/2$ along the real axis represents the homogeneous waves while the part of the path off the real axis represents the inhomogeneous waves propagating in the positive and negative z directions.

B.4c Transformation into the γ -plane ($0 \leq z \leq h$)

In order to evaluate Eq. (B.6) asymptotically it is necessary to once again transform into the cylindrical coordinate system, but a set of transformation equations different from those used for Eq. (B.5) prove to be more convenient. Let

$$k_x = k_b \sin \gamma \quad (\text{B.16})$$

$$\beta_b^{\text{in}} = k_b \cos \gamma$$

and once again let

$$x - x_n = r_n \sin \theta_n \quad (\text{B.17})$$

$$z = r_n \cos \theta_n$$

where r_n and θ_n are defined as in Section B.4b. The interior magnetic field can be rewritten as

$$\begin{aligned}
 H_y^{in} = & -\frac{k_b \Delta}{2\pi n_b} \sum_{n=1}^N c_n \int_C \left(\frac{1 - \Gamma_k^{in} e^{-j2\beta_b^{in}(h - r_n \cos \theta_n)}}{1 + \Gamma_k^{in} e^{-j2h\beta_b^{in}}} \right) \\
 & \times e^{-jk_b r_n \cos(\gamma + \theta_n)} \left(\frac{\sin \frac{\Delta k_b \sin \gamma}{2}}{\frac{\Delta k_b \sin \gamma}{2}} \right) d\gamma , \quad 0 \leq z \leq h \quad (B.18)
 \end{aligned}$$

where

$$\beta_o^{in} = -j\sqrt{k_b^2 \sin^2 \gamma - k_o^2}$$

and

$$\Gamma_k^{in} = \frac{\epsilon_b \beta_o^{in} - \epsilon_a \beta_b^{in}}{\epsilon_b \beta_o^{in} + \epsilon_a \beta_b^{in}}$$

Fig. B.3 shows the contour of integration in the γ -plane with an indentation around γ_b accounting for a pole behavior of the Sommerfeld integrand.

A point should be made here concerning the options of γ and k_x integrals [33]. The γ integration has the advantage of easy interpretation in terms of the observation angle θ plus the consideration that $\pm k_o$, which are branch points in the k_x -plane, have corresponding values which are regular in the γ -plane. However evaluation of the Sommerfeld integral in the k_x -plane is essentially a Fourier transformation process over a rather complicated function which is also singular. For subsequent use in this paper we will therefore operate in the γ -plane due to the applicability of the saddle point method to our integral. A method for

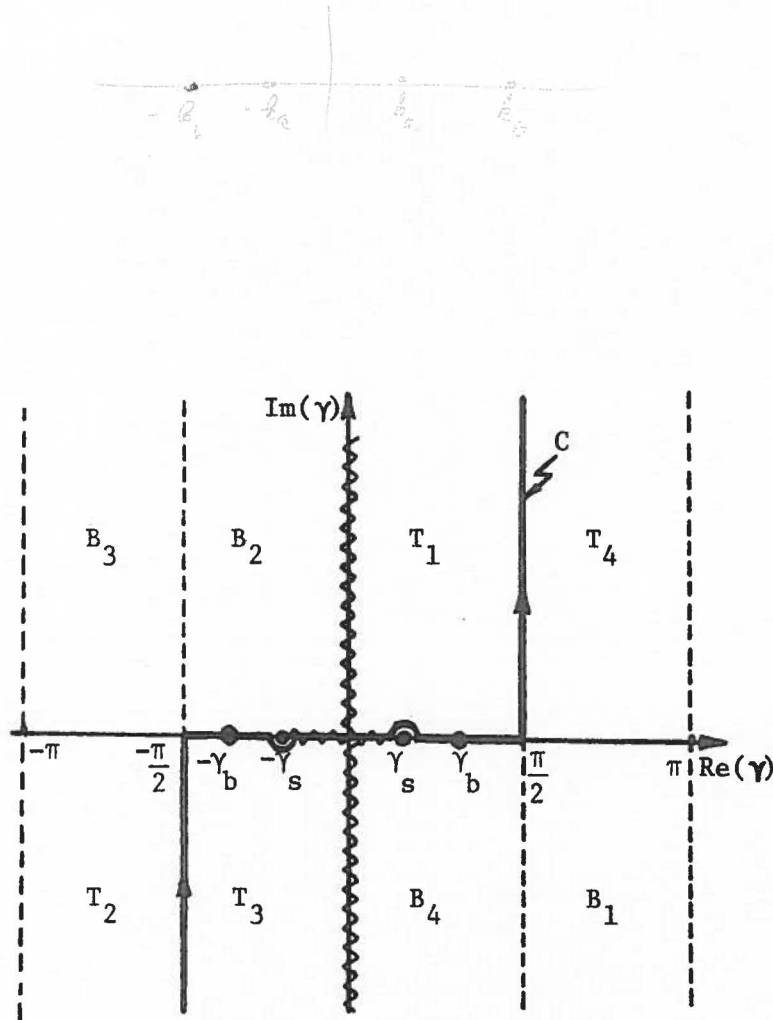


Fig. B.3 The complex γ -plane segmented into quadrants mapped from the top (T) and bottom (B) of the k_x -plane.

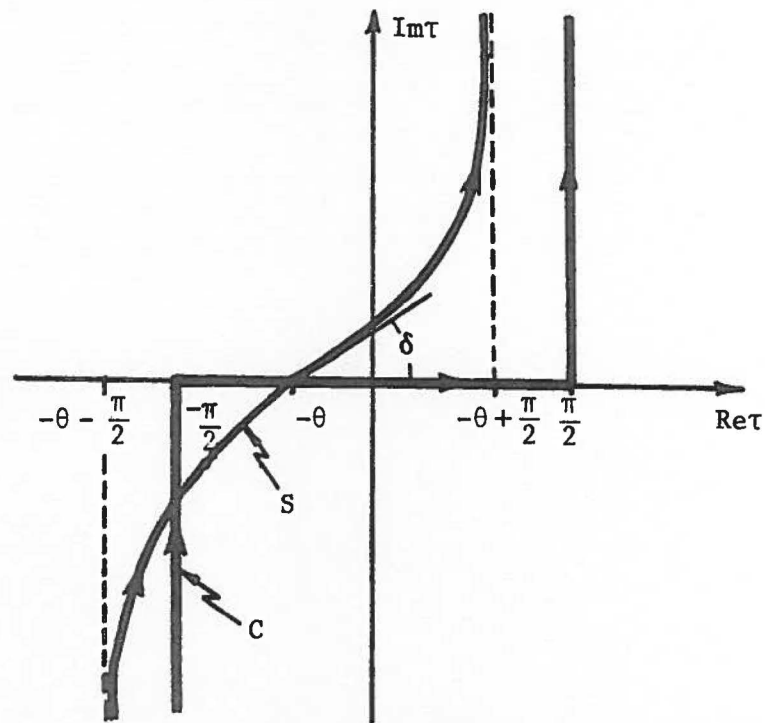


Fig. B.4 Contours in the complex τ -plane before (C) and after (S) deformation through the steepest descents path.

evaluation of a general integral of the form found in Eqs. (B.13) and (B.18) is presented in the following section.

B.4d Saddle Point Method

In this section we apply the saddle point method to the integral

$$I = \int_c U(\tau) e^{-jk_o r \cos(\tau + \theta)} d\tau \quad (B.19)$$

Here θ is some positive angle of observation and we assume initially that no poles occur in $U(\tau)$ at points near $\tau = -\theta$. Let

$$\tau = \tau_r + j\tau_i$$

then if

$$f(\tau) = -j\cos(\tau + \theta)$$

one can write

$$f(\tau) = -j\cos(\tau_r + \theta)\cosh\tau_i - \sin(\tau_r + \theta)\sinh\tau_i \quad (B.20)$$

For satisfaction of the saddle point requirement that $f'(\tau) = 0$ we have

$$f'(\tau) = j\sin(\tau + \theta) = 0$$

or

$$\sin(\tau_r + \theta)\cosh\tau_i = 0 \quad (B.21)$$

and

$$\cos(\tau_r + \theta)\sinh\tau_i = 0 \quad (B.22)$$

Since for any $x \cosh x > 0$, then in order to satisfy (B.21) we must have $\sin(\tau_r + \theta) = 0 \Rightarrow \tau_r = -\theta + n\pi$, $n = 0, \pm 1, \pm 2 \dots$. In (B.22) this means that

$\cos(\tau_r + \theta) = \pm 1$, therefore $\sinh\tau_i = 0 \Rightarrow \tau_i = 0$. Allowing only for $n = 0$ so $\tau_r = -\theta$ then the saddle point is found to be on the real axis in the complex τ -plane at the point $\tau_r = -\theta$.

The path of integration must pass through the saddle point at an angle δ so that $\text{Im } f(-\theta) = \text{constant}$. Evaluating the imaginary part of (B.20) at the saddle point where $\tau_r = -\theta$ and $\tau_i = 0$ one gets

$$\text{Im } f(-\theta, 0) = -\cos(-\theta + \theta)\cosh(0) = -1$$

therefore

$$\cos(\tau_r + \theta) \cosh\tau_i = 1 \quad (\text{B.23})$$

for all points on the significant portion of the path of integration. That is to say, Eq. (B.23) is an equation for the deformed path of integration along the contour S.

Concerning the behavior of the deformed path of integration, we see from (B.23) that since $\cos(\tau_r + \theta) = \frac{1}{\cosh\tau_i}$ then as $\tau_i \rightarrow \pm \infty$, $\cos(\tau_r + \theta) \rightarrow 0 \Rightarrow \tau_r = -\theta \pm \pi/2$. The path is now deformed in the τ -plane from the path C to the path S shown in Fig. B4 for $\theta > 0$.

In order to evaluate (B.19) analytically one must expand the exponent of the exponential in a Taylor-series about the saddle point:

$$-jk_o r \cos(\tau + \theta) \doteq -jk_o r \left(1 - \frac{(\tau + \theta)^2}{2!}\right),$$

(B.19) now becomes

$$I \doteq e^{-jk_o r} \int_C U(\tau) e^{jk_o r (\tau + \theta)^2 / 2} d\tau \quad (\text{B.24})$$

For the purpose of gaining an asymptotic solution to the above integral we would prefer to have an integral of the form

$$\int_{-\infty}^{\infty} U(\lambda) e^{-|z|\lambda^2} d\lambda , \quad \lambda \text{ real}$$

Therefore in Eq. (B.24) let

$$\lambda^2 = -j(\tau + \theta)^2$$

Now let $(\tau + \theta) = \rho e^{j\delta}$ where δ is the angle the path of integration makes with real axis in the upper half τ -plane (i.e., $\text{Im}\tau > 0$) and $\rho > 0$. Now

$$\lambda^2 = \rho^2 e^{-j\pi/2} e^{j2\delta}$$

and

$$\lambda = \rho e^{-j\pi/4} e^{j\delta}$$

In order for λ to be real δ must be defined as $\delta = \pi/4$ or $\delta = 5\pi/4$.

Along the steepest descent contour near the saddle point

$$\tau + \theta = \rho e^{j\pi/4} \quad \text{and} \quad d\tau = e^{j\pi/4} d\rho , \quad \tau_i > 0$$

$$\tau + \theta = \rho e^{j5\pi/4} = -\rho e^{j\pi/4} \quad \text{and} \quad d\tau = -e^{j\pi/4} d\rho , \quad \tau_i < 0.$$

Assuming $U(\tau)$ does not have a pole in the vicinity of the saddle point, then one may expand in a power series about the saddle point.

$$U(\tau) = \sum_{n=0}^{\infty} U^{(n)}(-\theta) \frac{(\tau + \theta)^n}{n!} \quad \text{where} \quad U^{(n)}(-\theta) = \left. \frac{d^n U(\tau)}{d\tau^n} \right|_{\tau=-\theta}$$

(B.24) now becomes

$$\begin{aligned}
 I &\stackrel{\circ}{=} e^{-jk_o r} \sum_{n=0}^{\infty} \frac{U^{(n)}(-\theta)}{n!} \left[\int_{\rho_\epsilon}^0 (-\rho e^{j\pi/4})^n e^{jk_o r} \frac{(-\rho e^{j\pi/4})^2/2}{(-e^{j\pi/4})} d\rho \right. \\
 &\quad \left. + \int_0^{\rho_\epsilon} (\rho e^{j\pi/4})^n e^{jk_o r} \frac{(\rho e^{j\pi/4})^2/2}{(e^{j\pi/4})} d\rho \right] \\
 &= e^{-j(k_o r - \pi/4)} \sum_{n=0}^{\infty} \frac{U^{(n)}(-\theta)}{n!} e^{jn\pi/4} (1 + (-1)^n) \int_0^{\rho_\epsilon} \rho^n e^{-k_o r \rho^2/2} d\rho
 \end{aligned}$$

Although the limit of integration ρ_ϵ is determined by the radius of analyticity of the Taylor series expansion of $U(\theta)$, extending the value of ρ_ϵ to ∞ has little effect on the integrand since the exponential term is already negligible at ρ_ϵ , therefore

$$I \stackrel{\circ}{=} e^{-j(k_o r - \pi/4)} \sum_{n=0}^{\infty} \frac{2U^{(n)}(-\theta)}{n!} e^{jn\pi/4} \int_{\rho=0}^{\infty} \rho^n e^{-k_o r \rho^2/2} d\rho$$

n = 0, 2, 4, ... (B.25)

The value of the integral is found to be

$$\int_{\rho=0}^{\infty} \rho^n e^{-k_o r \rho^2/2} d\rho = \frac{\Gamma[(n+1)/2]}{2(k_o r/2)^{(n+1)/2}}, \quad n > -1$$

so

$$I \doteq e^{-j(k_o r - \pi/4)} \sum_{n=0}^{\infty} \frac{U^{(n)}(-\theta)}{n!} e^{jn\pi/4} \left(\frac{2}{k_o r}\right)^{(n+1)/2} \Gamma[(n+1)/2]$$

$$n = 0, 2, 4, \dots \quad (B.26)$$

If $n = 0$

$$I \doteq e^{-j(k_o r - \pi/4)} U(-\theta) \sqrt{\frac{2\pi}{k_o r}} \quad (B.27)$$

which is sufficient for most purposes where $r \rightarrow \infty$.

When the observation point is in the vicinity of a pole a Laurent-series expansion must be used in place of a Taylor-series expansion. Therefore, instead of expanding around the saddle point we expand around the pole τ_o

$$U(\tau) = \frac{F(\tau_o)}{\tau - \tau_o} + U_1(\tau)$$

where $F(\tau_o)$ is the residue of $U(\tau)$ at the saddle point and $U_1(\tau)$ is an analytic function around $-\theta$. $U_1(\tau)$ may be represented by a Taylor-series

$$U_1(\tau) = \sum_{n=0}^{\infty} A_n (\tau + \theta)^n$$

$$A_n = \frac{1}{n!} \frac{d^n}{d\tau^n} \left[U(\tau) - \frac{F(\tau_o)}{\tau - \tau_o} \right]$$

However, this situation may be avoided as long as the pole remains at a sufficient distance from the saddle point regardless of the angle of

observation.

B.4e Application of Saddle Point Method TE case ($z > h$)

The occurrence of poles in the integrand of Eq. (B.5) is, as has been mentioned before, a consequence of surface waves which are produced in a dielectric slab lying over a perfectly conducting ground. These poles occur on the real axis in the k_x -plane. It has been shown in the previous section that a deformation of the path of integration allows an analytic approach to the solution of the integral in Eq. (B.13). Careful attention however, must be paid to how the path of integration is deformed around the poles in the k_x -plane, in order to determine how these poles are captured by the path of integration in the α -plane. From Fig. B5 one can see that the surface wave pole is not captured until the angle of observation (saddle point) moves to some angle α_p away from the normal ($\theta = 0^\circ$).

The saddle point method assumes that most of the contribution to the integral occurs in the immediate vicinity of the saddle point. That is, the integrand rapidly becomes smaller as it is evaluated at successive points along on the path of integration in a direction away from the saddle point. When surface wave poles are encountered by the path of integration, a contribution to the integral due to these poles may be incorporated in the solution by adding the sum of their residues to the saddle point solution. When the dielectric slab medium is lossless the observation angle corresponding to the capture of a surface

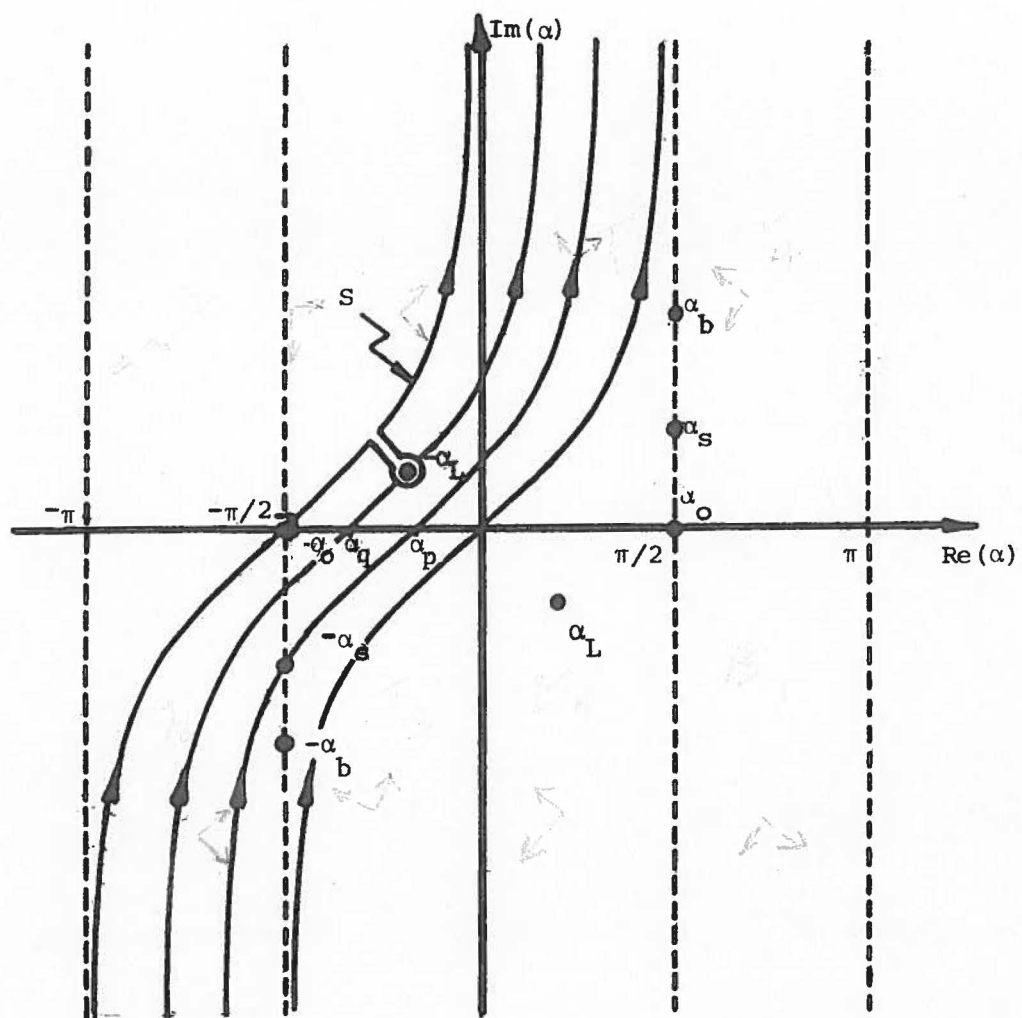


Fig. B.5 Successive steepest descent contours S demonstrating how surface and leaky wave poles are captured in the α -plane.

wave pole is given by $\alpha_p = \sin^{-1} k_o / k_s$.

As mentioned earlier, the surface wave pole is not the only pole which will be encountered by the path of integration. So called leaky-wave poles which come from the complex roots of the integrand of (B.13) must also be dealt with. If the integral in (B.13) is not solved by the saddle point method, then one normally would not be bothered by such poles since they occur on the bottom sheet of the Riemann surface in the k_x -plane. However, when the path is deformed in the α -plane, it will partially fall into regions which have been transformed from this bottom sheet. Therefore, it is seen in Fig. B5 that after the observation point has moved to an angle α_q from the normal, a leaky wave pole will now also be captured by the path of integration. The effect of these poles is accounted for by adding their residues to the saddle point method solution and the surface wave residues.

Referring to the previous section, the final form of the far magnetic field for the case of TE slot illumination can now be presented as

$$H_y^{\text{ex}} = \frac{-k_o \Delta}{2\pi\eta_o} \sum_{n=1}^N c_n \left[e^{-j(k_o r_n - \pi/4)} \right]$$

$$x \sum_{m=0}^{\infty} \frac{U^{(m)}(-\theta_n)}{m!} e^{-jm\pi/4} \left(\frac{2}{k_o r_n} \right)^{(m+1)/2} \Gamma[(m+1)/2]$$

$$+ 2\pi j \sum_S \text{Res}(\alpha_s) + 2\pi j \sum_L \text{Res}(\alpha_L) \Big] \\ m = 0, 2, 4, \dots \quad (B.28)$$

with

$$\text{Res}(\alpha_c) = \frac{j\beta_b^{\text{ex}} \sin(h\beta_b^{\text{ex}}) e^{jh\beta_o^{\text{ex}}} e^{-jk_o r_n \cos(\alpha_c + \theta_n)}}{\beta_o^{\text{ex}} (k_o \sin \alpha_c) \left[jh + \frac{\epsilon_a \epsilon_b (k_o^2 - k_b^2)}{\beta_o^{\text{ex}} \Gamma_{kn}^{\text{ex}} \Gamma_{kn}^{\text{ex}}} \right]} \frac{\sin\left(\frac{\Delta k_o \sin \alpha_c}{2}\right)}{\left(\frac{\Delta k_o \sin \alpha_c}{2}\right)}$$

$$c = s \text{ or } L$$

and

$$U(\alpha) = \left(\frac{1 + \Gamma_k^{\text{ex}}}{1 + \Gamma_k^{\text{ex}} e^{-j2h\beta_b^{\text{ex}}}} \right) e^{jh(\beta_o^{\text{ex}} - \beta_b^{\text{ex}})} \frac{\sin\left(\frac{k_o \Delta s \sin \alpha}{2}\right)}{\left(\frac{k_o \Delta s \sin \alpha}{2}\right)}$$

where $\text{Res}(\alpha_s)$ and $\text{Res}(\alpha_L)$ represent respectively the surface wave and leaky wave residues and (α_s, α_L) represent surface and leaky wave poles. $\Gamma_k^{\text{ex}} = \Gamma_{kn}^{\text{ex}} / \Gamma_{kd}^{\text{ex}}$ is as defined in Eq. (B.13) and Γ is the mathematical gamma function.

B.4f Application of the Saddle Point Method TE case ($0 \leq z \leq h$)

The analysis of the previous section is applicable to the magnetic field expression in the region $0 \leq z \leq h$. The deformed path of integration S in the γ -plane is shown for several angles of observation in Fig. B6. It should be noted however that only those contours which correspond to angles of observation interior to the slab (i.e. $\theta < \cos^{-1}(h/r)$) are

used for the interior problem.

The saddle point integration path of the Sommerfeld correction term will, in the γ -plane, intersect a branch cut for certain angles of observation of (Fig. B6). When the path of integration intersects a branch cut the path will then pass over onto the lower sheet of the Riemann surface. The portion of the path of integration on the lower sheet is indicated by the dashed line in Fig. B6. For such angles of observation a contribution due to the branch cut must be included in the field solution. The branch cut integration path is indicated by B in Fig. B6 and the contribution due to this branch cut integral is indicated by the term B.C. in the preceding equations. The steepest descents integration path S can be shown to intersect the branch cut integration path B at infinity. When the dielectric slab medium is lossless, the observation angle corresponding to the intersection of the branch cut and the path of integration is given by $\gamma_q = \sin^{-1}(k_o/k_b)$.

The far magnetic field inside the slab for the case of TE slot illumination can now be presented as

$$H_y^{in} = \frac{-k_b^\Delta}{2\pi n_b} \sum_{n=1}^N c_n \left[e^{-j(k_b r_n - \pi/4)} \right. \\ \left. \times \sum_{m=0}^N \frac{U^m (-\theta_n^m)^{jm\pi/4}}{m!} \left(\frac{2}{k_b r_n} \right)^{(m+1)/2} \Gamma[(m+1)/2] \right]$$

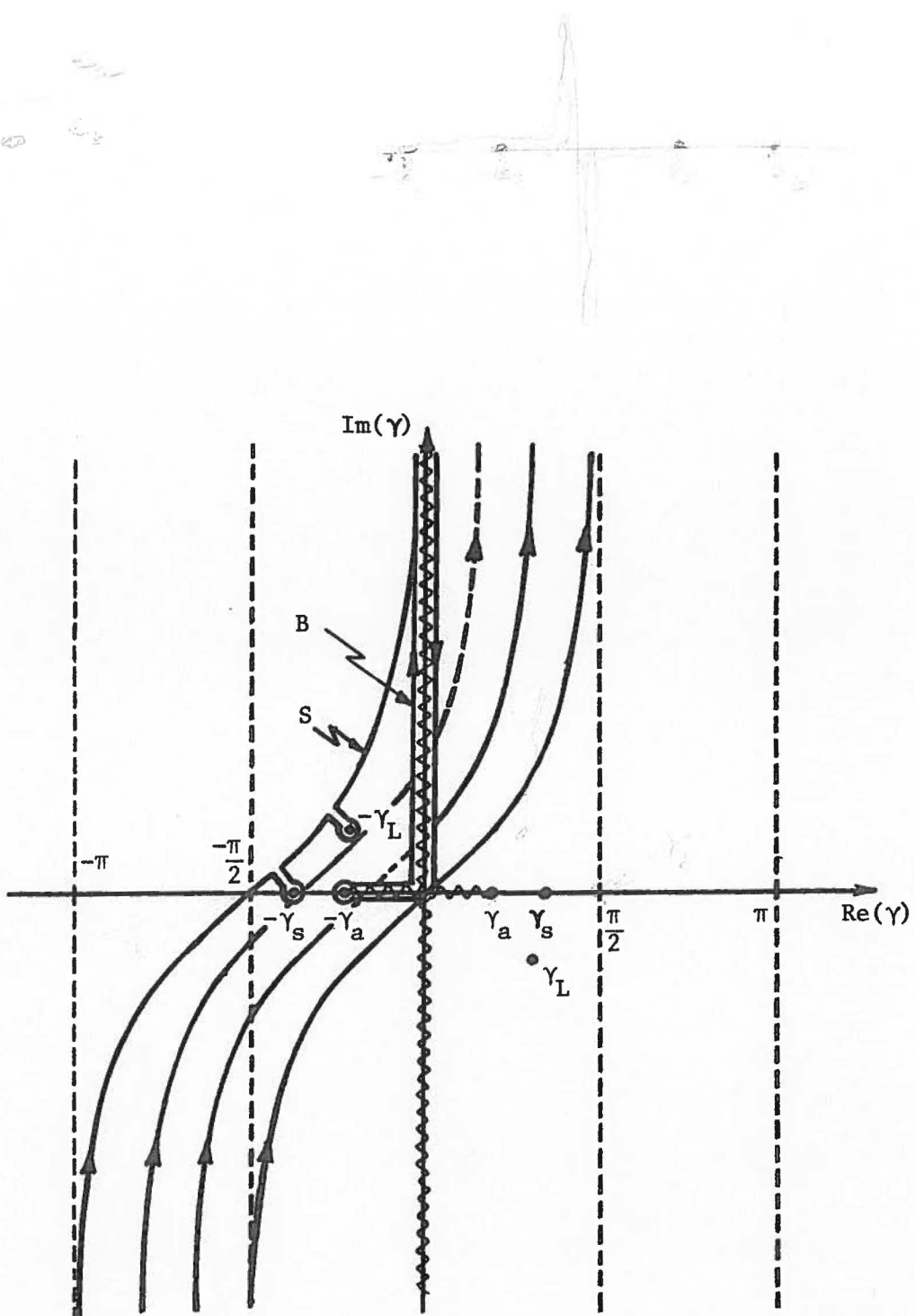


Fig. B.6 Successive steepest descent contours S demonstrating how surface and leaky wave poles are captured in the γ -plane.

$$+ 2\pi j \sum_S \text{Res}(\gamma_s) + 2\pi j \sum_L \text{Res}(\gamma_L) + \text{B.C.} \Bigg] \\ m = 0, 2, 4, \dots; 0 \leq z \leq h \quad (\text{B.29})$$

with

$$\text{Res}(\gamma_c) = \frac{-\cos(\beta_b^{\text{in}} r_n \cos \theta_n)}{\left(jh + \frac{\epsilon_a \epsilon_b (k_o^2 - k_b^2)}{\beta_o^{\text{in}} \Gamma_{kn}^{\text{in}} \Gamma_{kd}^{\text{in}}} \right)} e^{j k_b r_n \sin \gamma_c \sin \theta_n} \frac{\Delta k_b \sin \gamma_c}{\sin(\frac{\Delta k_b \sin \gamma_c}{2})}$$

C=S or L

and

$$U(\gamma) = \left(\frac{1 - \Gamma_k^{\text{in}} e^{-j2\beta_b^{\text{in}}(h-r_n \cos \theta_n)}}{1 + \Gamma_k^{\text{in}} e^{-j2h\beta_b^{\text{in}}}} \right) \frac{\Delta k_b \sin \gamma}{\sin(\frac{\Delta k_b \sin \gamma}{2})}$$

where $\text{Res}(\gamma_s)$ and $\text{Res}(\gamma_L)$ represent respectively the surface and leaky wave residues and B.C. is the contribution due to the branch cut.

$\Gamma_k^{\text{in}} = \Gamma_{kn}^{\text{in}} / \Gamma_{kd}^{\text{in}}$ is as defined in Eq. (B.18) and Γ is the mathematical gamma function. For this case the surface wave occurs for the angle of observation $\gamma = \gamma_s = -\theta_n = \sin^{-1} k_s / k_b$.

B.5(a) Application of the Saddle Point Method TM case ($z \geq h$)

For the case of TM illumination of the slot it is advantageous to formulate an expression for the far electric field. The TM case far electric field is found to be

$$E_y^{ex} = \frac{\Delta}{2\pi} \sum_{n=1}^N c_n \int_C \left(\frac{1 + \frac{\Gamma_g^{ex}}{g}}{1 + \frac{\Gamma_g^{ex}}{g} e^{-j2h\beta_b^{ex}}} \right) e^{jh(\beta_o^{ex} - \beta_b^{ex})} x e^{-jk_o r_n \cos(\alpha + \theta_n)} \begin{pmatrix} \sin \frac{k_o \Delta \sin \alpha}{2} \\ \frac{\sin \frac{k_o \Delta \sin \alpha}{2}}{k_o \Delta \sin \alpha} \end{pmatrix} \beta_o^{ex} d\alpha$$

which, after application of the saddle point method, becomes

$$E_y^{ex} = \frac{\Delta}{2\pi} \sum_{n=1}^N c_n \left[e^{-j(k_o r_n - \pi/4)} x \sum_{m=0}^{\infty} \frac{v^{(m)}(-\theta_n)}{m!} e^{jm\pi/4} \left(\frac{2}{k_o r_n} \right)^{(m+1)/2} \Gamma[(m+1)/2] + 2\pi j \sum_S \text{Res}(\alpha_S) + 2\pi j \sum_L \text{Res}(\alpha_L) \right]$$

$$m = 0, 2, 4, \dots ; z \geq h \quad (B.30)$$

with

$$\text{Res}(\alpha_S) = \frac{j\beta_b^{ex} \sin(h\beta_b^{ex}) e^{jh\beta_o^{ex}}}{(k_o \sin \alpha_c) \left[jh + \frac{\mu_a \mu_b (k_b^2 - k_o^2)}{\beta_o^{ex} \Gamma_g^{ex} \Gamma_{gd}^{ex}} \right]} \frac{e^{-jk_o r_n \cos(\alpha_c + \theta_n)}}{\frac{\sin \left(\frac{k_o \Delta \sin \alpha_c}{2} \right)}{\left(\frac{k_o \Delta \sin \alpha_c}{2} \right)}}$$

, C = s or l.

and

$$V(\alpha) = \left(\frac{1 + \frac{\Gamma^{ex}}{g}}{1 + \frac{\Gamma^{ex}}{g} e^{-j2h\beta_b^{ex}}} \right) e^{jh(\beta_o^{ex} - \beta_b^{ex})} \beta_o^{ex} \frac{\sin\left(\frac{k_o \Delta \sin \alpha}{2}\right)}{\left(\frac{k_o \Delta \sin \alpha}{2}\right)}$$

where

$$\frac{\Gamma^{ex}}{g} = \frac{\mu_a \beta_b^{ex} - \mu_b \beta_a^{ex}}{\mu_a \beta_b^{ex} + \mu_b \beta_a^{ex}} = \frac{\Gamma^{ex}}{\Gamma^{ex} gd}$$

B.5(b) Application of the Steepest Descents Method, TM Case ($0 \leq z \leq h$)

The electric field interior to the dielectric slab has been determined to be

$$E_y^{in} = -\frac{\Delta}{2\pi} \sum_{n=1}^N C_n \int_C \left(\frac{1 + \frac{\Gamma^{in}}{g} e^{-j2\beta_b^{in}(h-r_n \cos \theta_n)}}{1 + \frac{\Gamma^{in}}{g} e^{-j2h\beta_b^{in}}} \right) X \beta_b^{in} e^{-jk_b r_n \cos(\gamma + \theta_n)} \frac{\sin\left(\frac{k_b \Delta \sin \gamma}{2}\right)}{\left(\frac{k_b \Delta \sin \gamma}{2}\right)} d\gamma$$

which, with application of the steepest descents method, yields

$$E_y^{in} = -\frac{\Delta}{2\pi} \sum_{n=1}^N C_n \left[e^{-j(k_b r_n - \pi/4)} \right]$$

$$x \sum_{m=0}^{\infty} \frac{v^{(m)} (-\theta_n)^m e^{jm\pi/4}}{m!} \left(\frac{2}{k_b r_n}\right)^{(m+1)/2} \Gamma[(m+1)/2]$$

$$+ 2\pi j \sum_S \text{Res}(\gamma_s) + 2\pi j \sum_L \text{Res}(\gamma_L) + \text{B.C.} \quad]$$

$$m = 0, 2, 4, \dots; \quad 0 \leq z \leq h \quad (\text{B.31})$$

with

$$\text{Res}(\gamma_c) = \frac{j \beta_b^{in} \sin(\beta_b^{in} r_n \cos \theta_n)}{(k_b \sin \gamma_c) \left[jh + \frac{\mu_a \mu_b (k_b^2 - k_o^2)}{\beta_o^{in} \Gamma^{in} \Gamma^{in} g n g d} \right]} \frac{e^{j k_b r_n \sin \gamma_c \sin \theta_n}}{\sin\left(\frac{k_b \Delta \sin \gamma_c}{2}\right)} \frac{\sin\left(\frac{k_b \Delta \sin \gamma_c}{2}\right)}{\left(\frac{k_b \Delta \sin \gamma_c}{2}\right)}$$

where C = S or L

and

$$v(\gamma) = \left(\frac{1 + \frac{\Gamma_g^{in} e^{-j2\beta_b^{in}(h-r_n \cos \theta_n)}}{1 + \frac{\Gamma_g^{in} e^{-j2h\beta_b^{in}}}{\mu_a \beta_b^{in} + \mu_b \beta_o^{in}}}}{\beta_b^{in}} \right) \frac{\sin\left(\frac{k_b \Delta \sin \gamma}{2}\right)}{\left(\frac{k_b \Delta \sin \gamma}{2}\right)}$$

where

$$\Gamma_g^{in} = \frac{\mu_a \beta_b^{in} - \mu_b \beta_o^{in}}{\mu_a \beta_b^{in} + \mu_b \beta_o^{in}} = \frac{\Gamma_g^{in}}{\Gamma_g^{in} g d}$$

APPENDIX C

SURFACE WAVE MODES

The following is an outline of the vector potential solution method for finding the surface wave modes for the structure shown in Fig. C1 and for establishing the allowable surface wave region in the complex k_x -plane. The TM modes are found, so that $H_x = 0$ and no variation occurs with respect to y . In the dielectric region the propagation constant is denoted by k_b and in the region $z > h$ by k_a , where in each case the dielectric constant ϵ is assumed to be real.

The wave equations for the two homogeneous regions of interest are

$$(\nabla_{xz}^2 + k_a^2) A_x^a = 0 , \quad z \leq h \quad (C.1)$$

$$(\nabla_{xz}^2 + k_b^2) A_x^b = 0 , \quad 0 \leq z \leq h \quad (C.2)$$

The electric and magnetic fields may be found in terms of the magnetic vector potentials where

$$E_x^b = - \frac{j\omega}{k_a^2} \left(k_b^2 + \frac{\partial^2}{\partial x^2} \right) A_x^b(x, z) \quad (C.3a)$$

$$E_z^a = - \frac{j\omega}{k_b^2} \frac{\partial^2}{\partial x \partial z} A_x^a(x, z) \quad (C.3b)$$

$$H_y^b = \frac{1}{\mu_a} \frac{\partial}{\partial z} A_x^b(x, z) \quad (C.3c)$$

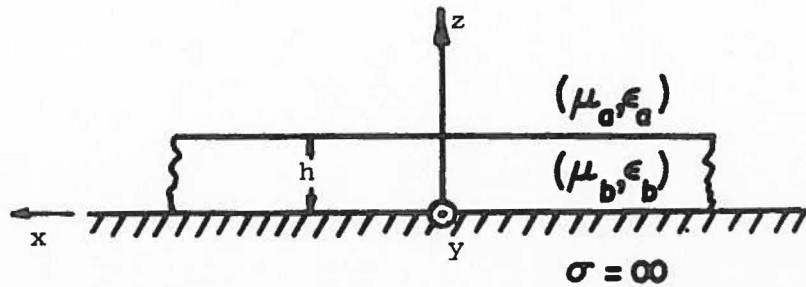


Fig. C.1 A dielectric slab of thickness h located above a perfectly conducting ground plane.

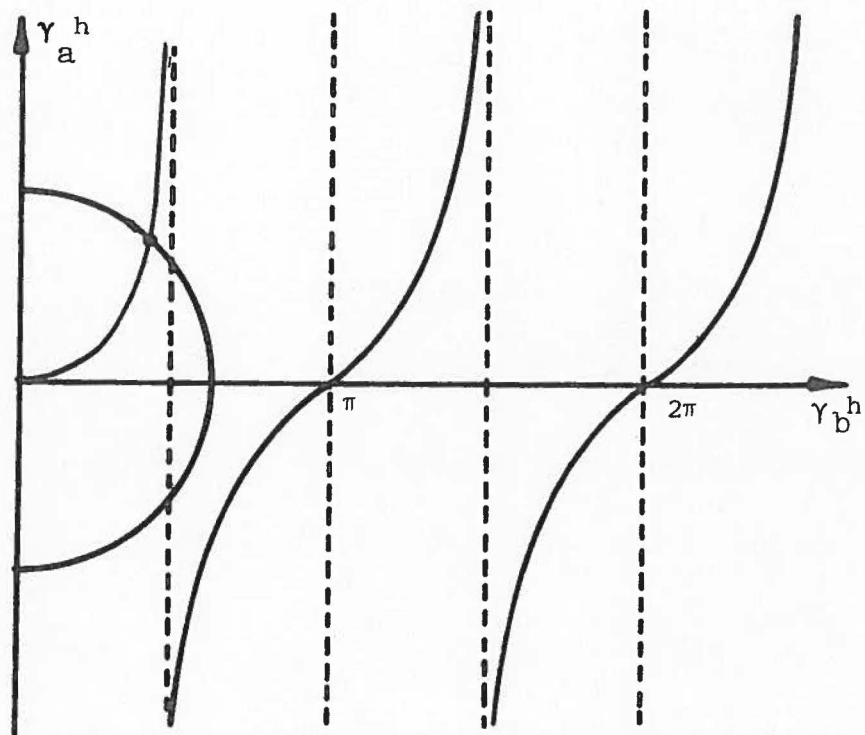


Fig. C.2 Graphical solution for surface wave modes.

A solution of Equations (C.1) and (C.2) requires satisfaction of the following boundary conditions

$$\frac{E_x^b}{x} = 0 \quad \text{at} \quad z = 0 \quad (\text{C.4a})$$

$$\frac{E_x^b}{x} = \frac{E_x^a}{x} \quad \text{at} \quad z = h \quad (\text{C.4b})$$

$$\frac{H_y^b}{y} = \frac{H_y^a}{y} \quad \text{at} \quad z = h \quad (\text{C.4c})$$

Since one would expect a standing wave in the z direction inside the slab and a rapidly decaying field in the z direction outside the slab, appropriate solutions for the two regions may be written by inspection,

$$\frac{A_x^a}{x} = C e^{-\gamma_a^a z} e^{-jk_x^a x}, \quad z \geq h \quad (\text{C.5a})$$

$$\frac{A_x^b}{x} = D \sin \gamma_b^b z e^{-jk_x^b x}, \quad 0 \leq z \leq h \quad (\text{C.5b})$$

The supposition that the propagation constant k_x be the same in both regions is provided for by the boundary conditions (C.4b and C.4c) which require that the electric and magnetic fields be continuous at $z = h$. From (C.5a) and (C.1) and from (C.5b) and (C.2) we determine the characteristic equations of the two regions:

$$-k_x^2 + \gamma_a^2 + k_a^2 = 0 \quad (\text{C.6})$$

and

$$-k_x^2 - \gamma_b^2 + k_b^2 = 0 \quad (\text{C.7})$$

Subtracting (C.7) from (C.6) and multiplying through by h^2 one gets

$$(\gamma_a h)^2 + (\gamma_b h)^2 = (k_a h)^2 (\mu_b \epsilon_b - 1) \quad (\text{C.8})$$

where $\tilde{\epsilon}_b = \epsilon_b / \epsilon_a$ and $\tilde{\mu}_b = \mu_b / \mu_a$ are the relative dielectric constant and in the dielectric region $0 \leq z \leq h$.

From (C.4b) and (C.5) one obtains

$$-\frac{C\gamma_a^2 e^{-\gamma_a h}}{k_a^2} = \frac{D\gamma_b^2 \sin \gamma_b h}{k_b^2} \quad (C.9)$$

and from (C.4c) and (C.5)

$$-\frac{C\gamma_a e^{-\gamma_a h}}{k_a} = \frac{D\gamma_b \cos \gamma_b h}{\tilde{\mu}_b} \quad (C.10)$$

Dividing (C.9) by (C.10) and multiplying through by h yield

$$\tilde{\epsilon}_b \gamma_a h = \gamma_b h \tan \gamma_b h \quad (C.11)$$

The eigenvalue solutions for γ_a and γ_b may be obtained graphically by superimposing the circles of (C.8) over the tangent curves of (C.11). The values of k_x determined by these solutions are the propagation constants for the surface waves.

Fig. C2 shows the graphical solution technique when $h = 0.25\lambda_b$, $\tilde{\mu}_b = 1$ and $\tilde{\epsilon}_b = 2.7$. Points of intersection in the region $\gamma_a h < 0$, are not physically valid solutions since the corresponding field would be exponentially increasing for positive z . Once the allowed values of γ_a and γ_b are determined, the allowed values of k_x for the surface waves may be found from either of the following two equations:

$$k_x = \pm \sqrt{\gamma_a^2 + k_a^2} \quad (C.12a)$$

$$k_x = \pm \sqrt{k_b^2 - \gamma_b^2} \quad (C.12b)$$

The plus-minus sign accounts for the existance of poles on both positive and negative real axis. The minimum allowable value for which k_x is both positive and real can be determined from (C.12a) to be k_a while the maximum allowable value can be determined from (C.12b) to be k_b . A similar statement can be made for k_x negative and real. One can now establish the surface wave region to be

$$k_a < |k_x| < k_b .$$

BIBLIOGRAPHY

- [1] M.C. Bailey, "The impedance properties of dielectric-covered narrow radiating slots in the broad face of a rectangular waveguide", IEEE Trans. Antennas Propagat., vol. AP-18, pp. 596-603, Sept. 1970.
- [2] M.C. Bailey and C.T. Swift, "Input admittance of a circular waveguide aperture covered by a dielectric slab", IEEE Trans. Antennas Propagat., vol. AP-16, pp. 386-391, July 1968.
- [3] W.F. Croswell, W.C. Taylor, C.T. Swift, and C.R. Cockrell, "The input admittance of a rectangular waveguide-fed aperture under an inhomogeneous plasma: theory and experiment", IEEE Trans. Antennas Propagat., vol. AP-16, pp. 475-487, July 1968.
- [4] E.R. Nagelberg, "Radiating properties of dielectric covered apertures", Bell Sys. Tech. J., vol. 47, pp. 2169-2181, Dec. 1968.
- [5] C.P. Wu and V. Galindo, "Surface-wave effects on dielectric sheathed phased arrays of rectangular waveguides", Bell Sys. Tech. J., vol. 47, pp. 117-142, Jan. 1968.
- [6] C.P. Wu, "Integral equation solution for the radiation from a waveguide through a dielectric slab", IEEE Trans. Antennas Propagat., vol. AP-17, pp. 733-739, Nov. 1969.
- [7] V. Galindo and C.P. Wu, "Dielectric loaded and covered rectangular waveguide phased arrays", Bell Sys. Tech. J., vol. 47, pp. 93-116, Jan. 1968.
- [8] M.C. Bailey and W.F. Croswell, "Pattern measurements on slot radiators in dielectric-coated metal plates", IEEE Trans. Antennas Propagat., vol. AP-15, pp. 824-826, Nov. 1967.
- [9] D.E. Clark, R.C. Rudduck, and D.C.F. Wu, "Two-dimensional radome analysis by a surface integration technique", Report 2767-5, 26 February 1970, The Ohio State University Electro-Science Lab, Dept. of E.E.; prepared under Contract N00019-69-C-0325 for Naval Air Systems Command (AD 866 375).
- [10] W.F. Croswell and R.B. Higgins, "Effects of dielectric covers over shunt slots in a waveguide", Langley Research Center, Hampton, Va., NASA TND-2518, Dec. 1964.
- [11] R.E. Cristen, "Investigation of the interaction between a longitudinal slot and a plasma", Antenna Lab, Ohio State University, Research Foundation Report 2146-4, 15 June 1966.

- [12] J.R. Wait, "On the conductance of slots", IRE Trans. Antennas and Propagation, vol. AP-4, pp. 124-127, April 1956.
- [13] A.F. Stevenson, "Theory of slots in rectangular waveguides", J. Appl. Phys., vol. 19, pp. 24-38, Jan. 1948.
- [14] A. Hessel and J.C. Sureau, "Resonances in circular arrays with dielectric sheet covers", IEEE Trans. Antennas Propagat., vol. AP-21, pp. 159-164, Mar. 1973.
- [15] Q. Balzano, "Analysis of period arrays of waveguide apertures on conducting cylinders covered by a dielectric", IEEE Trans. Antennas Propagat., pp. 25-34, Jan. 1974.
- [16] Q. Balzano et al., "Analysis of dielectric slab covered waveguide arrays on large cylinders", Raytheon Co., Bedford, Mass., BR-7663, Aug. 1973.
- [17] K.E. Golden and G.E. Stewart, "Linear array and feed network performance in a reentry plasma environment", IEEE Trans. Antennas Propagat., vol. AP-22, pp. 340-346, May 1972.
- [18] A.A. Oliner, "The impedance properties of narrow radiating slots in the broad face of rectangular waveguide: I and II", IRE Trans. Antennas and Propagation, vol. AP-5, pp. 4-20, Jan. 1957.
- [19] C.M. Knop and G.I. Cohn, "Radiation from an aperture in a coated plane", J. Res. Nat. Bur. Stand., vol. 68D (4), pp. 363-78, 1964.
- [20] A.T. Villeneuve, "Admittance of waveguide radiating into plasma environment", IEEE Trans. Antennas Propagat., vol. AP-13, pp. 115-121, Jan. 1965.
- [21] C.P. Wu, "Determination of resonance conditions in dielectric-sheathed or plug-loaded phase arrays", IEEE Trans. Antennas Propagat. (Commun.), vol. AP-16, pp. 358-360, May 1968.
- [22] L.I. Parad, "The input admittance to a slotted array with or without a dielectric sheet", IEEE Trans. Antennas Propagat. (Commun.), vol. AP-15, pp. 302-304, Mar. 1967.
- [23] N. Amitay and V. Galindo, "Characteristics of dielectric loaded and covered circular waveguide phased arrays", IEEE Trans. Antennas Propagat., vol. AP-17, pp. 722-729, Nov. 1969.
- [24] H.M. Barlow and A.L. Cullen, "Surface Waves", Proc. IEEE (London), Vol. 100, part III, pp. 329-347, Nov. 1953.

- [25] N. Amitay, V. Galindo, and C.P. Wu, Theory and Analysis of Phased Array Antennas, New York: Wiley-Interscience, 1972.
- [26] C.T. Tai, "The effect of a grounded slab on the radiation from a line source", J. Appl. Phys., vol. 22, pp. 405-414, April 1951.
- [27] S. Barone, "Leaky wave contributions to the field of a line source above a dielectric slab", Microwave Research Inst., Polytechnic Institute of Brooklyn, Brooklyn, N.Y., R-532-56, PIB-462, Nov. 1956.
- [28] E.T. Copson, Asymptotic Expansions, London: Cambridge University Press, 1965.
- [29] A. Erdeli, Asymptotic Expansions, New York: Dover Publications, Inc. 1956.
- [30] R. Mittra and S.W. Lee, Analytical Techniques in the Theory of Guided Waves, New York: Macmillan, 1971.
- [31] R.E. Collin, F.J. Zucker, Antenna Theory Part II, New York: McGraw-Hill, 1969.
- [32] R.E. Collin, Field Theory of Guided Waves, New York: McGraw-Hill, 1960.
- [33] P.C. Clemmow, The Plane Wave Spectrum Representation of Electromagnetic Fields, London: Cambridge University Press, 1966.
- [34] R.E. Collin, Foundations of Microwave Engineering, New York: McGraw Hill, 1953.
- [35] S.D. Conte, Carl deBoor, Elementary Numerical Analysis, New York: McGraw Hill, 1965.
- [36] P.M. Morse, H. Feshbach, Methods of Theoretical Physics, New York: McGraw Hill, 1953.
- [37] C.M. Butler, class notes.
- [38] A. Sommerfeld, Partial Differential Equations, New York: Academic Press, 1949.
- [39] C.M. Butler and D.R. Wilton, "Plates Apertures and Bodies", in Method of Moments Short Course Notes, University of Mississippi, 1976.
- [40] R.F. Harrington, Field Computation by the Method of Moments, New York: Macmillan, 1968.

- [41] R. Mittra, Computer Techniques for Electromagnetics, New York: Pergamon Press, 1973.
- [42] M. Abramowitz, I. A. Stegun, Handbook of Mathematical Functions, National Bureau of Standards, U.S. Government Printing Office, Washington, D.C., 1964.
- [43] I. S. Gradshteyn, I.M. Ryzhik, Tables of Integrals Series and Products, New York: Academic Press.
- [44] C. M. Butler, K. R. Umashankar, Radio Sci. 11, 611 (1976).
- [45] J. Brown, "The Type of Wave Which May Exist Near a Guiding Surface", Proc. IEE (London), Vol. 100, Part III, pp. 363-364, November, 1953.
- [46] C. M. Butler, A. Q. Howard, R. D. Nevels, "Electromagnetic Diffraction of an Aperture in a Planar Conducting Screen Separating Partitioned Half-Spaces", J. Appl. Phys., Vol. 48, pp. 4886-4892, December, 1977.

BIOGRAPHICAL SKETCH OF THE AUTHOR

Robert Dudley Nevels, Jr., was born in Hopkinsville, Kentucky, on April 14, 1946. He is the son of Mrs. Germaine Morris of Hopkinsville, Kentucky. Mr. Nevels graduated from Hopkinsville High School in May, 1964. From September, 1964 until May, 1969 he attended the University of Kentucky where he obtained a B.S. degree in Electrical Engineering. Mr. Nevels served as a communication specialist in the U.S. Army from 1970 until 1972. He received an Army Accommodation Medal during duty as a member of the Presidential Honor Guard in 1971. Mr. Nevels received a M.S. degree in Electrical Engineering with a minor in math from Georgia Institute of Technology in 1973. While at Georgia Tech, he worked as a research assistant with the Georgia Tech Experiment Station. Since 1974, Mr. Nevels has worked as a research assistant, teaching assistant and acting assistant professor at the University of Mississippi. He is currently employed as an Assistant Professor at Texas A and M University.